EFFECTS OF THE REACTING FLOWFIELD ON COMBUSTION PROCESSES IN A STAGNATION POINT REVERSE FLOW COMBUSTOR

A Dissertation
Presented to
The Academic Faculty

by

Priya Gopalakrishnan

In Partial Fulfillment
of the Requirements for the Degree
Doctor of Philosophy in
Aerospace Engineering

Georgia Institute of Technology

May 2008

EFFECTS OF THE REACTING FLOWFIELD ON COMBUSTION PROCESSES IN A STAGNATION POINT REVERSE FLOW COMBUSTOR

Approved By:

Dr. Jerry M. Seitzman, Advisor
Associate Professor
School of Aerospace Engineering
Georgia Institute of Technology

Dr. Yedidia Neumeier
Principal Research Engineer
School of Aerospace Engineering
Georgia Institute of Technology

Dr. Jechiel J. Jagoda
Professor, Associate Chair for Graduate Studies and Research
School of Aerospace Engineering
Georgia Institute of Technology

Dr. Ben T. Zinn
Regents Professor and David S. Lewis Jr. Chair
School of Aerospace Engineering
Georgia Institute of Technology

Dr. Minami Yoda
Professor, Woodruff School Faculty Fellow
School of Mechanical Engineering
Georgia Institute of Technology

Dr. Richard Gaeta
Senior Research Engineer
GTRI-Aero Transport and Advanced Systems Lab (ATAS),
Georgia Institute of Technology

Date Approved: 11th January 2008

For Divi

ACKNOWLEDGEMENTS

First and foremost I would like to express my sincere gratitude to my advisor, Dr. Jerry Seitzman, for being a great mentor and guide throughout my graduate career at the Aerospace Combustion Lab. I greatly appreciate his infinite patience and cheerful attitude during our discussions. I would also like to thank him for giving me the freedom to work things out at my own pace and for providing a wonderful learning opportunity.

I would like to thank Dr. Ben Zinn, Dr. Yedidia Neumeier, Dr. Jeff Jagoda, Dr. Minami Yoda and Dr. Rick Gaeta for taking the time read this thesis document and for their comments and suggestions. I would especially like to thank Dr. Yedidia Neumeier for always being around to help out with the experiments and for his hands-on approach to problem solving. I would also like to express my heartfelt appreciation to Dr. Jagoda for being so approachable to students in academics matters and others alike. Special thanks to Dr. Narayanan Komerath for his support during my Masters studies and for providing the opportunity to work on a variety of problems at the John Harper Wind Tunnel.

I would like to thank Bobba, JP, Nori, Murgi, Santosh S., Nelson, Thao, Yash, Sai and Qingguo for their help and valuable discussions on various topics. I have learnt a lot from all of them and am especially grateful for their help with all the heavy lifting for the experimental set-ups. I wish to express my sincere thanks to Karthik for his assistance with the data taking and for making it such a fun and enjoyable process. I would also like to extend a special thanks to all my colleagues at the Combustion Lab for their friendship and for making the lab a great work environment. I'm also indebted to Dr. Vaidya

Sankaran for his help during my qualifiers preparation and for his insightful discussions and suggestions.

I would like to thank Kapil, Preetham, Santosh H. and Prerona for organizing so many fun get-togethers and for making my stay in Atlanta delightful. I would also like to thank my roommates Rupa, Sunitha, Sonali, Vindhya, Shalini and Divya for their friendship and for everything I have learnt from them.

Last but not least I would like to thank my husband, Vijay, for his constant support and love throughout my graduate career. Finally, I owe everything, that I have and am yet to receive, to my loving parents and family.

TABLE OF CONTENTS

LIST OF TABLES

LIST OF FIGURES

SUMMARY

The performance of dry, low NOx gas turbines, which employ lean premixed (or partially premixed) combustors, is often limited by static and dynamic combustor stability, and they require complicated mixing hardware. To overcome these issues, a novel design, referred to as a Stagnation Point Reverse Flow (SPRF) combustor, has been recently demonstrated. The SPRF combustor has been shown to operate with ultra low NOx emissions in premixed *and nonpremixed* modes with gaseous and liquid fuels. The objective of this thesis is to elucidate the interactions between the flowfield and combustion processes in this novel combustor for gas- and liquid-fueled operation. This is achieved with experimental measurements employing various optical diagnostic techniques, which include Particle Image Velocimetry (PIV), chemiluminescence imaging, Planar Laser-Induced Fluorescence (PLIF) of OH radicals and elastic laser scattering from liquid droplets.

The velocity measurements obtained during gas-fueled operation show that both nonreacting and reacting flows exhibit a "stagnation" region with low mean velocity and high RMS fluctuations. In nonreacting flow, it has been shown that the decay rate of the jet can be modeled as a combination of a free jet and a jet in a uniform opposed flow. The high shear between the forward and reverse flows causes significant recirculation, resulting in enhanced entrainment and mixing of the returning hot product gases into the incoming reactant jet for the reacting flow cases, which enables stable operation of the combustor at very lean equivalence ratios. Nonpremixed operation produces a flowfield similar to that of the premixed case except in the near-field region. The coaxial injector

design results in high turbulence intensities close to the injector exit leading to significant fuel-air premixing before combustion occurs.

The operation of the SPRF combustor fueled with liquid Jet-A is also experimentally investigated. The results indicate that while the overall flow features are similar to the gas-fueled SPRF combustor, the combustion characteristics and NOx performance in liquid operation are strongly controlled by fuel dispersion and evaporation. Injecting the liquid at the exit of the air annulus results in a highly lifted flame, similar to nonpremixed gaseous operation. This is attributed to the initial shielding of fuel from the high temperature return products for this injector placement. On the other hand, retracting the fuel injector well inside the air produces a more well-dispersed fuel pattern at the reactant inlet leading to a reduction of the equivalence ratio in the fuel consuming reaction zones. This results in a decrease in NOx emissions when the liquid injector is retracted. Since the effective Dahmkohler number ($Da=\tau_{mix}/\tau_{chem}$) increases with ϕ_{global}, this difference in NOx performance is more pronounced at higher fuel-air ratios as the retracted injector lowers the relative mixing time compared to the flush case.

CHAPTER 1

INTRODUCTION AND MOTIVATION

1.1 Introduction

Environmental concerns and legislative regulations are driving combustor manufacturers to meet increasingly more stringent emission standards while maintaining (or improving) efficiency and reliability. Not only do combustion systems have to meet the current stringent requirements for NOx, CO, and soot emissions, but future engine designs will also be required to emit even lower levels of pollutants to meet future guidelines. Recent legislative regulations imposed by government agencies like the EPA are promoting lower pollutant solutions. Thus the NASA goals for future emission reductions include: "…reduc(ing) NOx emissions of future aircraft by 70 percent within 10 years, and by 80 percent within 25 years [1]." Goals such as this one continue to spur research into optimizing combustor designs for reduced emissions.

While lowering combustor emissions is an important goal for combustor designers, other considerations such as high power density, combustor stability, and low radiated noise are continually being addressed as well. Power density (or intensity), defined as the ratio between the combustion power generated and the total combustor volume, is a quantity that should be high for aircraft engines so as to be able to produce high thrust for less added weight. Clearly, improved and even novel combustor designs are needed to allow gas turbines to meet environmental and performance standards.

Most reductions in NOx emissions from gas and liquid-fueled combustors have been achieved mainly through lean premixed/partially premixed combustion, dilution with exhaust gases, staged combustion or similar approaches that primarily lower peak flame temperatures and consequently NOx emissions. Lean premixed natural gas combustors have demonstrated the capability to greatly reduce NOx emissions in gas turbines for ground power generation [2-3]. A similar potential for improvement exists for liquid-fueled combustors, for example using lean premixed, prevaporized approaches or lean direct injection. For current aeroengine combustors, which operate in a partially premixed mode with somewhat rapid mixing after fuel injection, increased fuel-lean operation should also lead to lower NOx emissions. However, in these approaches, combustor static and dynamic stability is compromised as the mixture is made leaner. This results from the weaker combustion process, which is more vulnerable to small perturbations in combustor operating conditions [4-5].

An alternative approach to lowering NOx is flue gas recirculation (FGR). Dilution of the reactants with *cooled*, inert products lowers the oxygen concentration and temperature before combustion, which lengthens the ignition delay [6]. This causes the combustion zone to be spread out over the entire mixing region rather than in a thin front. The increased ignition delay also allows sufficient time for premixing of fuel and air before burning occurs. The result is a more uniform temperature distribution that helps to lower NOx levels. In contrast to FGR, many combustors also have some internal or external recirculation of hot products, denoted here as exhaust gas recirculation (EGR). NOx reductions similar to those obtained by FGR have been predicted for hot EGR [7]. However, the role of EGR in lowering NOx emissions is not completely understood, as

the enhanced reactivity due to addition of hot products and radicals offsets the increased ignition delay produced by lowering the oxygen concentration.

A new, compact combustor design that incorporates some aspects of these other approaches has recently been demonstrated [8]. This Stagnation Point Reverse Flow (SPRF) combustor's unique design enables it to burn gaseous or liquid fuels with low NOx and CO emissions. In its simplest configuration, a nearly adiabatic combustor consists of a tube with one end open and the other closed (Figure 1). Unlike most combustors, the reactants and products enter and leave this combustor at the same end. The reactants are injected (without swirl) along the combustor centerline, moving towards the closed end. The flow must eventually reverse to exit the combustor, so the products can also mix with the incoming reactants.

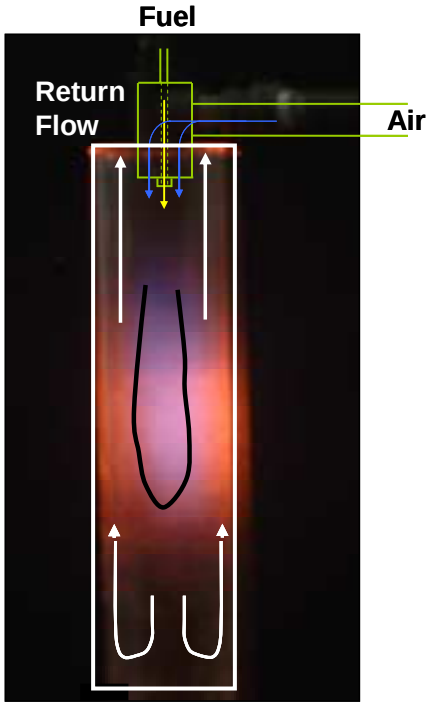

Figure 1. Schematic of stagnation point reverse flow (SPRF) combustor.

1.2 Motivation and Objectives

The SPRF combustor has been shown to operate stably over a wide range of equivalence ratios and loadings. While low NOx emissions from this combustor operating with lean premixed reactants might be expected, nonpremixed operation can also achieve very low NOx levels. For example, previous work [8] has demonstrated that the NOx emissions at a fixed lean overall equivalence ratio were roughly similar for both modes of operation when the combustor is fueled with natural gas (Figure 2). In addition to producing very low NOx emissions, the combustor operates stably without external preheating, even at very low fuel-air ratios and high loadings resulting in high power densities. The combustor has also been demonstrated to operate with low NOx emission in liquid-fueled mode without external prevaporization of the fuel [9].

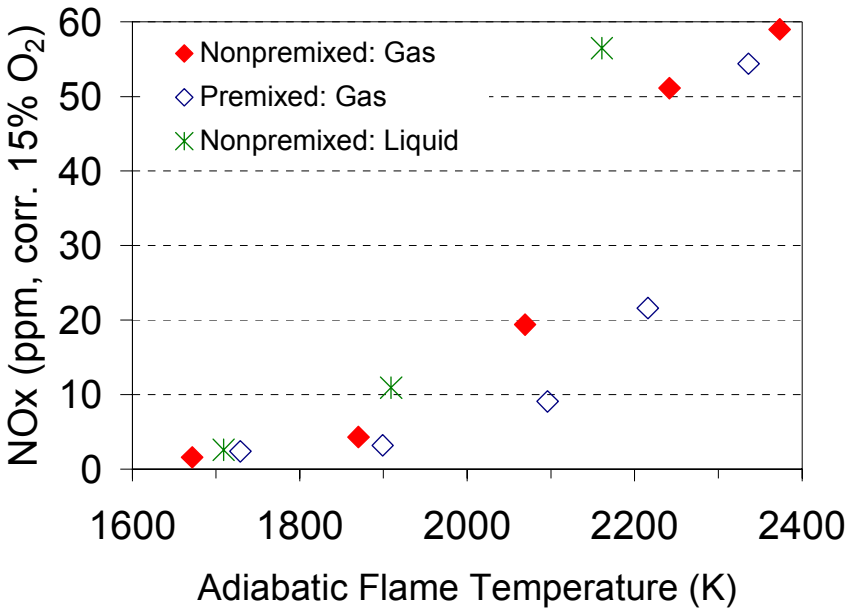

Figure 2. Variation of NOx emissions with adiabatic flame temperature based on overall equivalence ratio and measured inlet temperature.

The SPRF combustor's unique geometry allows for both the creation of a low velocity region and interactions between incoming reactants and exiting combustion

products as a means of stabilization of the combustion process and reduction of NOx emissions. Therefore, the flowfield created in the combustor is of great importance since it determines the residence times and mixing characteristics, that impact flame stabilization and emissions. Thus one of the main objectives of this thesis is to examine the flowfield of the Stagnation Point Reverse Flow combustor while operating with natural gas to resolve the average velocities and turbulence levels in different regions of the combustor and to determine the interplay between the flowfield and the heat release processes. In part, this will include examining the instantaneous velocities to provide a basis for understanding the sizes and locations of the large scale vortical structures and their influence on the product entrainment and mixing.

Although gaseous fuels are suitable in many instances, a number of applications require burning of liquid fuels, e.g., aircraft turbine engines. While lean premixed, prevaporized combustion is an option to achieve low NOx emissions in liquid fueled systems, external (ahead of the combustor) prevaporization of liquid fuel creates a serious safety hazard and adds extra complexity to the system. Thus, injection of liquid fuel into the combustor remains the most practical option. Relatively low NOx emissions have been achieved in the SPRF combustor with liquid fuels without external prevaporization through the use of a concentric injector design that relies on airblast atomization [9]. The design of the SPRF combustor is such that the general flame structure and flow features are expected to remain similar even in liquid-fueled operation for comparable inflow conditions. Hence, the most important difference in the operation of the combustor with liquid fuels is the added time required for evaporation, which changes the relationship between the chemical times and mixing times. In general, the NOx emissions from

(nonpremixed) liquid fueled combustors is mainly influenced by the local equivalence ratio [5], i.e., whether the mode of burning is prevaporized (partially premixed) or droplet (diffusion flame) burning. Therefore it is important to estimate the stoichiometry in the flame zone, which is a function of the spray characteristics and evaporation rates. Thus, the second part of this thesis describes the effects of liquid-dispersion and mixing on the performance and combustion characteristics of the SPRF combustor in liquid-fueled operation.

1.3 Thesis Outline

The current work examines the flowfield and its link to the combustion processes that enable the Stagnation Point Reverse Flow (SPRF) combustor to run stably with both gaseous and liquid fuels while maintaining low NOx emissions. To this end, the velocity field and heat release characteristics in this unique reverse flow configuration are investigated. This work also investigates the effects of liquid-dispersion and fuel-product mixing on the performance and combustion characteristics of the SPRF combustor in liquid-fueled operation.

Specifically, this thesis will focus on three major objectives: 1) determine major flow features in the SPRF combustor based on velocity measurements; 2) characterize the interaction between the velocity field and the heat release; and 3) examine the operation of the combustor with liquid-fuel and elucidate the influence of fuel dispersion on the combustion processes in liquid-fueled operation.

A brief overview of flowfields that have some of the features of the SRPF combustor's reverse-flow configuration is provided in Chapter 2, along with background on flame-flow interactions. Chapter 2 also gives a brief background of the different

burning regimes in liquid-fueled operation as well as NOx formation in this mode of operation. Details of the optical diagnostics techniques employed in this study including the experimental set-up, data analysis techniques and sources of error are described in Chapter 3. Chapter 4 details the velocity field of the SPRF combustor in nonreacting and reacting flow as well as the interactions between the flowfield and heat release mechanisms. The turbulence generation and product entrainment characteristics that lead to stable, low emission operation of the combustor are also examined there. Liquid-fueled operation of the SPRF combustor is explored in Chapter 5. In particular, it elucidates the influence of fuel-dispersion and evaporation times on the combustion processes in this mode of operation. A summary of the main conclusions as well as some recommendations for future work are presented in Chapter 6. Lastly, Appendix A contains a brief description of the seeder design and the error analysis for the velocity data is shown in Appendix B.

CHAPTER 2

BACKGROUND

This chapter gives a brief background of various concepts that provide a basis for understanding the ideas presented in this study. The SPRF combustor design represents a unique combination of various types of jet flows. Therefore, Section 2.1 outlines some of the important features of jet flows with and without confinement, coaxial jets and jets in opposed flows. The effect of density changes and heat release on jet flows, as well some background on flow-flame interactions are presented in Section 2.2. Lastly, Section 2.3 describes some relevant spray combustion regimes in combustion as well as factors affecting NOx emissions in liquid-fueled combustors.

2.1 Jet Flows

While there is a significant amount of literature on free turbulent jets, confined jets with coflow or counterflow, jets in cross-flow, and (stagnating) jets exiting onto impingement plates, there have been no previous flowfield studies on a geometry resembling this combustor, with its self-reversing flow. Since the SPRF design does incorporate features of many of the jet flows mentioned above, some background about these flows is presented here.

2.1.1 Free Jets

Early experimental work on turbulent free jets over the whole range of Froude numbers from momentum dominated jets to the pure plume have been reviewed in depth, and similarity and scaling laws have been developed [10 - 11]. The following quantities

have been identified as important parameters in quantifying jet flows: rate of spread, lateral and longitudinal profiles of average velocity, species concentration and turbulent quantities such as fluctuating velocity, turbulent shear and entrainment/mixing characteristics [12, 13, 14].

For the case of free axisymmetric self-preserving turbulent jets, the centerline velocity (U_c) is given by:

$$U_c = BM_0^{1/2}(X - X_o) \tag{2.1}$$

where B, x_0 are constants that depend on the jet exit conditions: x_0 is the virtual origin of the jet and M_0 is the momentum flux at the origin. The centerline jet decay can then be expressed as [13]:

$$\begin{aligned} \frac{U_c}{U_0} &= B_u\left(\frac{X}{D} - \frac{X_o}{D}\right)^{-1} \\ B_u &= \frac{1}{2}\pi^{\frac{1}{2}}B \end{aligned} \tag{2.2}$$

where U_0 is the exit velocity of the jet and D is the jet diameter. For a self-similar round jet, it has been observed that the decay rate varies as $1/X$ when X is normalized with the jet diameter. When this is plotted, it is observed to be a straight line where the slope represents the decay rate and the X-intercept denotes the virtual origin of the jet. Hussein *et al.* [13] noted that for an axisymmetric jet with a top-hat velocity profile, the virtual origin, X_0, is located at $\sim 4D$ and the decay constant, B_u is approximately 5.9 (or equivalently from Eq. (2.2), B=6.7). Xu and Antonio [15] have observed comparable values for round jets issuing from a smooth contraction nozzle, whereas the values of the constants are slightly different for fully-developed pipe jets with similar exit conditions. Several other studies have shown similar results that confirm that while the 1/X decay is

a consistent feature of free jets, the centerline decay constants and the location of the virtual origin are sensitive to the inlet conditions [16-17].

Studies have also shown that the radial spreading rate of free (round) jets varies linearly with X and may be expressed as [15]:

$$\frac{R_u}{D} = C\left(\frac{X - X_0}{D}\right) \tag{2.3}$$

where R_u is the mean half-radius defined as the distance between the radial locations at which the velocity drops to 50% of its centerline value, C is a constant and X_0 is once again a virtual origin. It should be noted that this value may be different from the virtual origin calculated based on the centerline decay rates.

It is also known that density has a considerable effect on the near field turbulence values of jets [12,18]. Variable density jets, such as those encountered in free turbulent jet flames, have different entrainment characteristics - lighter gases are entrained more easily.

2.1.2 Confined/Co-flowing Jet Flows

The effect of confinement and co-flowing streams on the structure of axisymmetric turbulent jets has also been studied. A co-flowing stream is defined as one where the velocity is significantly lower than that of the main jet ($U < 0.1U_{jet}$). Borean *et al*. [19] observed that the variation of the mean velocity and the rate of expansion of a confined jet with a weak co-flow are identical to that of a free jet, which suggests that the inner flow (jet) is not affected by the external flow when the jet velocity is significantly greater than that of the co-flowing stream. A similar result was obtained for the turbulent quantities where only some of the third order moments exhibit a different behavior near

the axis of the flow. In a strong coflow, however, the centerline velocity and the jet width tend to follow a $x^{-2/3}$ and $x^{1/3}$ dependence, respectively [20]. In the case when there is no external coflow velocity, the effect of confinement changes the structure of the jet significantly [21]. It has been observed that the jet decay rates are lower for confined jets compared to that of free-jets as a result of the reduced entrainment rates.

Some studies have also been conducted on confined jet flows impinging on stagnation plates. The amount of air entrained by the jet is then linked to the density ratio, the length of jet development and also to the pressure gradient due to the impact on the plate [22]. It was also found that the entrainment rate is highest when the stagnation plate is located approximately 10 jet diameters from the nozzle exit. This configuration is often found in burner geometries that produce flat stagnation flames. The SPRF combustor, however, differs from this geometry because of the increased distance of the jet exit from the stagnation plate (25 annular diameters in the implementation studied here), and because the impingement plate is located within the confining walls of the system. It should also be noted that the definition of entrainment for free and confined, non-coflowing jets is usually based on the increase in mass flow rate caused by the drag of the jet. This definition, however, lacks a clear meaning in the context of confined coflowing jets where mass flow rate is fixed.

2.1.3 Co-axial Jet Flows

The SPRF combustor when operated in nonpremixed mode adds an additional feature to the flow – the fuel and air form a pair of coaxial confined jets. Extensive literature exists on the flow features of free coaxial jets. The most important parameter influencing jets with coaxial flow has been identified as the momentum ratio between the

inner and annular flows [2325]. Villermaux and Rehab [26] suggest that in coaxial jets with outer to inner velocity ratio higher than unity, the most important parameters controlling the mixing process are the velocity difference between the two streams and the gap thickness of the annular jet. Measurements of NOx emissions in jet diffusion flames with coaxial air [27 - 29] have shown significant reduction of NOx levels. The high shear produced by the high velocity coaxial air has been shown to result in enhanced mixing between fuel and air and also lowers the residence times resulting in lower emission levels. However, little is known about the effects of confinement on coaxial jets.

2.1.4 Jets in Opposed Flow

A rather unique aspect of the SPRF flowfield is that the entering reactant jet is faced with an opposed flow produced by the reversal of the jet fluid at the stagnation region ahead of the closed end. Previous research in this area has been limited to single jets in opposed flows where the two flows are uncoupled, e.g., a jet injected upstream into a wind tunnel (Figure 3).

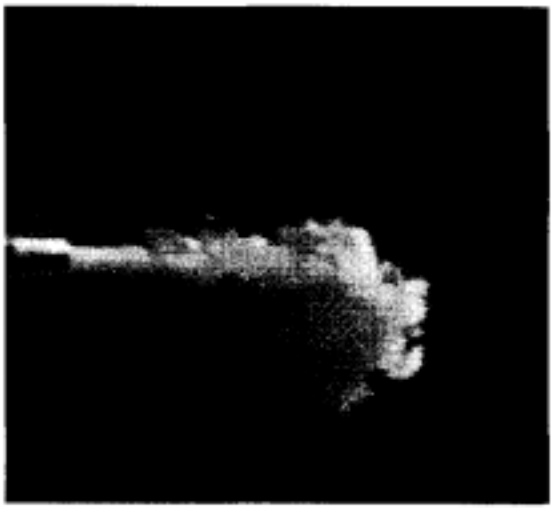

Figure 3. Instantaneous LIF image of a jet in a uniform opposed flow [30].

Experimental studies show that the jet penetrates an axial distance, X_p, before it is deflected backwards (Figure 4). Along the penetration distance, the jet decays more rapidly compared to a free jet and then stagnates at X_p. The penetration distance depends on the velocity ratio of jet to that of the counterflow and a linear dependence on this ratio has been demonstrated to be [30, 3134], i.e.,

$$\frac{X_p}{D} = C\frac{U_j}{U_{opp}} \qquad 2.4$$

where D is the jet diameter, U_j is the jet exit velocity and U_{opp} is the (constant) velocity of the counterflow. The value of the constant, C, varies for different experimental arrangements and has been shown to be between 2.4-2.8 for velocity ratios (U_j/U_0) ranging from 2 to 12.

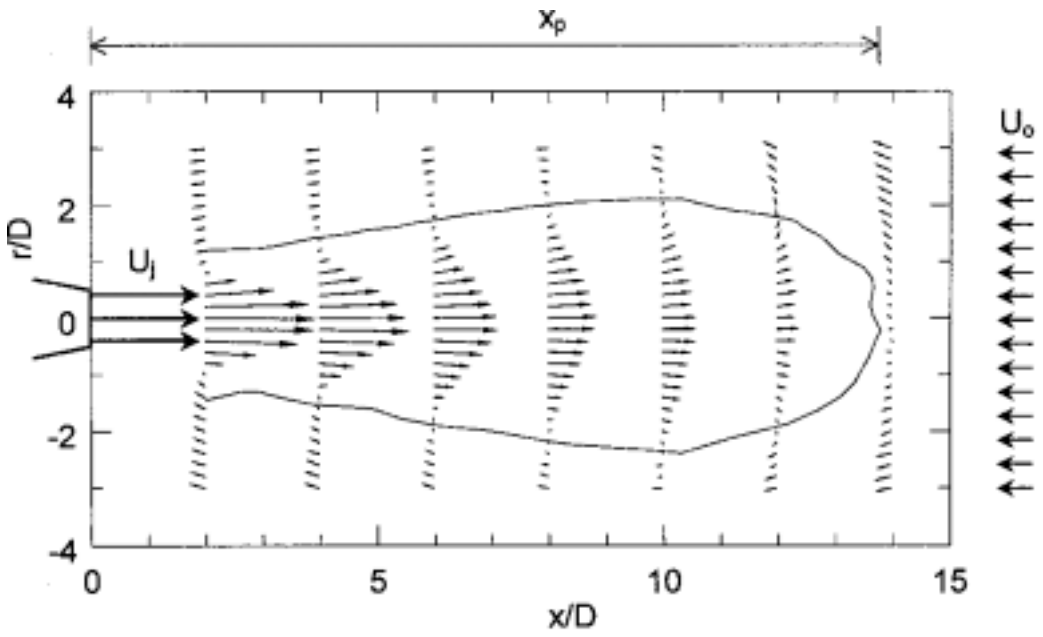

Figure 4. Mean velocity vectors and zero velocity contours of a jet in a uniform counterflow [33].

It was also found that the turbulent mixing process in this configuration depends on the velocity profiles at the nozzle exit and the excess momentum of the jet, which is defined as ($U_{opp}/U_j - U_{opp}$), where U_{opp} is the velocity of the uniform opposing (air) stream and U_j is the velocity of the main jet at the nozzle exit [35, 36].

2.1.5 Turbulent Flow –Flame Interaction

The interaction between turbulent flow and flames is very complex and is not fully understood. The generation or suppression of turbulence due to heat release from a flame can have important implications on the stability and emissions performance of combustors. Some of the key mechanisms of flame turbulence as described by Ballal [37,38] are listed here.

1. Propagation of a flame through the unburnt gas mixture accelerates the hot gases creating mean and fluctuating shear between adjacent streamlines producing what may be termed as “shear generated turbulence” within the flame. This effect has been to shown to be the predominant flame generated turbulence mechanism in tightly enclosed/ducted flames [39].
2. The rise in temperature across the flame front also results in higher viscosity of the hot gases behind the flame front, thereby increasing the viscous dissipation of turbulent kinetic energy and quickly damping small scale fluctuations. Since measurements in practical combustors suggest the dominating influence of small scale random turbulence, suppression of small scale fluctuations can considerably affect the performance of combustion systems.

3. Volumetric expansion of burnt gases produces velocity divergence, which lowers the overall turbulent kinetic energy due to dilation effects. This mechanism tends to dominate in unconfined flames such as jet flames.
4. The relative magnitude and direction of the density gradients setup within the flame influence the diffusion of turbulent kinetic energy and can thus lead to production or suppression of turbulence in a flame.
5. Lastly, pressure related processes such as pressure fluctuations correlated with volume increases, which are acoustic in nature, can result in combustion generated turbulence.

The mechanisms listed above operate simultaneously, and their contribution to production or dissipation of turbulent kinetic energy is a strong function of the flame geometry, the system boundaries (enclosed/open flames) and reactant mixing (i.e., premixed or diffusion flame). Further it has been shown that in practical combustion systems, fluctuating mixture fractions, size of the recirculation zone in bluff body stabilized flames, swirl numbers and two-phase combustion can further affect the flow-flame interactions [40].

2.2 Liquid-Fueled (Spray) Combustion

As noted in Chapter 1, the second major goal of this thesis is to extend the results of the gas-phase studies to understand operation and performance of the SPRF combustor with liquid-fuels. The objective here is to determine the combustion characteristics and the effects of the fuel dispersion on the NOx emissions from the combustor in this mode

of operation. Hence the following sections provide some background on spray combustion and pollutant formation in liquid systems.

2.2.1 Lowering NOx emissions in Liquid-Fueled Operation

Since thermal NOx formation is highly dependent on temperature, liquid fuels tend to produce higher NOx compared to gaseous fuels. This occurs because there is always a potential for near-stoichiometric combustion when burning liquids even at lean global equivalence ratios [5]. A common approach to lowering NOx emission in liquid operation is premixed, prevaporized combustion, where the liquid fuel is externally vaporized and mixed with air before entering the combustor. However, this option poses major safety issues because of flash back concerns and also increases the overall complexity of the combustion system. Therefore, spray combustion systems are preferred when operating with liquid fuels. In such systems, atomization is an important issue in NOx formation since larger droplets are more likely to support envelope diffusion flames that burn at near-stoichiometric conditions whereas small droplets that are well-dispersed tend to impede the formation of envelope flames so that most of the combustion occurs in a partially premixed - like mode [41].

2.2.2 Combustion Regimes in Liquid-Fueled Operation

Droplet or spray combustion can be characterized in different regimes depending on the group combustion number, G defined as follows [42, 43]:

$$G = 3\left(1 + 0.276\,\mathrm{Re}^{\frac{1}{2}}\,Sc^{\frac{1}{3}}\right)LeN^{\frac{2}{3}}\left(\frac{R}{s}\right) \qquad 2.5$$

where *Re* is the Reynolds number, *Sc* is the Schmidt number, *Le* is the Lewis number, *N* is the total number of droplets in the cloud, *R* is the instantaneous average droplet radius of the cloud and s is the spacing between the droplets.

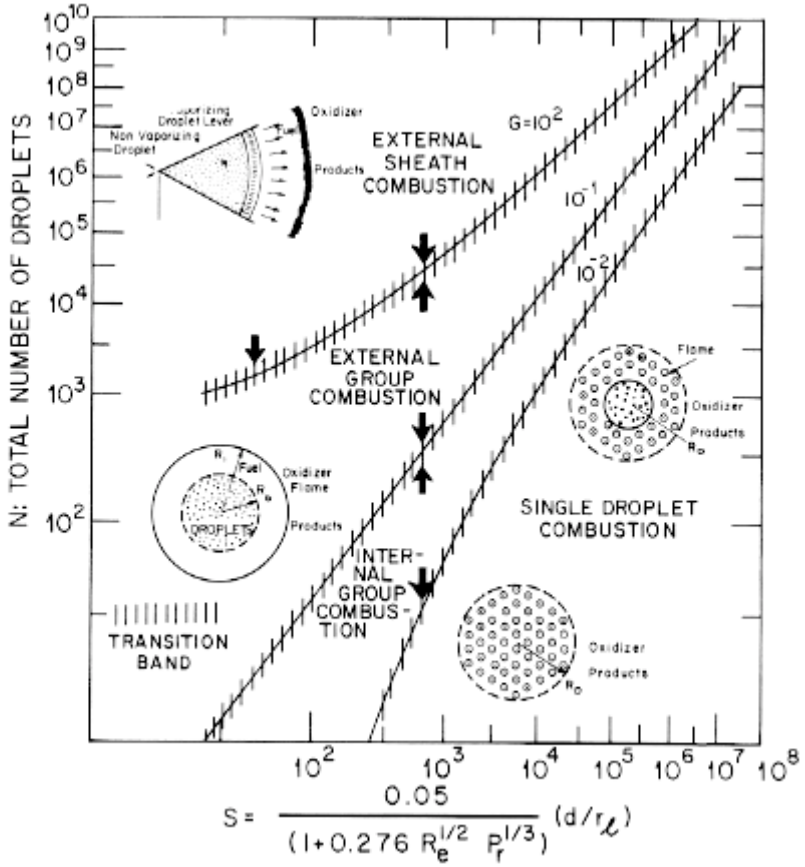

Figure 5. Different regimes of spray combustion based on group combustion number [43].

There are two main regimes of interest in the present study. First is internal group combustion ($10^{-2}<G<1$), which involves a core within the droplet cloud where evaporation is occurring while the core is totally surrounded by flame. Outside the core, each droplet is enveloped by an individual flame. Second is external group combustion ($1\leq G<10^2$), where a single flame envelopes all droplets. This type of burning is observed

when the size of the droplet core increases (large group numbers) and is often observed in industrial burners and most gas-turbine combustors.

Rangel and Sirignano [44] have studied the combustion of droplet streams in a gas flow and have shown that multiple flames can exist, i.e., one can observe both a partially premixed flame as well as diffusion flames when bigger droplets penetrate through the premixed flame before complete vaporization has occurred. The partially premixed flame is established when a small group of droplets evaporate and then burn inside the cloud while the bigger droplets survive longer and burn as diffusion flames further downstream. This describes the combustion process in the internal group combustion regime noted above.

CHAPTER 3

EXPERIMENTAL AND DATA ANALYSIS APPROACHES

This chapter describes the various diagnostic techniques, experimental set-ups and data analysis techniques that are employed in this study. The geometry of the SPRF combustor and the different injector configurations are described in Section 3.1. The second section details the instrumentation, set-up and data analysis procedures for the various optical diagnostic techniques employed here. These include PIV (particle image velocimetry), which is used to characterize the velocity field, laser scattering from fuel droplets, which provides information on liquid fuel dispersion, as well as Planar Laser Induced Fluorescence (PLIF) of OH radicals and chemiluminescence from CH^* and OH^* to visualize hot product gases and the combustion zone.

3.1 Description of SPRF Combustor

3.1.1 Combustor Design

The SPRF combustor used for the current studies is a laboratory scale, atmospheric pressure device (Figure 6). The geometry of the combustor is very simple, consisting of a cylindrical tube (GE fused quartz) 300mm long with one end open and the other closed. The inner diameter of the combustor used in this study is 70mm. The tube is closed at the one end with a quartz disk so as to allow the laser sheets for the diagnostics to enter the combustor. The base plate is fit snugly inside the quartz tube so that there is no measurable leakage of fuel/air through the closed end. Fuel and air enter the

combustor through a concentric tube injector located centrally in the combustor. The inner tube is centered with respect to the outer injector annulus with the help of three set-screws, and the co-annular injector is centered and aligned with the combustor axis as well as possible. The injector design is described more in detail in the next section. To minimize heat losses, the combustor can be insulated with a close fitting, hollow alumina cylinder (ZIRCAR AL-30AAH) cut into four sections. To facilitate optical access, a 180° window is cut out of one of the sections, which can be placed at different axial locations. Thus most of the optical measurements are acquired one-quarter of the combustor at a time, and the complete field is derived by assembling them together.

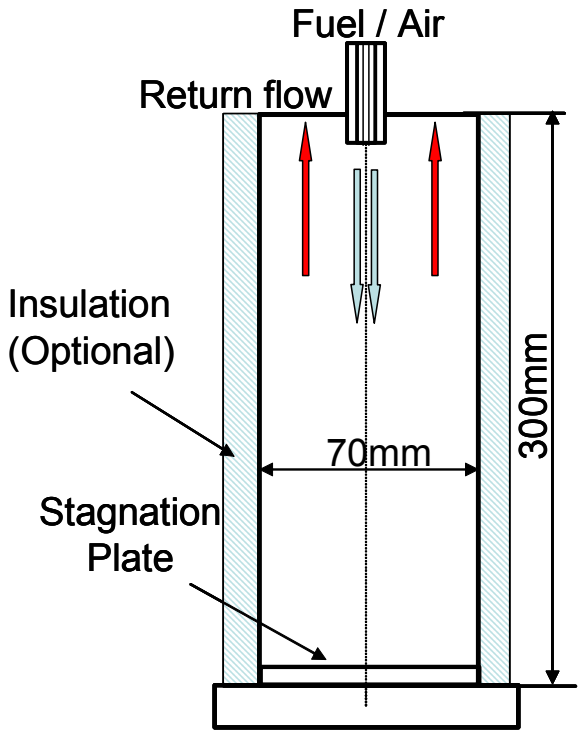

Figure 6. SPRF combustor design and dimensions.

The reverse flow geometry of the SPRF combustor produces a rather unique flowfield. Contrary to most combustors, the reactants and products enter and leave this

combustor at the same (open) end. In the investigated configuration, the reactants are injected along the combustor center line, while the products flow in the reverse direction to exit the combustor, allowing the outflowing products and inflowing reactants to come into direct contact in a thin shear layer. Because the exiting products flow directly over the reactant injector in the SPRF design, they produce "internal" preheating of the reactants before injection.

3.1.2 Injector Design

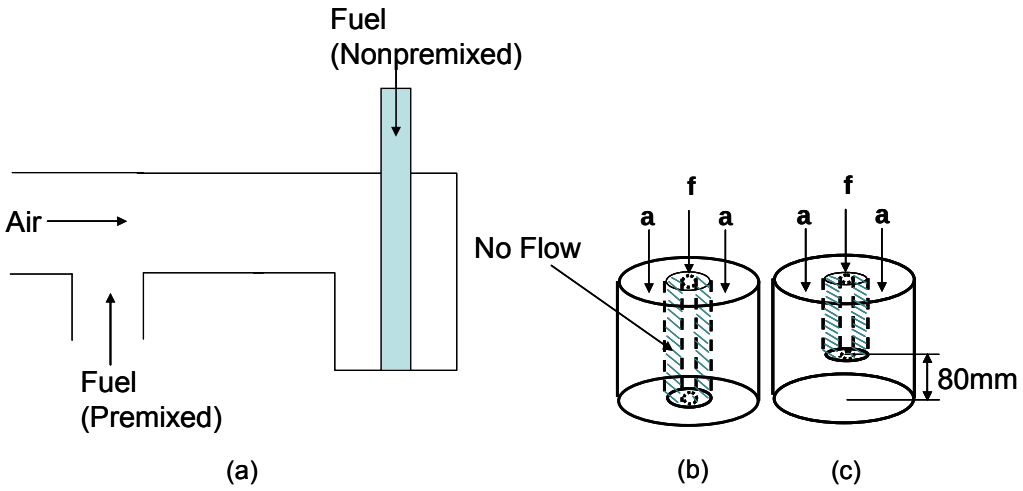

Figure 7. Schematic of injector used for: (a) Gas-fueled operation; and for liquid-fueled operation in a (b) Flush configuration and a (c) Retracted configuration.

As noted above, the reactant injector employs stainless steel concentric tubes centered along the axis of the combustor. The injector is placed such that it is located approximately 19mm downstream of the exit plane of the combustor.

Gas-Fueled Injector

The coaxial design of the injector allows for easy switching between premixed and nonpremixed modes of operation for gaseous fuels. For nonreacting flow measurements, air enters the combustor through the annular passage; there is no flow through the inner (fuel) tube which is closed far upstream to prevent entrainment of reactants or products into the injector. Similarly for premixed operation, the natural gas-air mixture is injected through the injector's annulus; fuel and air are introduced well upstream of the injector exit to ensure complete premixing. In the nonpremixed mode, fuel is injected through the inner tube and air through the annulus; no fuel-air mixing can occur until the flows enter the combustor. Fuel and air flow rates are controlled separately with calibrated rotameters.

Liquid-Fueled Injector

A tri-concentric injector design is employed for liquid-fueled operation (Figure 7). The fuel is pumped through a 500 μm tube centered within a 6 mm tube with no flow in the outer region. The whole arrangement can be traversed inside a third concentric tube which forms an annular passage for air flow. The fuel tube is centered with respect to the outer air annulus using set-screws. The air stream surrounding the fuel facilitates atomization of the fuel jet. Care is also taken to ensure that the whole injector is centered with respect to the combustor. Air flow rate is monitored and controlled using a calibrated rotameter. The fuel flow rates are calculated based on measurements of excess O_2/CO_2 in the product gases with a portable gas analyzer (Horiba CEMS - PG250). As the inlet air is not preheated, the combustor is ignited with a premixed mixture of natural gas and air and the liquid fuel is introduced gradually before switching to fully liquid

operation. In this study, two separate fuel tube locations have been investigated – (1) liquid fuel injector is flush with the exit of the air injector (flush configuration) and (2) liquid fuel injector is retracted to ~80mm above the exit of the air injector (retracted configuration). A summary of the combustor and injector dimensions in the various configurations is given in Table 1.

Table 1. Summary of SPRF combustor and injector dimensions.

Combustor Dimensions (mm)	
Length	300
Inner diameter	70
Injector Dimensions (mm): Gas-Fueled Operation	
Air tube: inner diameter	12.5
Air tube: outer diameter	17
Fuel tube: inner diameter	4.7
Fuel tube: outer diameter	6.25
Injector Dimensions (mm): Liquid-Fueled Operation	
Air tube: inner diameter	12.5
Air tube: outer diameter	17
Centering tube – no flow: outer diameter	6.25
Fuel tube: inner diameter	0.5
Fuel tube: outer diameter	1

3.2 Details of Diagnostics and Analysis Procedures

Several optical diagnostic techniques are employed in this study to understand the flowfield and combustion processes in the SPRF combustor. Each of these techniques is

detailed in this section along with the data analysis procedures as well as the major sources of error which can affect the accuracy of the measurements.

3.2.1 Temperature and Emission Measurements

As noted earlier, the SPRF combustor produces a reverse flow configuration so that the exiting products flow over the injector and preheat the reactants. The temperature of the incoming gas is monitored with an unshielded K-type thermocouple ~ 1.5mm in diameter. The thermocouple is placed in the center of the air annulus away from the injector walls and is roughly 5mm upstream of the injector exit. The temperature of the exhaust gases is measured with a shielded K-type thermocouple that is placed along with the gas sampling probe approximately 25mm inside the combustor in the exhaust flow. Both thermocouples are removed before taking imaging measurements to prevent laser scattering from the probes.

The exhaust gases from the SPRF combustor are sampled with an uncooled ceramic probe, and a portable gas analyzer (Horiba CEMS - PG250) is used to determine the gas composition. The PG-250 system provides simultaneous measurements of CO, CO_2, O_2, NOx and SO_2 in flue gas samples. In this study, the system is not calibrated for SO_2 measurements. The PG-250 employs non-dispersive infrared detection of CO and CO_2 and an electrochemical cell for O2 measurement. The NO_x emission is estimated with the chemiluminescence NO detector which uses a low-temperature NO_2 to NO converter. In liquid-fueled operation, the measurements of excess O_2 in the product gases are also used to calculate the fuel flow rates. The Horiba system is calibrated every week against a standard set of gases at different concentrations and the system is able to provide repeatable readings within 0.5% of full scale.

3.2.2 Particle Image Velocimetry (PIV)

In contrast to conventional velocity measurement techniques such as LDV (laser Doppler velocimetry), and hotwire anemometry, which provide single point measurements, PIV is a non-intrusive technique that can be used to obtain instantaneous whole-field, spatially correlated measurements of flows. This technique is also a more direct measure of the velocity of a fluid (compared to hotwire anemometry) since it depends directly on the displacement of the tracer particle during a given time period. PIV has been successfully applied to both nonreacting and reacting flows to study the velocity field in various flow geometries [45,46].

3.2.2.1 PIV Set-Up

The PIV set-up is made up of three major parts - a source of illumination, a seeder that generates the tracer particles required for the measurements and an interline CCD camera for image acquisition. A schematic of the experimental set up used in this study is shown in Figure 8.

The illumination is provided by a laser sheet generated with light produced from the 2^{nd} harmonic output (532nm) of a dual-head, pulsed Nd:YAG laser (Surelite I-10). Each laser head is capable of providing light pulses with 120mJ of energy at the rate of 10 Hz. Since the laser pulse is very short (FWHM of 8ns) it effectively freezes the flow even up to supersonic velocities. The beam is converted into a thin sheet (~0.6 mm) with two cylindrical lenses, and enters the combustor from the closed end (Figure 8).

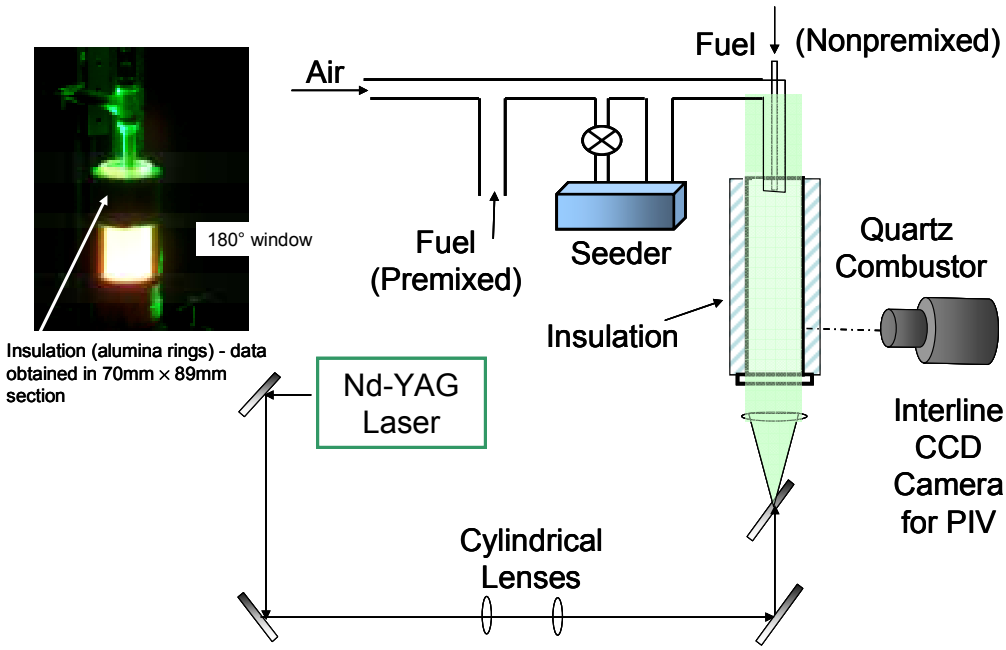

Figure 8. Schematic of PIV set-up.

The scattering efficiency is mainly dependent on the difference in refractive index between the tracer particle and the flow medium. Hence the use of solid or liquid particles in gaseous flows and use of solid particles or gas bubbles in the case of liquid flows is preferred. The velocity lag of a particle in a continuously accelerating fluid is given by:

$$U_{lag} = U_p - U = d_p^2 \left(\frac{\rho_p - \rho}{18\mu} \right) a$$

where U_p denotes the particle velocity, U denotes the actual fluid velocity, a is the fluid acceleration ρ_p is the density of particle, ρ and μ are the density and dynamic viscosity of the fluid respectively.

The large relative difference in density between the fluid and tracer particles (usually about a factor of 10^3) demands that the diameter of the particles to be very small (~ 1 μm) to assure proper tracking of the fluid motion. Hence, in the present study, the air

is seeded with 0.3 to 2 micron aluminum oxide particles dispersed with a fluidized bed seeding generator. A more detailed description of the seeder design is provided in Appendix A. Alumina particles are used in this study because they have a very high melting point (2300 K) which makes it possible for the particles to survive through the flame thus enabling velocity measurements in both unburnt and burnt gases. In order to get valid vectors in the PIV measurements, the seeding density is maintained so that there are at least 10-15 particles per interrogation area in the burnt gases where the seed density tends to drop due to thermal expansion. Additionally the seed particles are also baked for 6 to 8 hours to remove moisture and prevent particle agglomeration.

The correlated pairs of particle scattering images are acquired using a 12 bit MicroMAX Interline CCD camera from Roper-Scientific. The full chip resolution of the camera is 1300 × 1030 pixels, and it is equipped with a 50 mm Nikkor lens (f: 1/1.8) for image capture. The timing between the two laser heads and the camera shutter is synchronized with a digital pulse generator (Stanford, DG535). Pulse delays between the image pairs vary from 3 to 11 μs for different regions of the combustor. The images are acquired for 70mm × 89mm segments of the combustor and then spliced together to produce the complete combustor velocity field.

3.2.2.2 PIV Data Processing and Analysis Procedures

A commercial software package (Insight 6, TSI) is used to calculate the velocity field. First, the raw PIV images are preprocessed to remove background noise, for example from wall scattering. In order to prevent an unacceptably large background scattering signal caused by deposition of the seed material on the combustor walls, the combustor was cooled and cleaned after every 50 image pairs. Following background

subtraction, the images are further filtered to remove interrogation spots that do not contain any particle images. This is done by setting an "average spot intensity" value so that spots without particles are below a certain threshold value whereas spots with particle images are above the threshold. The correct threshold value is decided by monitoring the PIV processor and varies for each data set.

An FFT based cross-correlation technique is employed to find the average particle displacement in a 64×64 pixel region with a Nyquist grid that gives a 50% overlap in the interrogation areas yielding a total of 1209 velocity vectors. The data was also verified by varying the size of the interrogation areas to eliminate any bias errors in the velocity measurements. The reverse flow geometry of the SPRF combustor produces a unique self-reversing flowfield with large velocity gradients both in the axial and radial directions. Therefore, in each quarter the PIV data is obtained with 3 different time delays between the image pairs so as to help capture the forward and return flow velocities accurately. The particle displacements are obtained with a 0.1 pixel accuracy using a Gaussian sub-pixel interpolation algorithm. Each vector represents the average velocity in an interrogation volume $2.19 \times 2.19 \times 0.6$ mm^3.

Even if all steps of the image acquisition and processing are optimized, there is a non-zero probability that we obtain spurious velocity vectors with the PIV interrogation algorithm. The most common reasons for the occurrence of these spurious vectors are low local particle image density, non-uniform illumination of the image and background noise from reflections. Even with highly homogeneous seeding it is possible that portions of the image do not contain useful information because of the lack of particles or out of plane displacement of the particles. Therefore, vector validation is performed to separate

the vectors corresponding to correct measurements with uncertainty from spurious vectors. The two main techniques used in this study are:

(1) **Maximum displacement validation:** There are limitations to the maximum measurable displacements in most standard correlation algorithms. This is usually taken to be ~25% of the interrogation area size [47]. Thus the measured values that are outside this range are rejected.

(2) **Peak to noise peak ratio validation:** The highest correlation peak is used to locate the particle displacement while the second highest peak is a noise peak caused by the random pairing of images from different particles. The ratio of the displacement peak height to the noise peak height shows how much the displacement peak stands out above the noise and is a measure of the confidence that the selected peak is the correct peak. In this study, the Peak/Noise peak ratio is set to 10 to ensure that the particle displacement is as accurate as possible.

The velocity data thus acquired can be post-processed further to obtain an estimation of vorticity fields, streamlines, zero velocity contours, etc. To obtain information about the sizes and locations of large and small scale eddies in the flow based on the instantaneous velocity fields simple scale decomposition techniques such as Reynolds decomposition or Proper Orthogonal Decomposition (POD) may be applied [48]. In the present study, a simple spatial correlation analysis is performed in order to obtain information about the sizes of large-scale coherent structures in the different regions of the combustor. It should be noted that this technique provides only a rough estimate of the sizes of the coherent structures and a more accurate measure of the

structure sizes can be obtained with the aforementioned techniques. The length scale of the coherent structures is calculated from the instantaneous PIV data with the following equations.

$$R_L = \frac{\overline{U(x) \bullet U(x+r)}}{u'(x)u'(x+r)}$$
$$L_c = \int_0^{\infty} R_L(r)dr \qquad 3.1$$

The correlation coefficient R_L is calculated based on the instantaneous axial velocity, U and the root mean square of the axial velocity (u') over the correlation length, r. Although the calculation of correlation length (L_c) requires integration of the correlation coefficient over an infinite extent, here the calculations are restricted to some distance within the computational domain. In practice, the correlation coefficient does not tend asymptotically to zero but rather oscillates above and below as the correlation length increases. Therefore, in this study, the limits of integration are restricted to the location at which the value of the correlation coefficient first crosses zero. Thus we estimate the length over which the axial velocity remains correlated: this is an indication of the sizes of the large scale structures in the flow.

3.2.2.3 Sources of Error and Analysis of Uncertainties in PIV Measurements

The PIV measurement uncertainties due to the evaluation algorithm as well as thermal gradients in the flow are assessed here. The accuracy of the algorithm is calculated based on the smallest measurable pixel displacement for the Gaussian sub-pixel interpolation technique ~ 0.3 pixels. The current PIV experiments are designed to have pixel displacements between 8-10 pixels within the 64 × 64 pixel interrogation area, which yields a 3.8% uncertainty in the particle displacements.

Temperature gradients in reacting flows also act as a source of error in the PIV measurements through beam steering effects, image distortion and thermophoresis. Significant image blurring and distortion occurs when the object plane is a far behind the density gradient region. Since the measurements presented in this study are taken in a plane passing through the flame and not a substantial distance away, the image distortion effects are found to be negligible.

The angular deflection in a laser beam caused by a density gradient in a direction perpendicular to the beam is given by:

$$\varepsilon = \frac{L}{\delta}\frac{n(T) - n_0}{n_0}$$

where ε is the deflection angle towards the region of highest density, L is the length along the beam axis, δ is the width of the density gradient or flame thickness and n is the index of refraction of the fluid. The index of refraction (n) as a function of temperature is given by:

$$n(T) = K\frac{\rho(T)}{\rho_0} + 1 = K\frac{T_0}{T} + 1$$

Since n_{air} at 300K is 1.000298, K = 0.00298, n_{air} at flame temperatures (2000K) is 1.00199. Based on these values it is estimated that the deflection angle is approximately 0.0016 radians which corresponds to a deviation of only 0.3mm (half of the sheet thickness) as it reaches the top of the combustor. Therefore, the uncertainty due to beam steering effect is not expected to be significant in this study.

Lastly the effect of thermophoresis on measurement uncertainty is briefly explored. The tendency of a particle suspended in a gas with a temperature gradient to drift down the gradient is called thermophoresis [49]. This effect causes the particle velocity perpendicular to the flame to lag the actual fluid velocity resulting in erroneous measurements. The resulting lag in particle velocity is termed thermophoretic velocity. The thermophoretic velocity has been shown to be dependent on the Brownian diffusivity of the particle as well as the local temperature gradient [49]. Sung *et al*. and Muniz *et al*. [46,49] have estimated this value to be ~ 14cm/s for 0.4μm TiO_2 and Al_2O_3 particles in flow with a thermal gradient of 2000K/mm at a temperature of 1300K. In the SPRF combustor, since the reactants are preheated by the outgoing product gases, the thermal gradients are not expected to be very strong. Also, since the size of the particles used in the present study is much larger (1-2 μm), the thermophoretic velocities are expected to be even lower of the order of about 8cm/s. Therefore, the error in measurement due to the particle lag can be neglected in most parts of the flow except near the stagnation region.

The accuracy of the PIV measurements is further affected by the uncertainty in the timing generators and laser jitter. However, both of these values are of the order of picoseconds and the time delay between the frames is at least a few microseconds. It is important to note that since the volumetric flow rate of reactants in the SPRF combustor is very high, the timing for the PIV system is adjusted to capture the large axial velocities in the jet. Since the radial velocities are likely to be very small in comparison except in the stagnation region, the errors in the radial velocity measurements are very large (≥50%).

Therefore the net uncertainty in the velocity measurements can be estimated based on the following equation:

$$\frac{\Delta V}{V} = \sqrt{\left(\frac{\Delta x}{x}\right)^2 + \left(\frac{\Delta t}{t}\right)^2}$$

$$\Delta x = 0.3\ pixel,\ x = 8\, pixels,\ \Delta t = 1\times10^{-12}\, s,\ t = 1\times10^{-6}\, s$$

Thus, the maximum uncertainty in the (axial) velocity measurements in the present study is approximately 3.8%. Since the flow in the SPRF combustor is highly turbulent in nature, the statistics of the velocity field are obtained by averaging several instantaneous fields. The error analysis for the statistical errors in the data is deferred till later (Appendix B).

3.2.3 Droplet/Laser Scattering

Scattering of laser light from liquid droplets can be used as a means to identify the location of fuel and to obtain a qualitative understanding of the fuel dispersion and mixing effects. In the present work, laser scattering from fuel has been employed along with chemiluminescence imaging/OH-PLIF measurements to visualize the fuel distribution and heat release zones simultaneously.

3.2.3.1 Laser Scattering Set-Up

In this study, mixing of unburned, cold fuel with air and hot products was analyzed by seeding the fuel with 3-5 μm diameter olive oil droplets and collecting the scattered laser light with the same optical system used for PIV. The oil droplets were generated using a standard laskin nozzle based aerosol generator [50]. In liquid-fueled

operation, the distribution of liquid inside the combustor as well as the mixing of unburned, cold fuel with hot products is investigated by illuminating the liquid fuel jet with a laser sheet generated by the optical set-up detailed in the previous section. The scattered light is detected normal to the laser sheet with the same MicroMAX CCD camera and lens system described earlier (Figure 9).

3.2.4 CH/OH Chemiluminescence Imaging

Chemiluminescence emission has commonly been used as a measure of chemical reaction rates as well as heat release rates and provides information on the presence and strength of the combustion processes in a specific region of a combustor. Chemiluminescence intensities relate to rates of production and depletion of the particular species. These rates vary with reaction pathways which are a function of equivalence ratio. Hence, the signal intensities can also be related to the equivalence ratio in the combustion zone.[51, 52, 53, 54]

3.2.4.1 Simultaneous Chemiluminescence/ Droplet Scattering Set-Up

The natural chemiluminescence from the combustor is imaged with an intensified camera (Princeton Instruments ICCD-576-S/RB-E, 18 mm intensifier, 384×576 pixels) in both the gas-fueled as well as the liquid-fueled set-ups. The CH* chemiluminescence and a portion of the CO_2* chemiluminescence that occurs in the same spectral region are collected by placing an interference filter (430±5 nm) in front of the camera (Figure 9).

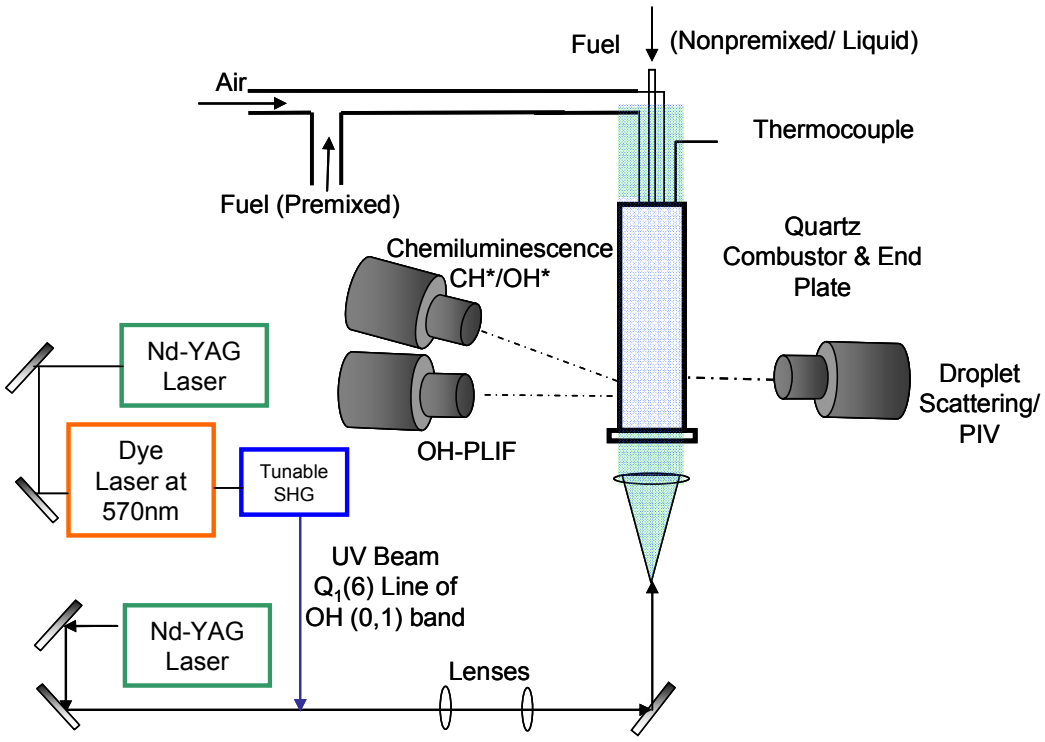

Figure 9. Chemiluminescence, droplet scattering and OH-PLIF set-up.

For gas-fueled operation, the intensifier gate of the chemiluminescence camera is synchronized with the OH-PLIF system (described in the next section), such that the exposure begins 100 ns after the laser pulse and lasts 250 μs. To achieve simultaneous imaging of fuel droplets and chemiluminescence in liquid-fueled operation, a similar set-up is used where the camera is synchronized with the droplet-scattering system. In both cases the two cameras are aligned such that the angle between them is as small as possible and their fields of view are matched to include the entire length and width of the combustor.

Separately to study the OH* chemiluminescence from the combustor when it is operating with liquid Jet-A, a second intensified camera (PI-MAX, 1024×256 pixels) equipped with a UV-Nikkor lens (105mm, f/4.5) and a Schott glass filter (WG308) is

used. During this experiment, the droplet scattering system is disabled and the two chemiluminescence cameras are synchronized with a DG-535 pulse generator.

3.2.4.2 Chemiluminescence Data Analysis

In order to obtain an estimate of the equivalence ratio distribution in the flame zone, the CH* to OH* chemiluminescence ratios were obtained by taking the ratio of the intensities of the CH* field to the OH* intensities at every point in the combustor. Both the CH* and the OH* chemiluminescence images are background subtracted to remove some of the CO_2* radiation. Also, the ratios are obtained conditioned upon the existence of an OH* signal (over the background noise) above a certain threshold at that point: this ensures that the CH*/OH* do not tend to infinity.

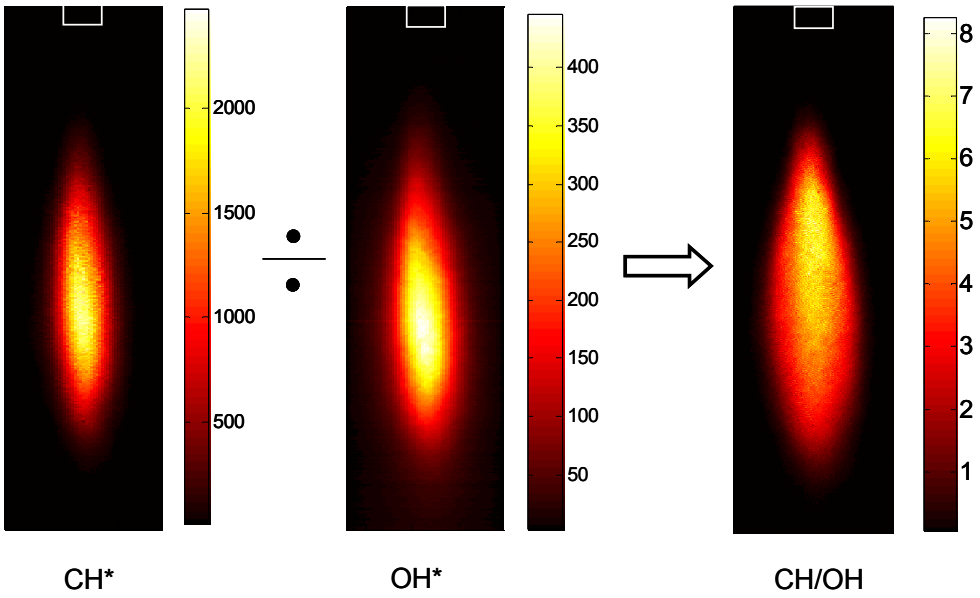

Figure 10. Sample image of average CH*/OH* distribution in liquid-fueled operation at ϕ =0.75 and m_{air} = 8.1g/s.

3.2.5 Planar Laser Induced Florescence (OH-PLIF)

Planar Laser Induced Fluorescence (PLIF) of OH radicals has been used to visualize a cross sectional region through the flame providing information about the combustion process by demarcating the regions of reactants (no OH signal) and the hot products regions(OH signal) [55].

3.2.5.1 OH-PLIF Set-Up

OH fields are determined with a PLIF system tuned to excite the $Q_1(6)$ line of the $A^2\Sigma^+(\nu'=1)\leftarrow X^2\Pi(\nu''=0)$ band at 282.93 nm. This line is chosen here due to its relative insensitivity to temperature. Thus most of the signal change may be attributed to change in the OH concentration. The excitation radiation is produced by frequency-doubling the output of a tunable (Lambda Physik) dye laser, pumped by the second harmonic of a Nd:YAG (Figure 9) laser. The laser beam, with a pulse energy of roughly 17 mJ, is expanded into a sheet 69 mm wide and 300 μm thick with three fused silica lenses. The laser sheet passes through a diametrical plane and illuminates nearly the whole width and length of the combustor. The emitted fluorescence light is detected normal to the sheet with a 25 mm intensified camera (PI-MAX, 1024x256 pixels) equipped with a UV-Nikkor lens (105mm, f/4.5). Schott glass filters (WG305, UG11) placed in front of the lens limit the detected fluorescence to the range 300-370 nm. A pixel resolution of ~300 μm is obtained with this configuration. In liquid-fueled operation, range of wavelengths over which the fluorescence signal is detected is restricted to 308 ± 5nm to avoid interference from Jet-A fluorescence.

3.2.5.2 OH-PLIF Data Analysis

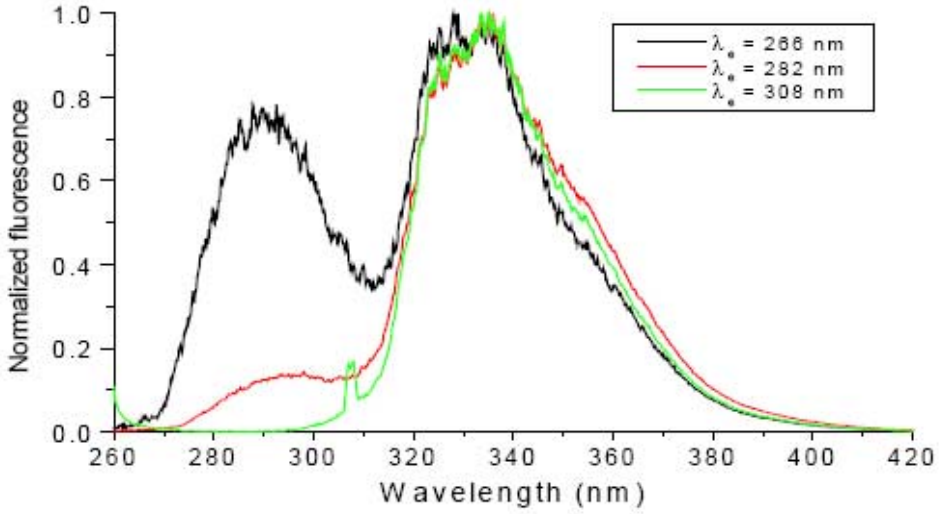

Figure 11. Spectra of kerosene fluorescence at 450K and 1atm for difference excitation wavelengths [56].

In the present study, the OH field obtained with the PLIF system is mainly used to provide a qualitative understanding of the product entrainment and reactant-product mixing in the SPRF combustor. In liquid-fueled operation, excitation of Jet-A at 283nm results in fluorescence of kerosene and other components of Jet-A and it occurs in the same spectral region as that of OH (Figure 11)[56]. Therefore to analyze the PLIF field in liquid-fueled operation, it is necessary to identify the regions where fluorescence of liquid/gaseous Jet-A occurs.

To achieve this, the laser line is tuned away from the $Q_1(6)$ line and the excitation wavelength is lowered to 266nm. The fluorescence light emitted at 308±5nm is then collected and analyzed. Figure 12 shows simultaneous droplet scattering data together with the PLIF field. As seen, the data shows that most of the fluorescence signal occurs in

a narrow region where the liquid fuel is present. Thus, it is possible to separate the Jet-A fluorescence signal from the OH-fields in the combustor.

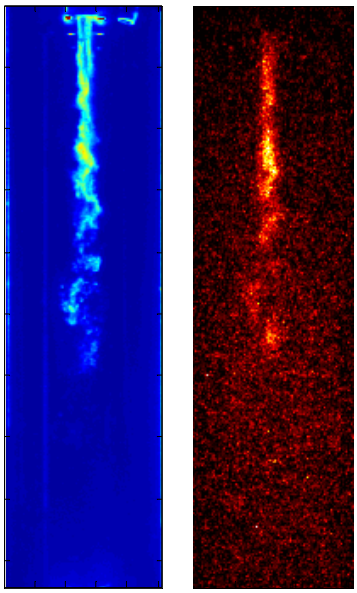

Figure 12. Simultaneous laser scattering and kerosene (Off-OH) PLIF in liquid-fueled operation.

CHAPTER 4

FLOWFIELD OF THE SPRF COMBUSTOR

This chapter describes the results of an investigation to understand the interaction of the flowfield and combustion processes resulting from the unique geometry of the SPRF combustor. We begin by investigating the nonreacting flowfield to identify the major flow features such as location of the shear layers and stagnation regions and then quantify some of the important parameters such as turbulence levels, jet decay rates and shear layer growth in this type of confined, stagnating, self-reversing jet flow (Section 4.1). Next, the interaction between the flowfield and heat release is examined by comparing the nonreacting case with the premixed reacting flowfield (Section 4.2). Lastly, the key similarities/differences in the flowfield between nonpremixed and premixed reacting flows are explored in Section 4.3 and the operation of the SPRF combustor is explained based on the flowfield characteristics.

4.1 Nonreacting Flowfield

The time-averaged flowfield, based on 300 instantaneous PIV images, is shown in Figure 13(a) as a combination of axial velocity contours and interpolated streamlines for nonreacting flow entering at a mass flow rate of 8.1g/s corresponding to a Reynolds number of ~ 65,000. It should be noted that the streamlines may appear discontinuous in some locations. This is because the streamlines are interpolated for each quarter of the combustor (since the data is acquired separately) and then assembled together. The nonreacting flow consists of only air entering through the outer annulus of the coaxial

injector. As seen from the contour, the jet enters the combustor with a peak velocity of approximately 64m/s and rapidly slows down as it moves downstream of the combustor due to the presence of the stagnation plate. As observed from the streamlines, the jet stagnates and reverses approximately 60mm upstream of the end plate for this case. On average, large recirculation vortices are present between the inflow and the outflow in the regions 45mm<X<130mm, which could cause entrainment of the return flow into the incoming jet stream.

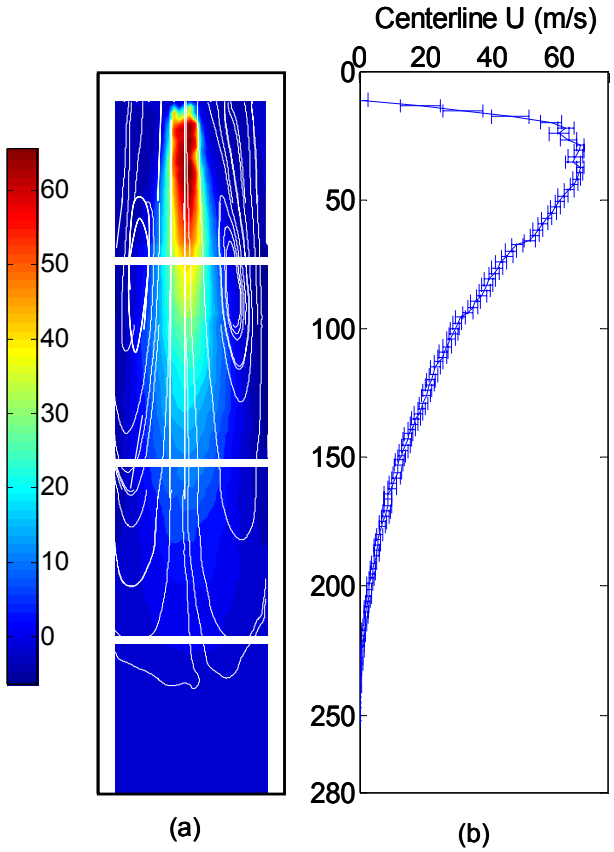

Figure 13. (a) Mean axial velocity contours (in m/s) and calculated streamlines, and (b) Measured centerline variation of mean axial velocity (each data point shown with error bars indicating the precision based on 95% confidence levels).

Figure 13(b) shows the variation of the mean axial velocity (U_c) along the centerline. The mean data are shown with error bars representing the precision

uncertainty based on 95% confidence. At best, the precision is ~5%, as compared to the 3.8% accuracy estimated in Chapter 3. Therefore, only precision uncertainty is shown throughout the rest of this chapter. As mentioned earlier, in the nonreacting flow, there is no flow through the central tube of the injector and all the flow enters the combustor through the annulus. The inner tube acts like a cylindrical cavity, into and out of which the incoming gas can flow and circulate. As the annular jet leaves the injector, it is slowed down by the presence of the cavity. This creates a small recirculation bubble at the tip of the injector. As the fluid moves downstream, the shear layers merge and the flow accelerates to its peak value. The axial velocity then begins to decay rapidly as the flow approaches the stagnation end of the combustor. The centerline velocity drops to 2% of its peak value in approximately 2/3rd of the length of the combustor.

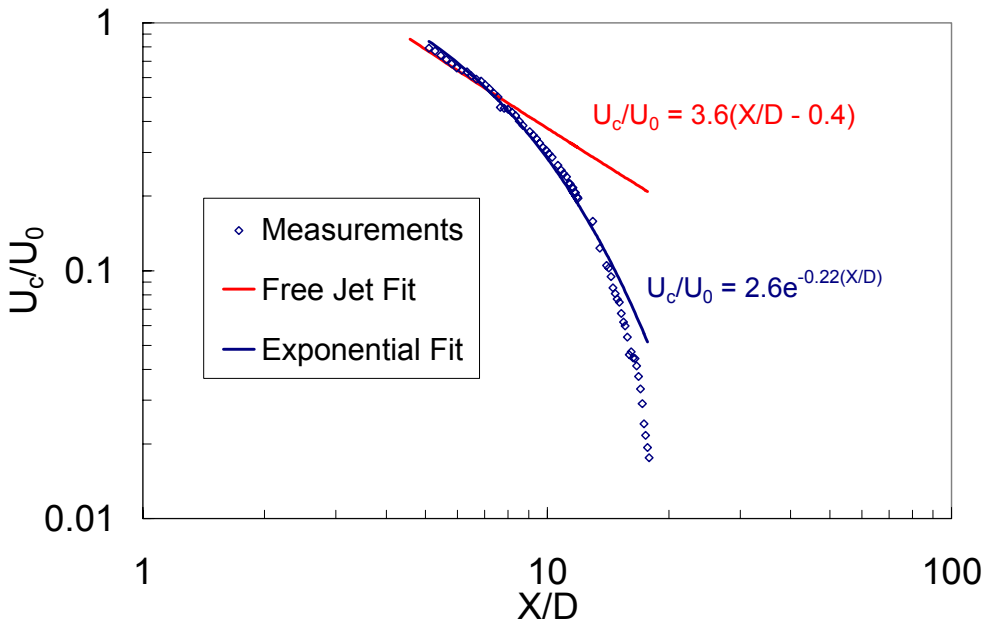

Figure 14. Variation of mean (normalized) centerline velocity with distance from the jet exit along with best- fit curves for the data.

To analyze the decay rate of the jet in the SPRF combustor, the centerline velocity values (U_c) are normalized by the peak jet velocity (U_0) and plotted against the non-dimensional distance from the jet exit (X/D) in Figure 14. It should be noted that the

centerline values are plotted only after the jet attains its peak velocity; we ignore the initial region where the recirculation bubble is present. In addition, the negative velocity regions (beyond the stagnation region) are not considered here.

Figure 14 shows the results plotted on a logarithmic scale. Near the injector ($4<X/D<7$), the measurements follow a nearly linear decay, which is representative of a $(X/D)^{-1}$ scaling. Therefore, the data in this region is fitted to the free jet theoretical decay (Equation 2.2.). From the least-squares best fit result, we find a jet decay constant (B_u) is 3.6 for this region. This value is lower than the result for free jets with similar Reynolds numbers (B_u = 5.9) [13], but this is not surprising considering that the flow here is an annular jet rather than a round jet. Still, the nonreacting jet in the SPRF combustor flowfield (i.e., confined with return flow) initially behaves much like a free jet. As the fluid moves downstream, the decay rate increases rapidly and can be approximated as an exponential decay for $7<X/D<14$ (as indicated by the fit shown in Figure 14). Further downstream, the decay rate increases until the flow finally stagnates due to the presence of the stagnation plate at the end of the combustor ($X/D=24$).

The location of the stagnation region, i.e., the depth of penetration of the jet before it reverses, is seen to be $X/D\sim18.5$. This can be compared to theoretical predictions for a jet in a uniform opposed flow. As seen from Figure 13, the jet enters the combustor with a maximum exit velocity of ~64m/s (U_j). Further, we can approximate the return flow as a uniform opposed flow with an average velocity of ~8m/s (U_{opp}). Substituting these values into Equation 2.4, $\frac{X_p}{D} = C\frac{U_j}{U_{opp}}$, and using the literature value for the constant, 2.4 [16], we find that the jet is expected to penetrate to $X/D\sim19$. Although Equation 2.4 does not strictly apply to highly confined flows (confinement

ratios i.e., D_{outer}/D_{inner} of less than 10, while the current SPRF combustor has a confinement ratio of 5.6), it is seen the nonreacting jet penetration distance in the SPRF combustor is well predicted by the expression.

Thus the behavior of the jet for nonreacting flow in the SPRF combustor may be approximated as a combination of a free jet and a jet in a (confined) opposed flow. From this point on, we will thus characterize the SPRF combustor using three loosely defined regions: a "near" field region close to the reactant injector; a mid-field region where the reactant jet behaves much like a free jet and a far-field region where the effects of confinement and stagnation rapidly reduce the jet velocity.

Next we consider the radial profiles of the mean axial velocities at four different axial locations, as shown in Figure 15. This plot shows the spreading of the jet as the fluid moves downstream of the injector.

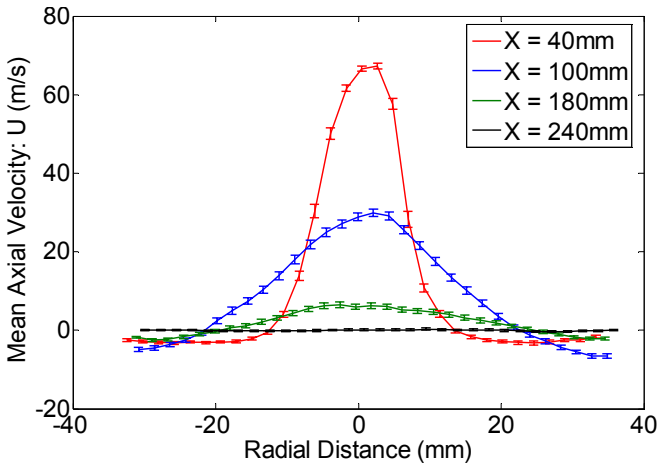

Figure 15. Radial profiles of mean axial velocity (each data point shown with error bars indicating the precision based on 95% confidence levels).

The jet spread as well as the rapid axial decay of the jet is evident from this plot. The velocity drops to less than 50% of the peak value over an axial distance of 50mm. As noted above the stagnation region is approximately 240mm downstream of the injector;

we see near zero velocities across the entire width of the combustor at this distance. The return flow velocities are observed to be of the order of 5-8m/s, with the largest return flow velocities occurring approximately in the mid-section of the combustor. The area available to the return flow is minimal in this region due to expansion of the incoming jet; hence the return flow velocities are higher in this region.

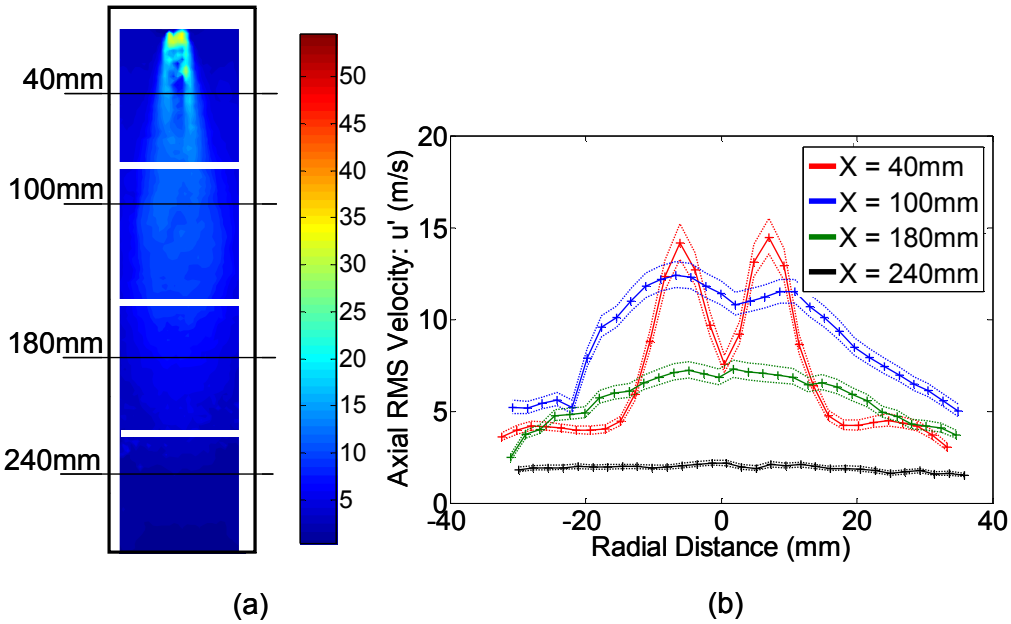

Figure 16. (a) Contours of axial RMS velocity (in m/s) and (b) Radial profiles of axial RMS velocity (shown along with error bands indicating the precision based on 95% confidence levels).

To better visualize the growth of the shear layer, Figure 16(a) shows the contours of the axial RMS velocities over the whole field. The presence of the recirculation near the injector exit is seen as a region of high RMS velocities near the centerline. Outside the recirculation bubble, the centerline RMS velocities decrease. High values of the RMS velocities are also seen in the shear layer between the incoming (annular) jet and the return flow. Further downstream, the shear layers between the forward-moving jet and

the return flow merge causing the centerline RMS values to increase until the flow stagnates close to end plate.

This point is more clearly illustrated in Figure 16(b), which shows the radial profiles of the axial component of the RMS velocity. At 40mm downstream of the injector, there are distinct peaks in the RMS values in the shear layers on either side of the jet. Further downstream (X=100mm), the shear layers have almost completely merged and the RMS velocities are higher across the entire width of the combustor. At just over half the combustor length (X=180mm), the effect of the end plate starts to become significant and the RMS velocities begin to decrease; this trend continues all the way to end of the combustor.

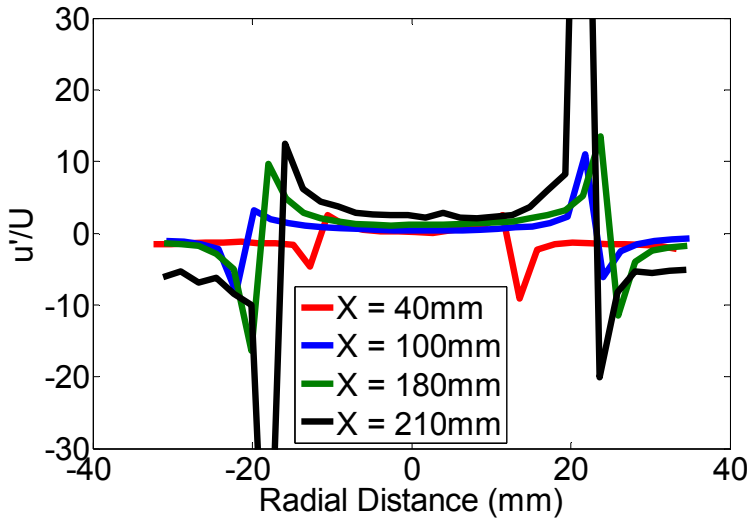

Figure 17. Radial profiles of u'/U.

In order to asses the level of turbulence generated by this type of flow, next we examine the radial profiles of u′/U at different axial locations (Figure 17). It is seen that the shear layers between the forward and return flows is a region of high RMS velocity and low mean velocity, resulting in very high turbulence levels. Along the combustor centerline (radial distance = 0), we see that u′/U grows steadily downstream of the

injector reaching values of one (100% turbulence intensity) at approximately x=175mm. Towards the end plate, the flow stagnates, and mean velocities are nearly zero while the RMS velocities are still high resulting in a high values of u'/U (>1) in the stagnation region (X>225mm) of the combustor. Therefore it is clearly seen that the return flow configuration of the SPRF combustor produces a highly turbulent velocity field with potential for good entrainment and mixing characteristics.

4.1.1 Instantaneous Velocity Field in Nonreacting Flow

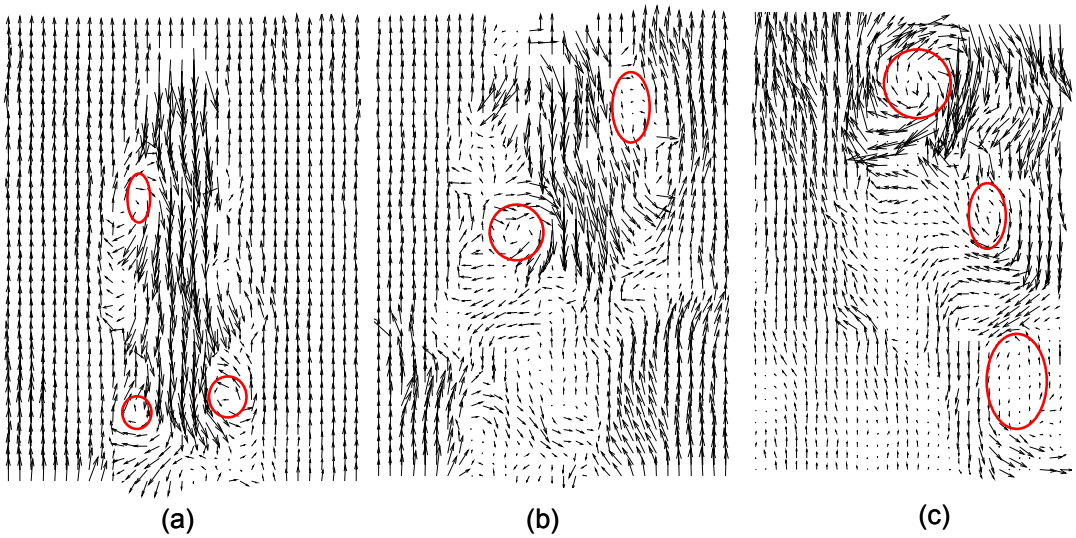

Figure 18. Instantaneous velocity field after subtraction of convective velocity (a) Near-to-mid field (X/D <6), (b) Mid field (6<X/D<12) and (c) Mid-to-far field (12<X/D<18).

In this section, we explore the behavior of the flow on an instantaneous basis to analyze the sizes and growth of the coherent structures that would be responsible for the large scale mixing characteristics in this type of flowfield. Figure 18 shows an instantaneous snapshot of the velocity field in the first three quarters of the combustor (X=0–210mm). The coherent structures or eddies are identified by subtracting a suitable convective velocity from the instantaneous velocity field [48] and are marked here for clarity.

It appears from the figure that the sizes of the coherent structures get larger as we move downstream of the injector exit. In order to estimate the sizes of the large scale structures (L_c), a simple velocity correlation function is calculated based on 300 instantaneous realizations of the velocity field, and the correlation coefficient is integrated within appropriate limits (Equation 3.1). It should be noted that while this method is perhaps not exact, the change in L_c shows a qualitative trend. Also since the spatial resolution of the PIV data is ~2mm, this equation probably fails to capture important scales that are smaller than the data resolution. The results are presented in Table 2. The data is obtained only for the first three-quarters of the combustor length since the flow stagnates and reverses beyond this region making it is difficult to estimate velocity correlations. Here, the radial location is defined as the distance from the axis (centerline) of the combustor in radial direction on either side.

Table 2. Sizes of coherent structures in nonreacting flow.

Measurement Window	**Radial Location (mm)**	**L_c (mm)**
1st Quarter	±7	12
2nd Quarter	±10	18
3rd Quarter	±15	20

The data show that the sizes of the large scale structures increases consistently as the axial distance from the injector increases. The size of the largest eddies is approximately of the order of the width of shear layer at the first two (mid-field) axial locations X/D=3.2 (40mm) and 8 (100mm). In the far-field region (X/D~14, 170mm), the shear layers have merged completely, and the increase in L_c is marginal.

4.2 Premixed Reacting Flow

We now have a better understanding of the basic flow characteristics in the SPRF combustor in the nonreacting case. However, it is well known that the addition of heat release can change a flowfield substantially. This section explores the interaction between the heat release and the velocity field, and the impact of this interaction on the combustion processes. A full matrix of operating conditions at which the velocity measurements are obtained is shown in Table 3.

Table 3. Flow conditions for velocity data.

	Flow Condition	Inlet Fuel-Air Ratio	Inlet Mass Flowrate (g/s)	Inlet Temperature (K)
Case 1	Nonreacting	N/A	8.1	300
Case 2	Premixed	0.6	8.3	500
Case 3	Nonpremixed	0.6	8.3	450
Case 4	Premixed	0.8	8.45	580
Case 5	Nonpremixed	0.8	8.45	630

For the reacting flow case, the air mass flow rate is maintained at ~8.1 g/s, and data is obtained for two separate equivalence ratios: $\phi 1=0.6$ (cases 2 and 3) and $\phi 2=0.8$ (cases 4 and 5). In premixed operation, natural gas and air enter the combustor through the annulus, and as in the nonreacting case, there is no flow through the center tube, which is closed far upstream.

The mean axial velocity contours shown in Figure 16 represent the time-averaged field obtained based on 450 instantaneous images. The nonreacting flowfield is also shown alongside for comparison. Because the burned product gases exiting the

combustor flow over the injector, the temperature of the incoming reactants increases, causing both the inlet and exit flow velocities to nearly double for the reacting flow case.

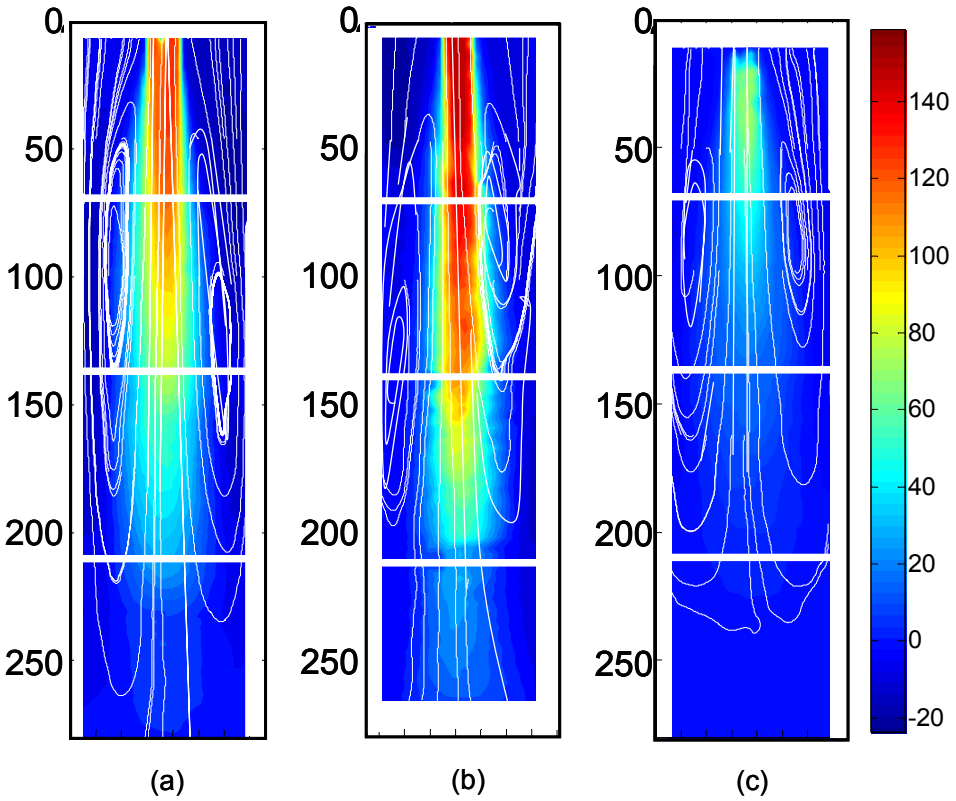

Figure 19. Contours of mean axial velocity (in m/s) for (a) Premixed (ϕ1 = 0.6), (b) Premixed (ϕ2 = 0.8) and (c) Nonreacting flow cases.

The reactant temperature in the injector, after preheating by the exiting products, was nearly 500 K for case 2. Thus the velocity right at the injector exit, based on the measured flow rate and temperature, should be ~133m/s. Though the PIV data does not extend all the way to the injector exit plane, the measured average velocity at an axial location X = 22mm is only slightly slower at 125m/s. Similarly for case 4, the maximum measured velocity of 143m/s is nearly equal to the calculated value (153m/s) based on the inlet preheat temperature. The most striking difference between the reacting flow and the nonreacting case is the location of the stagnation region. For the reacting flow cases, the

flow does not stagnate until it reaches the end plate. This is a result of jet expansion due to heat release. It is also seen that "on average", the recirculation bubble between the inflow and the outgoing products stretches farther downstream compared to the nonreacting case and extends beyond X/D=12 (the midpoint of the combustor length). This recirculation can also lead to entrainment of exiting high temperature products and flame radicals into the incoming reactants, which can significantly enhance chemical reaction rates and aid in flame stabilization.

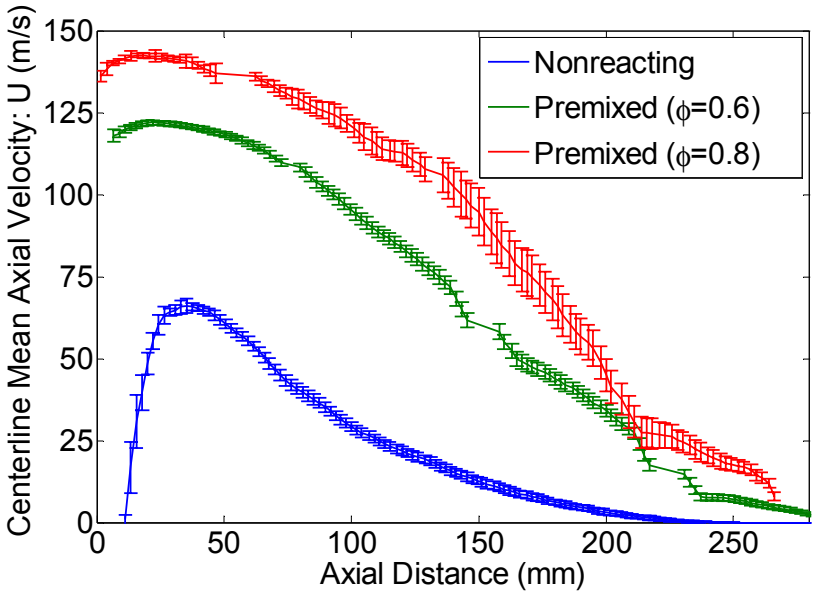

Figure 20. Centerline variation of mean axial velocity along the length of the combustor (each data point shown with error bars indicating the precision based on 95% confidence levels) for cases 1, 2 and 4.

As noted previously, the volumetric expansion of the product gases accelerates the flow pushing the stagnation zone further downstream. This effect is seen more clearly in Figure 20, which shows a plot of the variation in mean axial velocity along the centerline for cases 1, 2 and 4. The drop in velocity in the recirculation region in the near-field close to the injector exit is not captured very well in the reacting flow cases since

the recirculation bubble produced by the inner tube is much smaller for the reacting flow as a result of the higher annular inflow velocities. Also, the timing for the PIV measurements in the near-field region is set to capture the high forward velocities in that location and consequently, the sharp velocity gradient in the near-field region of the injector results in some data loss. It is observed that the velocity drops to nearly 50% of its peak value ~150mm downstream of the injector (X/D = 12) for case 2 whereas it takes ~180mm to attain a comparable velocity drop for case 4 where the equivalence ratio is higher. It is also observed that with the addition of heat release, the centerline decay rate of the jet no longer follows the ~1/X variation that was observed in the nonreacting case.

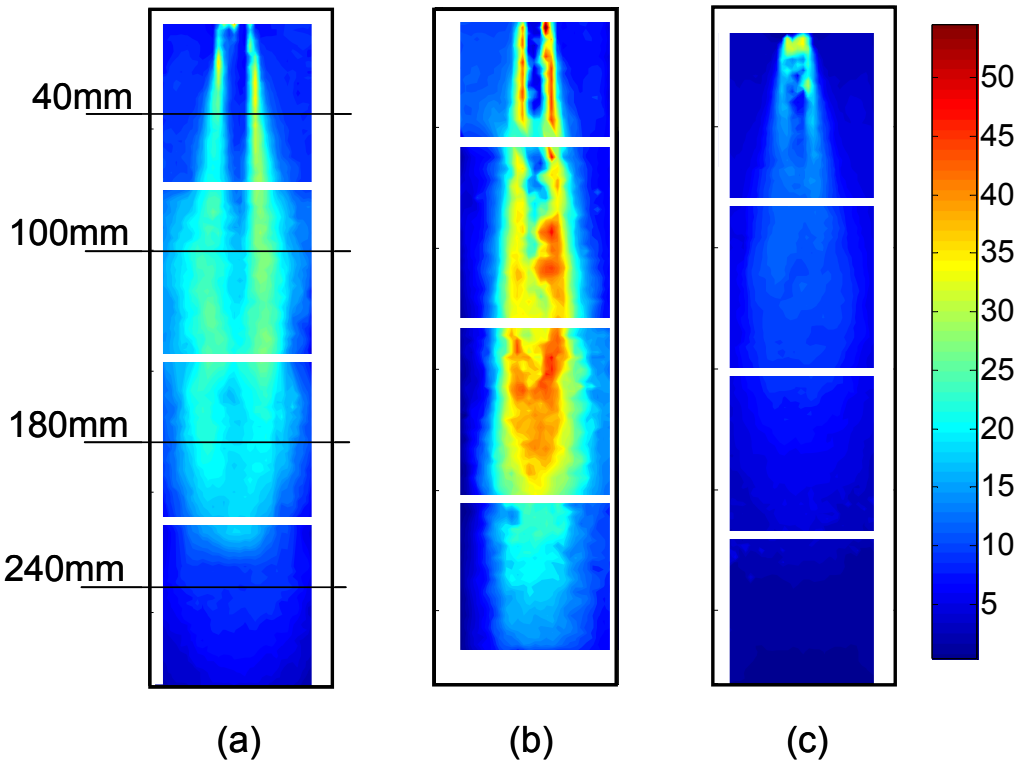

Figure 21. Contours of axial RMS velocity (in m/s) for (a) Premixed (ϕ1 = 0.6), (b) Premixed (ϕ2 = 0.8) and (c) Nonreacting flow cases.

This is a result of the greater heat addition in the ϕ = 0.8 case and correspondingly larger volumetric expansion. Therefore, the centerline jet decay rates for both the reacting flow

cases is initially lower compared to the nonreacting flow as a result of the heat release and then increases substantially as the jet approaches the end plate.

Next we examine the RMS fluctuations in the velocity and elucidate the effect of heat release on turbulence generation in the combustor. The contours of axial RMS velocity for premixed combustion (cases 2 and 4) are shown in Figure 21 together with the nonreacting case. The addition of heat release substantially increases the RMS velocities over the entire combustor volume. Compared to the nonreacting flow, the high RMS region stretches much farther downstream especially for the higher equivalence ratio case where the heat release is greater.

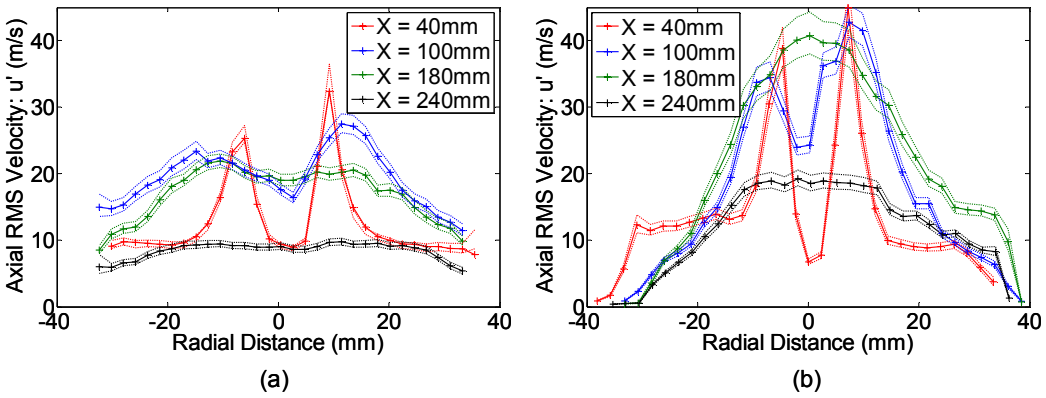

Figure 22. Radial profiles of axial RMS velocity for premixed reacting flow (shown along with error bands indicating the precision based on 95% confidence levels): (a) Case 2 (ϕ = 0.6) and (b) Case 4 (ϕ = 0.8).

It is also seen that the since both the forward and return velocities are nearly doubled in the reacting flow, there is much greater shear between the inflow and the outflow. As a result, the shear layers on either side of the jet merge much farther downstream compared to the nonreacting case. Also, the high shear in the flowfield can cause a flame stabilized in the shear layers to become weak and highly strained. The

implications of this will be discussed further in the next section. Thus, the interaction between the flowfield and the combustion processes starts to become evident here.

To examine the development of the RMS velocities more closely, the radial profiles at four different axial locations are presented in Figure 22. Initially, distinct peaks in the RMS are observed in the shear layer on either side of the jet for both case 2 and case 4. At a distance of ~100mm from the injector exit, the peaks are still visible for both cases, unlike the nonreacting case (Figure 16(b)), indicating that the shear layers have not yet merged for the reacting flow case.

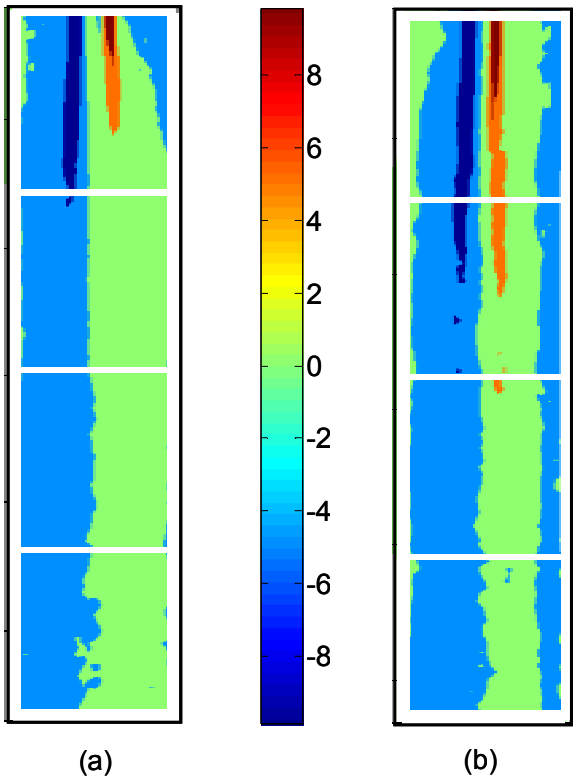

Figure 23. Average vorticity contours (in rad/s) for premixed reacting flow (a) Case 2 and (b) Case 4.

As the temperature of the incoming and outgoing gas increases, the jet expansion is countered by the expansion of the product gases in the return flow, which restricts the

width of the shear layer. Further downstream, the shear layers merge, and we see that the RMS velocities are much higher for case 4 due to the elevated temperatures at that condition. As shown in Figure 23, the vorticity generation in the shear layer indicates that, as expected, the strength of the shear layer is higher in case 4. The region of high vorticity also extends farther downstream for the higher equivalence ratio case (case 4) compared to case 2.

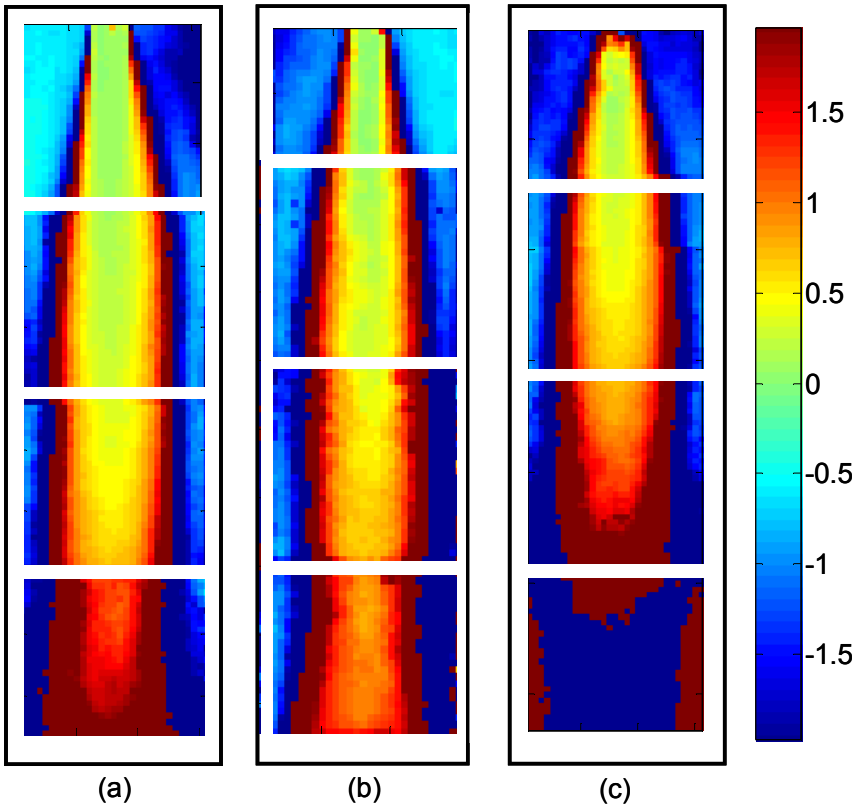

Figure 24. Contours of u'/U for reacting and nonreacting flow (a) Case 2, (b) Case 4 and (c) Case 1.

Considering the variation of the RMS velocities along the centerline, it is observed that unlike the nonreacting case, where the RMS velocities decay after the shear layers merge, there is an increase in the centerline RMS value for reacting flow cases due to the unsteady heat release in that region. In order to understand the effect of heat release

on the turbulence generation in the combustor, it is also useful to inspect the changes in RMS and local mean velocities simultaneously. Accordingly, the variation in axial turbulence intensity is examined by plotting the contours of u′/U (Figure 24).

For all three cases, the turbulence intensities are very high in the shear layers (60-70%). It should be noted that in the region of zero mean velocity, i.e., along the stagnation contour, the u′/U values are no longer meaningful and should be disregarded. Turbulence levels of nearly 50-100% are also observed in the return flow region for all cases. In the nonreacting case (Figure 24 (c)), since the flow stagnates earlier, the local turbulence intensities rise quickly as the fluid moves downstream of the injector exit. For the reacting flow cases, the u′/U values are initially lower compared to the nonreacting case but increase rapidly towards the middle of the combustor as the heat release becomes significant. Approximately 25-100% axial turbulence intensities are observed in these regions for all cases.

Figure 25 shows a plot of u′/U along the combustor centerline. The axial distance is normalized by the average penetration/stagnation length in each case. We see that nonreacting flow has consistently higher turbulence levels compared to the reacting cases. Thus the effect of heat release on this type of flowfield is to suppress turbulence and break up the coherent structures in the flow. This is consistent with the observations in lifted jet flame studies by Mungal *et al*. [46] where they report a reduction in the overall vortical activity and turbulence levels with the addition of heat release. It is also interesting to note that u′/U along the centerline is nearly the same for the reacting cases (2 and 4), since the increase in RMS velocity due to the greater heat addition for case 4 is compensated by a corresponding increase in the local mean velocities.

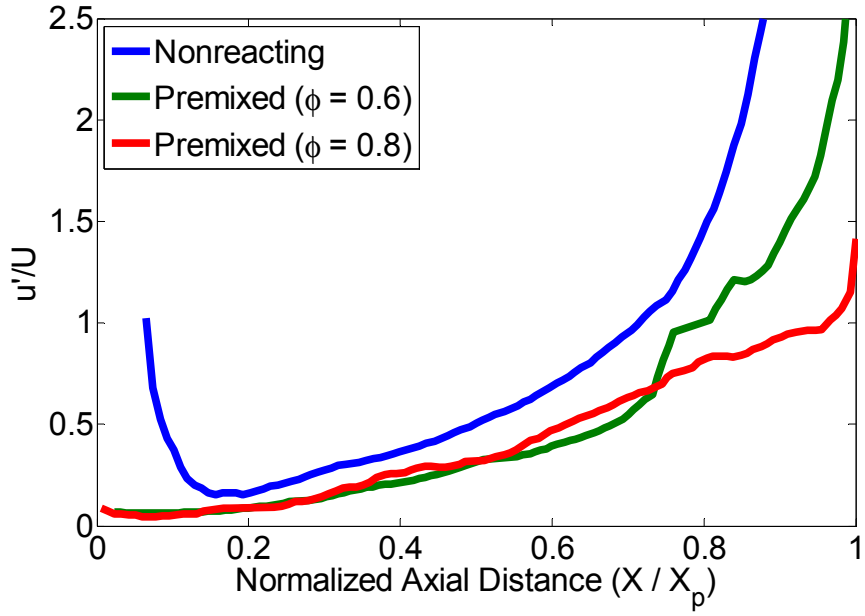

Figure 25. Centerline variation of u′/U for premixed reacting (cases 2 and 4) and nonreacting (case 1) flow plotted against the axial distance normalized by the penetration distance.

4.2.1 Instantaneous Velocity Field in Premixed Reacting Flow

In this section, we examine the effect of heat release on the flowfield by examining the structure/motion of the jet as well as the sizes of the coherent structures in the flow. Together these two aspects control the overall mixing and combustion processes in the SPRF combustor.

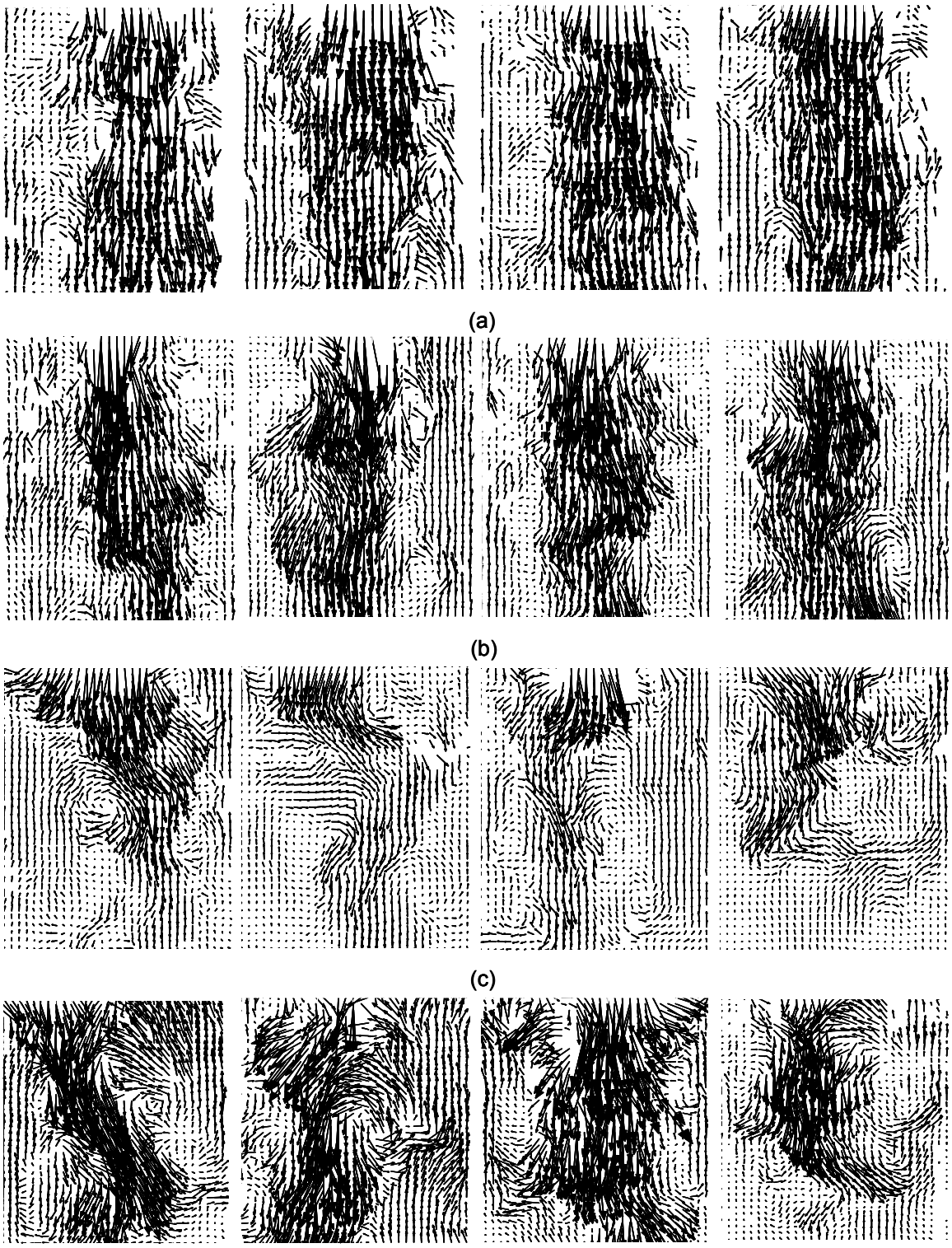

Figure 26. Instantaneous velocity field in 2nd Quarter (a) Nonreacting, (b) Reacting (case 2) flows and in 3rd Quarter (c) Nonreacting, (d) Reacting (case 2) flows.

Figure 26 shows instantaneous images in the mid-field and mid-to-far field regions for the nonreacting (case 1) and leaner premixed (case 2) flows. In the figure, the length of the velocity vectors have been adjusted artificially to enhance the flow features. For the nonreacting case, Figure 26(a) and (c) indicate that the incoming air maintains a centered, jet-like structure with the high forward velocity region remaining mostly in the central part of the combustor. The jet structure nearly disappears after approximately $2/3^{rd}$ of the combustor length as evidenced by the presence of negative velocities towards the end of the 3^{rd} quarter images. Beyond this region, the axial velocities become negligible, and the forward and reverse flow velocities are of comparable magnitude. Although there is some lateral movement of the jet away from the centerline in the 3^{rd} quarter for the nonreacting case, this is not significant when compared to the reacting flow.

For the reacting flow cases, the presence of the flame and the related gas expansion causes greater unsteadiness (RMS velocity) in the flow, which manifests as jet meandering in the PIV data. This is clearly seen in Figure 26(b) and (d); the region of high forward (downward) velocity moves around the combustor. In contrast to the nonreacting flow, the meandering of the central jet is evident earlier (in the 2^{nd} quarter images) in Figure 26(b). Further away from the injector exit, in the 3^{rd} quarter, the jet meandering becomes significant as the majority of the heat release occurs in this region. This behavior is also seen in instantaneous OH-PLIF data, which show that the reactant jet is highly contorted and occasionally breaks up into smaller packets before combustion occurs.

These interpretations are verified with clearer visualizations obtained with the help of 3-dimensional CFD results computed for the same inlet conditions as case 1 and case 2. Instantaneous (3-D) views of the computed axial velocity contours in the nonreacting and reacting flows along the entire length of the combustor are shown in Figure 27. It should be noted that the velocity scaling is doubled for the reacting flow case since the incoming velocity is nearly doubled compared to nonreacting flow [57].

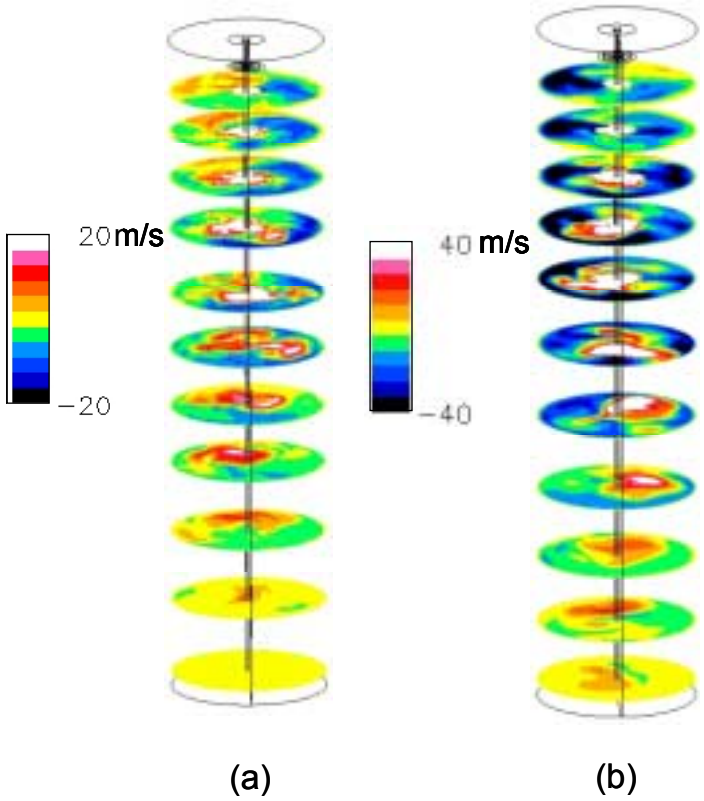

Figure 27. Instantaneous 3-D axial velocity contours (computational data) for (a) Nonreacting (case 1) and (b) Reacting (case 2) flows [57].

In the nonreacting flow (Figure 27(a)), the jet maintains a central core that remains mostly near the axis of the combustor. In the reacting case, however, the flow no longer maintains a simple centered jet-like form. The addition of heat release causes the jet to break up much earlier at ~ X/D=8. Further downstream, around X/D=13, the central

core of the jet has shifted laterally, almost to the edge of the combustor. Thus it is seen that the heat release tends to increase the large scale meandering motion of the jet.

Next, we analyze and compare the sizes of the large scale coherent structures in the shear layers for the two premixed reacting flows (cases 2 and 4) by following the same procedure outlined in section 4.1.1. The data is presented below in Table 4.

Table 4. Sizes of coherent structures in premixed reacting flow.

Inflow Condition	**Case 2**		**Case 4**	
Measurement Window	**Radial Location (mm)**	**Lc (mm)**	**Radial Location (mm)**	**Lc (mm)**
1st Quarter	±5	7	±5	6
2nd Quarter	±8	12	±8	9
3rd Quarter	±13	15	±13	8
4th Quarter	±20	12	±20	7

Over the entire length of the combustor, the sizes of the large scale structures in both reacting flow cases are significantly smaller than those in the nonreacting case presented earlier in Table 2. Therefore it is clear that the heat release induces large scale meandering motion of the jet and reduces the length scales over which the velocity remains correlated i.e., causes a break up of the coherent structures in the flow [46]. Furthermore, the sizes of the structures for the higher equivalence ratio case (case 4) are slightly smaller indicating that as the adiabatic flame temperature increases, the length scales over which the velocities remain correlated become smaller.

4.2.2 Impact of Velocity Field on Combustion Processes in Premixed Operation

This section describes some of the key features of the flame stabilization and mixing processes taking place in the SPRF combustor. We also examine the influence of the velocity field on the combustion characteristics.

Figure 28 shows the averaged CH chemiluminescence images, which indicate the region where heat release occurs for the two premixed cases (cases 2 and 4). The heat release begins fairly close to the injector for both cases, indicating a slightly lifted flame with some heat release in the near field shear layers. The majority of the heat release, however, occurs in the mid-section of the combustor. At a higher equivalence ratio, there is greater heat release in the region closer to the injector exit as a result of the higher preheat temperature as well as the enhanced species reactivity. Based on the velocity data presented earlier, it is seen that most of the heat release occurs in a region where the mean velocities are low and but u′/U is high - of the order of 25-100%.

Thus, the mean chemiluminescence fields indicate that the flame primarily sits in this region of high turbulence intensity, which can produce significant product entrainment and mixing. From a combustion point of view, it is known that this kind of exhaust gas recirculation helps enhance the formation of a radical pool and can therefore improve the stability of the flame thereby facilitating leaner operation of the combustor. The effect of the unsteady flow is more clearly seen in instantaneous PIV and OH images (Figure 29). Single (nonsimultaneous) images of velocity vectors and OH PLIF are shown for the first three quarters of the length of the combustor (X/D<18 or X<225mm). The velocity results show that the incoming jet is highly unsteady; large vortices (indicated by the arrows) are present even relatively close to the injector. They suggest

mixing between the incoming and return flows. Unlike a standard confined jet, where vortices are initiated at the initial shear region and propagate downstream, the SPRF geometry allows vortices carried by the return flow to propagate back towards the injector. If the flame is lifted or the reaction zone is broken, this can allow entrainment of products into the reactant stream. This process is suggested by the images of Figure 29.

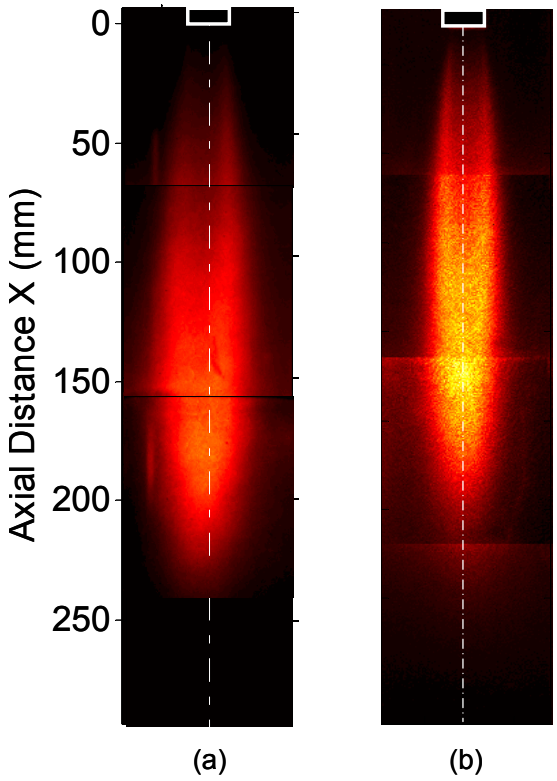

Figure 28. Averaged chemiluminescence images for premixed reacting flow (a)ϕ=0.6 and (b) ϕ= 0.8.

The instantaneous OH PLIF data show what appear to be regions of hot (OH containing) products being entrained into the cold reactants. As noted previously, the size of these vortical structures and the unsteady lateral motion of the reactant gases increase farther away from the injector. This correlates with the increase in u′ downstream. If hot products are entrained and mixed into the reactants by these large scale vortices, then this

will tend to increase reaction rates (and flame speeds), enhancing flame stabilization in the downstream regions. Similar results are expected in case 4 since the velocity fields and the heat release characteristics are comparable.

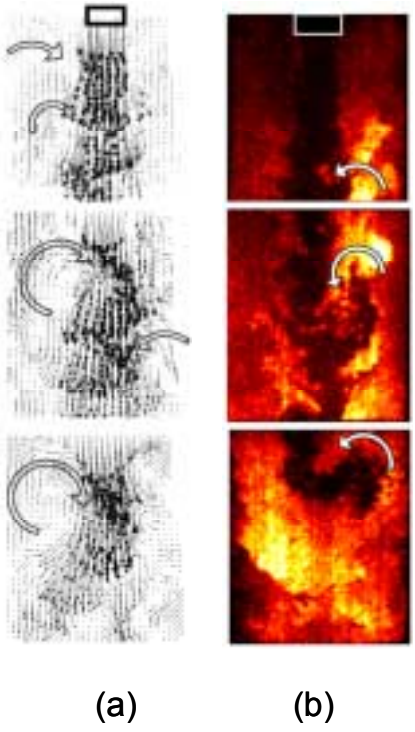

Figure 29. Instantaneous (nonsimultaneous) data showing product entrainment for premixed reacting flow - case 2 (a) Velocity and (b) OH PLIF fields.

To accurately estimate the amount of product entrainment in the system, in a separate study [58], concentration measurements of all major species in the combustor were made using Spontaneous Raman Scattering (SRS) at the same inlet mass flow rate (8.1 g/s) and an equivalence ratio of 0.6 (case 2). Figure 30 shows the axial variation of mean mole fractions (averaged over 500 acquisitions) along the centerline of the combustor. The data extends from close to the injector to half way into the combustor ($0.4< X/D <4$). Product gases (CO_2 and H_2O) are evident along the centerline as early as X/D=5. This supports the previous results which suggest that product entrainment begins

very close to the injector exit plane. Note, the temperature measurements from the Raman data indicate an inlet temperature 500 K, which matches the inlet temperature measured with the thermocouple at the injector.

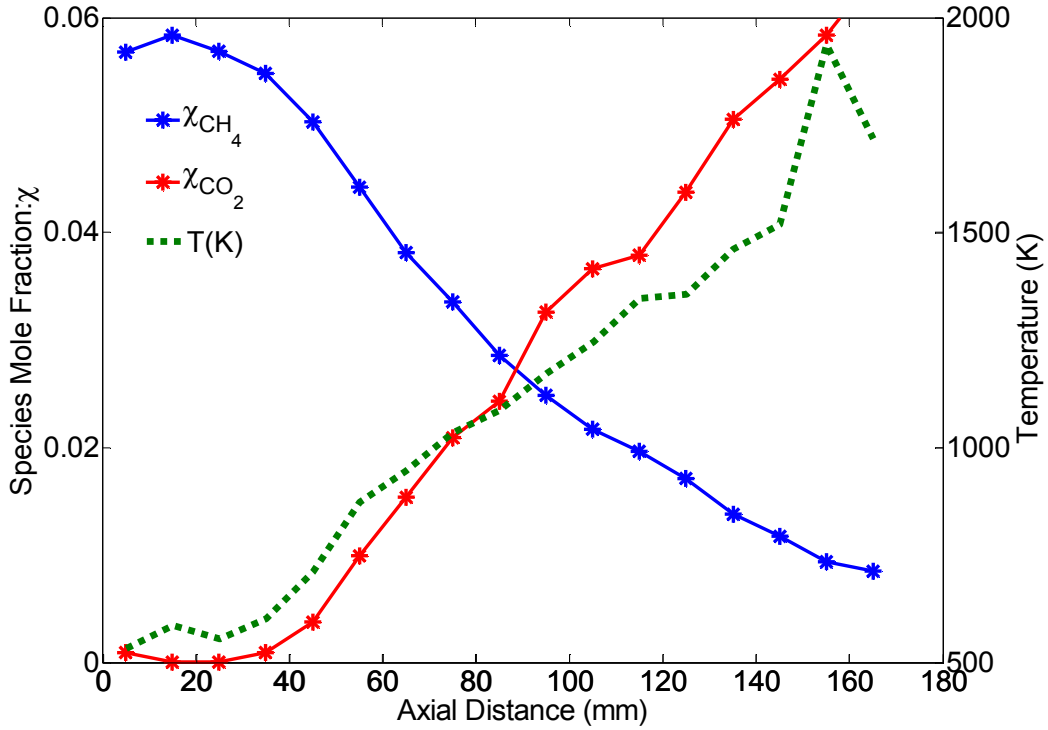

Figure 30. Variation of species mole fractions along the combustor centerline.

Thus, we see that the interaction between the heat release and the velocity field generated by the reverse flow configuration of the SPRF combustor facilitates significant product entrainment and mixing in premixed reacting flow. This in turn aids in stable operation even at very lean equivalence ratios and high loadings enabling the combustor to run with very low emission levels in premixed operation.

4.3 Nonpremixed Reacting Flow

As reported earlier, a distinguishing feature of the SPRF combustor is its ability to produce low emission levels even in the nonpremixed mode of operation. In this mode,

the fuel is injected through the inner tube while the air enters through the annulus. Thus the fuel and air remain completely separated until they enter the combustor. This section describes the flow characteristics of the combustor in this mode of operation. In the current study, the total mass flow rate and the overall equivalence ratio of the fuel and air are maintained at the same values as those used in the premixed experiments.

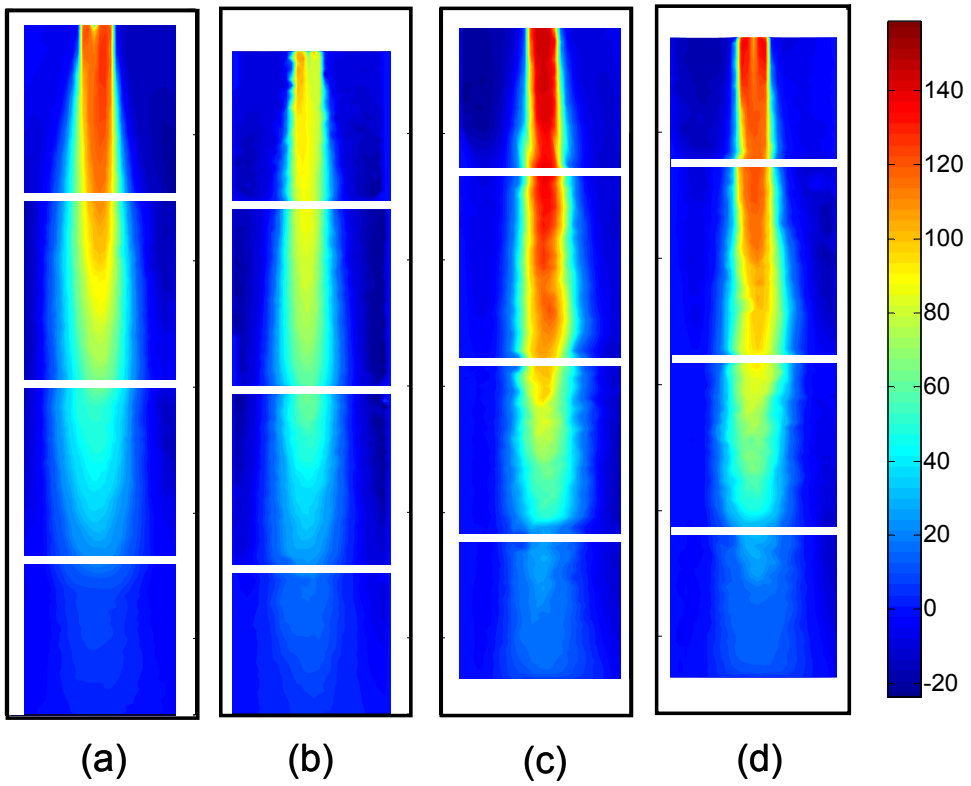

Figure 31. Contours of mean axial velocity(in m/s) for premixed and nonpremixed reacting flow (a) Case 2, (b) Case 3, (c) Case 4 and (d) Case 5.

The average axial velocity contours, based on 400 individual realizations, are shown in Figure 31. Generally, the flowfield is similar to the previous cases. As would be expected for two flows with the same mass flow rates and equivalence ratios, the exiting velocity of the product gases is ~25m/s for case 3 and is slightly higher (~30m/s) for the higher equivalence ratio data; roughly the same values as those in the premixed cases.

The most striking difference is the lower peak jet velocities for nonpremixed combustion compared to premixed operation.

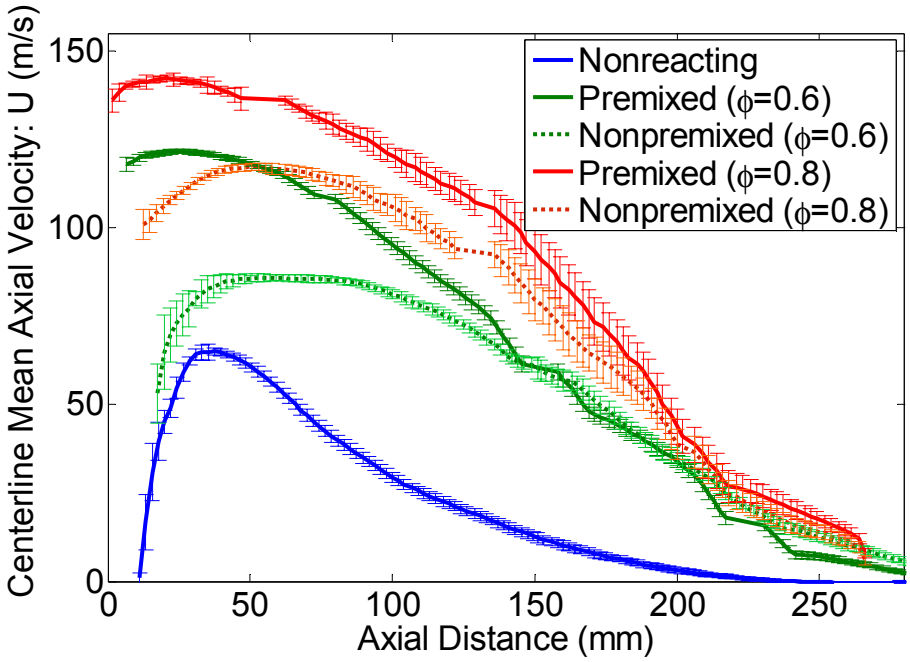

Figure 32. Centerline variation of mean axial velocity for nonreacting and reacting flow cases (each data point shown with error bars indicating the precision based on 95% confidence levels).

This is seen more clearly in the centerline plot of the mean axial velocities (Figure 32). As in the premixed case, preheating of the incoming air increases the inlet velocity; however the inner fuel tube is shielded by the air, so the fuel experiences little preheating. In addition, the effective inlet flow area is increased since part of the mass enters through the central tube in the nonpremixed case. Both these effects help lower the peak velocities for the nonpremixed cases. Another reason for the velocity difference is the difference in flame location for the two modes of operation, which will be discussed more in detail in the next section. Further downstream, the mean axial velocities are nearly equal, with the premixed mode exhibiting slightly higher centerline axial velocity

for the higher equivalence ratio case (case 4). Except in the near field region of the injector, the jet decay rates are also similar for nonpremixed and premixed modes.

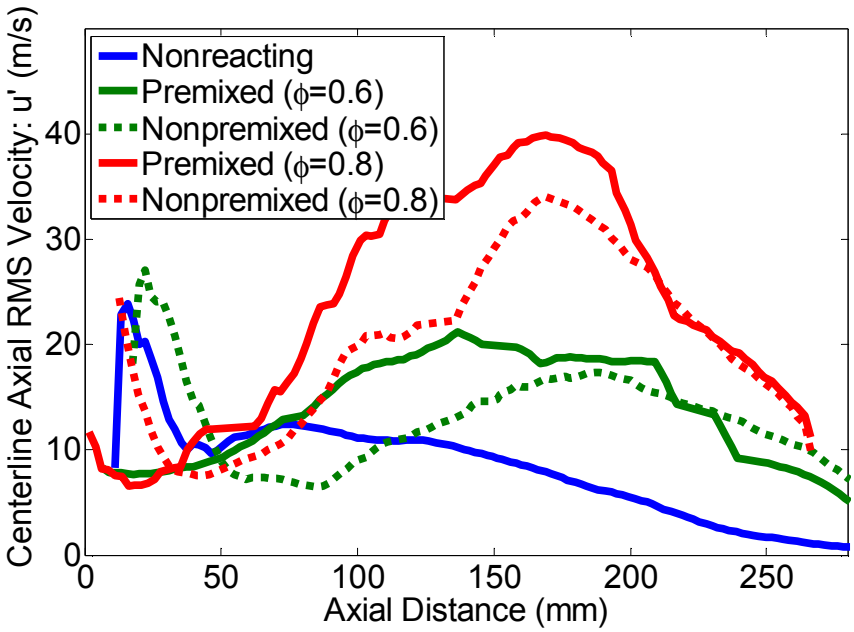

Figure 33. Variation of axial RMS velocity along the centerline for both reacting and nonreacting flow.

The variation in the axial RMS velocities along the centerline is shown in Figure 33. In the near-field of the injector, the axial RMS velocities are higher for the nonpremixed case. The high near-field velocity fluctuations result from the shear between the fuel and air jets, and is expected to enhance fuel-air mixing in this region. Downstream, the fuel-air-product shear layers merge, reducing the RMS velocities. Still farther downstream, the heat release becomes significant, causing a rapid rise in the centerline RMS velocities, which occurs earlier in the premixed cases compared to the nonpremixed mode. This again is a result of the difference in the location where the heat release occurs for the two modes of operation (see Section 4.3.1). It is also noted that the rise in RMS occurs earlier around X=100mm (X/D = 8) for both the higher equivalence

ratio cases (ϕ = 0.8: premixed and nonpremixed) corresponding to the earlier heat release in these cases.

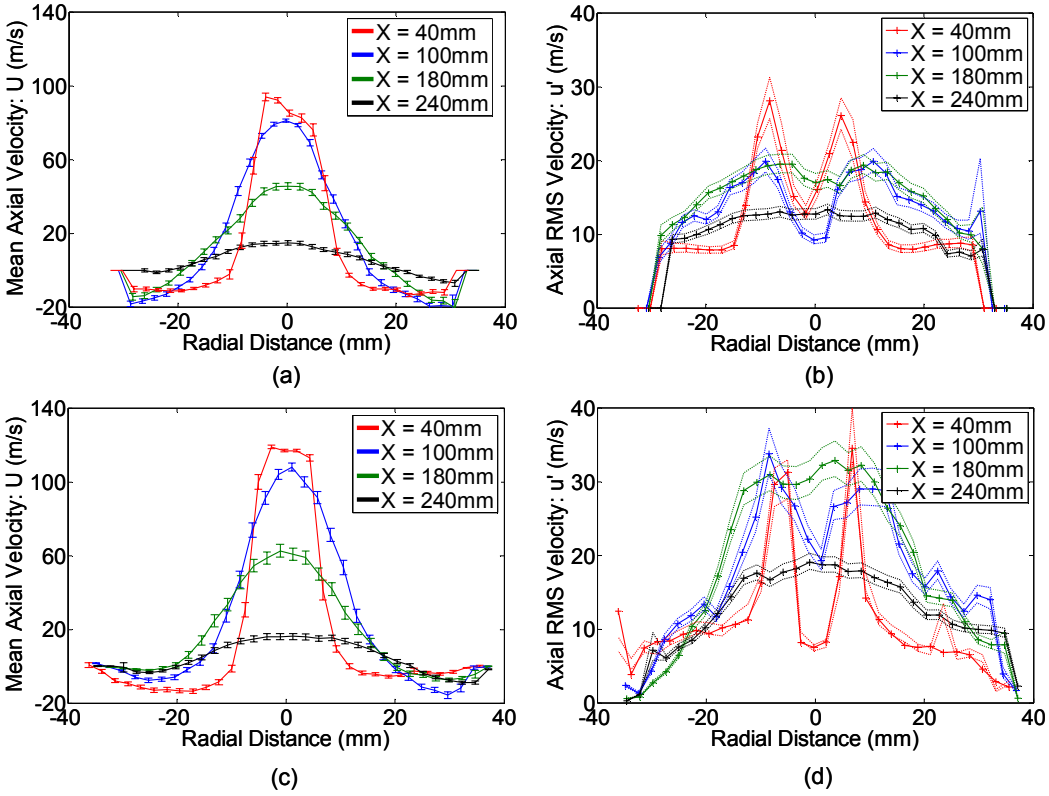

Figure 34. Radial profiles of axial velocities in nonpremixed reacting flow (shown with error bars indicating the precision based on 95% confidence levels): case 3 (a) Mean and (b) RMS velocities and case 5 (c) Mean and (d) RMS velocities.

To see the variation in the flow velocities across the width of the combustor, the radial profiles of the axial mean and RMS velocities at different axial locations along the combustor length are plotted in Figure 34 for nonpremixed operation (cases 3 and 5). As seen from Figure 34(a) and (c), the forward jet velocities for the richer, nonpremixed case (5) are higher than for the leaner case (3) due to the higher inlet preheat temperature obtained at that condition. However, the return flow velocities are slightly lower in case 5 indicating some differences in the jet width and the area available to the return flow for

the two cases. In general, the return flow velocity is mainly dictated by the temperature of the product gases exiting the combustor. As the temperature of the product gases increases and the gases expand, the flow accelerates. This acceleration can manifest as an increase in axial or radial velocities. As seen in Figure 35, the radial velocities are higher for case 5 and hence the axial velocity of the return flow is lower compared to case 3 because of the increased available flow area.

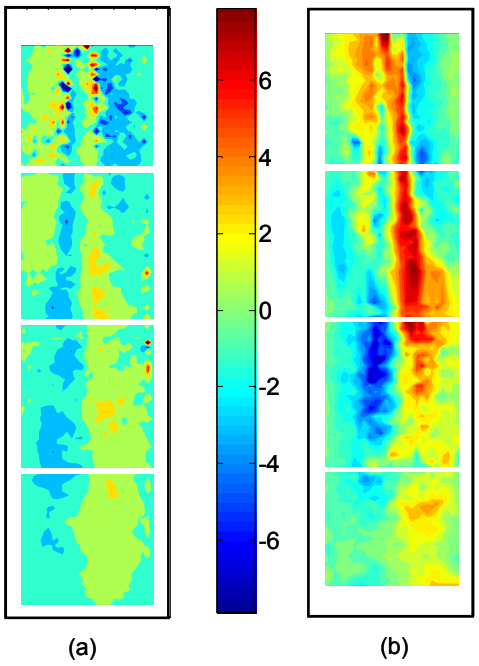

Figure 35. Mean radial velocity contours (in m/s) for nonpremixed flow (a) Case 3 and (b) Case 5.

Figure 34 (b) and (d) show the radial profiles of the axial RMS velocities in nonpremixed operation. As the inlet fuel-air ratio is increased, the higher flame temperatures results in significantly higher RMS fluctuations over the entire length of the combustor. Similar to the premixed mode, the width of the shear layer is reduced as the temperature increases, i.e., case 5 has a thinner shear layer compared to case 3. It is also

observed that the RMS velocities are consistently lower compared to the corresponding premixed cases (Figure 22) except in the near-field region of the injector exit. Since the mean flow velocities are also initially lower in nonpremixed operation, the overall turbulence intensities are nearly the same for both premixed and nonpremixed cases with the nonpremi1xed case exhibiting higher turbulence levels close to the injector exit.

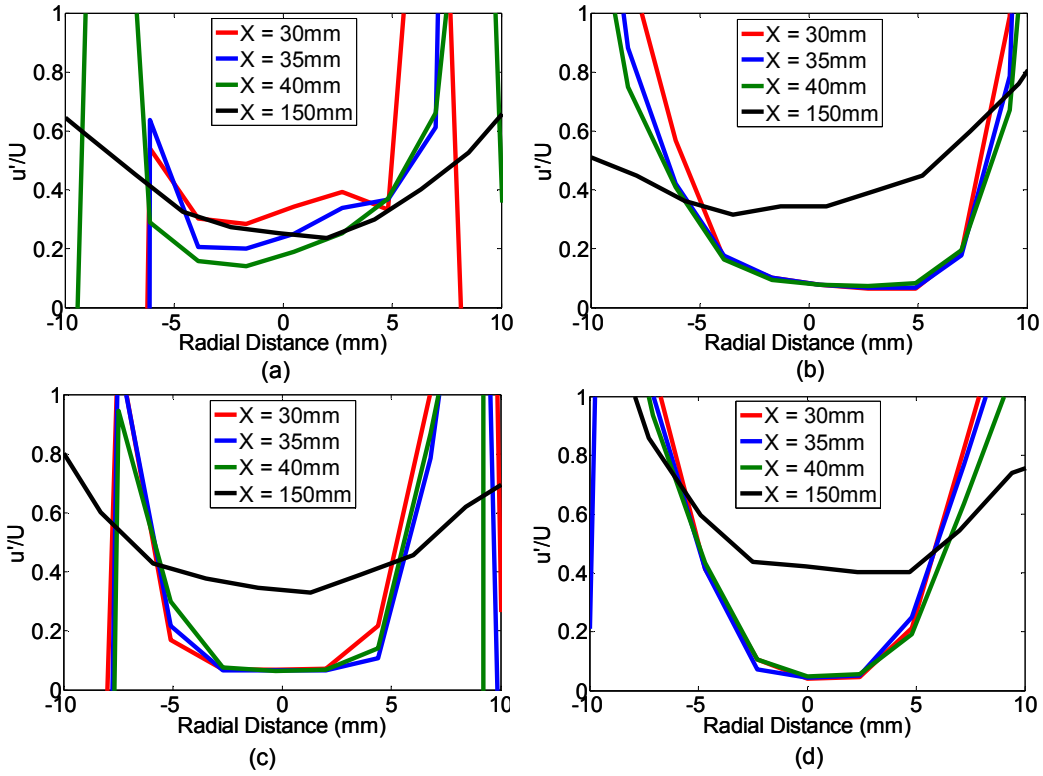

Figure 36. Radial profiles of u′/U nonpremixed and premixed reacting flows (a) Case 3, (b) Case 2, (c) Case 5 and (d) Case 4.

This is examined more closely by plotting the radial profiles of u′/U at different axial locations. Figure 36 shows that close to the injector exit, the nonpremixed cases have higher u′/U values, i.e., higher turbulence intensities, which is suggestive of stronger mixing in this region compared to the premixed flows. Particularly in case 3, we see that the turbulence levels in the near-field region (X<40mm) are at least 20-40%.

Therefore the initial regions of the nonpremixed flow are likely to have enhanced mixing rates. This difference in the u′/U values for the nonpremixed and premixed flows becomes less pronounced as the inlet fuel-air ratio is increased (cases 4 and 5). Farther from the injector exit as we approach the region where heat release occurs, the turbulence levels become comparable to the premixed values.

Lastly, we compare the centerline variation of u′/U along the length of the combustor for both premixed and nonpremixed flows (Figure 37). As noted above, we see that in the near-field of the injector, the nonpremixed cases have higher centerline u′/U values, indicating a strong air-fuel shear layer in the region that could result in some fuel-air premixing before combustion occurs. This supports the NOx data presented in Chapter 1, which show the similarities in NOx emissions between the premixed and nonpremixed modes. Further downstream, the values are nearly equal for all the reacting cases indicating that although the mean and RMS velocities are higher for the richer condition (cases 4 and 5), the overall turbulence intensity remains almost unchanged.

Hence it can be inferred that the velocity fields in both premixed and nonpremixed modes of operation are very similar except in the near field region of the jets. However, it is seen that this difference does not persist more than a few injector diameters. Further downstream, the axial velocities are approximately equal, and the premixed mode exhibits slightly higher turbulence intensities. Both premixed and nonpremixed modes of operation confirm the presence of a low U and high u′ region in the second half of the combustor that has been shown earlier to help stabilize the flame for premixed operation. Therefore, the comparable performance of the combustor, in

terms of emissions levels, in both modes of operation may be attributed to the similarities in flow fields and possibly high levels of mixing.

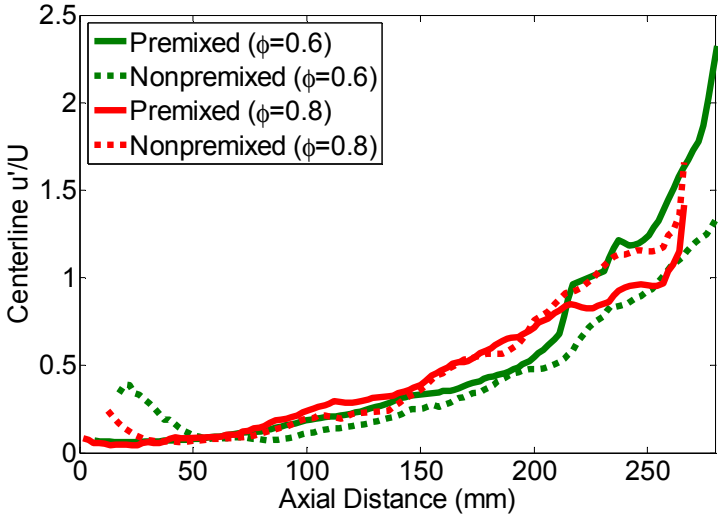

Figure 37. Centerline variation of u′/U in premixed and nonpremixed reacting flow.

4.3.1 Flowfield and Combustion Processes in Nonpremixed Operation

This section investigates the interaction between the flowfield and the heat release processes in nonpremixed operation of the SPRF combustor, as well as the differences/similarities between the premixed and nonpremixed modes.

The location where the flame is stabilized in the nonpremixed mode is seen from the average (200 images) chemiluminescence field shown in Figure 38. Most of the heat release occurs for 100<X<220 mm (8<X/D<18). It is also seen that as the overall fuel-air ratio is raised (case 5), the preheat temperature at the injector increases, and the flame moves upstream closer to the injector. Unlike the premixed combustor (Figure 28), there is negligible heat release close to the injector in the nonpremixed cases. The flame is completely lifted and stabilized only in the region of lower velocity and high

unsteadiness. The reduced heat release in the first half of the combustor also explains the lower initial velocities found for nonpremixed operation (Figure 31); the lower heat release causes less expansion and a reduced initial acceleration of the flow.

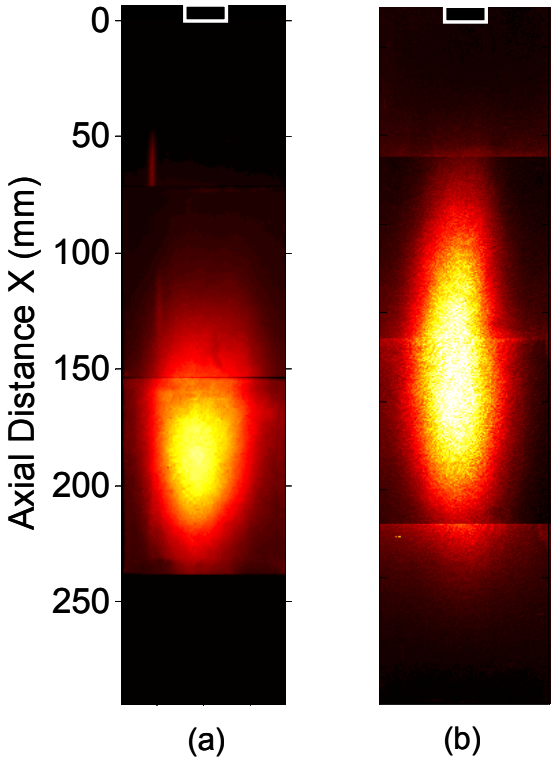

Figure 38. Averaged CH chemiluminescence images for nonpremixed operation (a) Case 3 and (b) Case 5.

The centerline variation of the turbulence intensities and normalized chemiluminescence intensities in the region where heat release occurs are plotted in Figure 39. In case 3, it is observed that the chemiluminescence intensities are nearly zero in the near-field of the injector, corresponding to the absence of heat release in this region. Gradually the signal increases and peaks around X=150-230mm (12<X/D<18), where the majority of the heat release occurs. The centerline u′/U in this region is

approximately 20-40%. As the inlet fuel-air ratio is increased, we see that although the chemiluminescence intensities rise closer to the injector, the turbulence levels (u′/U) are still of the order of ~15-50% in the region where the flame is stabilized.

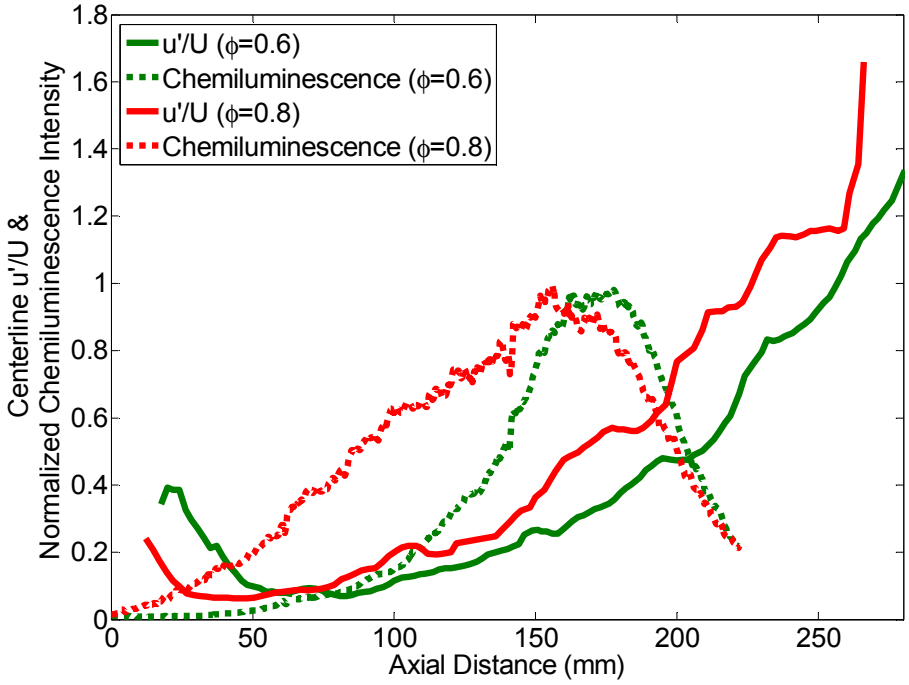

Figure 39. Centerline variation of u'/U and normalized chemiluminescence intensity in nonpremixed operation.

The large flame standoff distance for case 3 (inlet ϕ = 0.6) suggests that there is time for fuel and air to mix, and also to entrain product gases before reaching the flame zone. In contrast for case 5, the flame lift-off height is lower; this is attributed to the lower chemical time at this condition. However, based on the velocity data, it is expected that the mixing times remain nearly unchanged for the two cases. Hence, at a higher inlet fuel-air ratio (inlet ϕ = 0.6) there may not be sufficient time for significant internal fuel-air premixing before combustion occurs. Therefore the greater disparity in NOx

emissions between premixed and nonpremixed operation at $\phi = 0.8$ may be attributed to this difference.

To examine this idea of internal fuel-air premixing for case 3 more closely, the rate of fuel mixing was studied by imaging light scattered from oil droplets seeded into the fuel as described in chapter 3. The boiling point of olive oil is 570K; hence the droplet size and therefore the scattered intensity is reduced either by: 1) dilution due to mixing with air or products, or 2) evaporation caused by partial mixing with hot products or proximity to the flame zone. Mixing with air that has not mixed with products will not lead to significant droplet evaporation, since the inlet air temperature is just below 450 K. For an average droplet size of 7μm and for fuel velocities above 50 m/s, it is estimated that a rapid drop in scattering intensity due to evaporation would occur for temperatures greater than ~900 K. Hence, it may be inferred that the regions where droplets are observed represent locations where the local temperature does not exceed ~900-1100 K.

Figure 40(a) and (b) show an instantaneous image of the CH chemiluminescence and droplet scattering acquired simultaneously. Majority of the heat release occurs only after the seeding droplets have completely evaporated. This seen more clearly in Figure 40(c) which shows the variation of the normalized average, centerline droplet intensity with axial distance from the injector exit as well as the average chemiluminescence intensity along the centerline. The decrease in droplet scattering intensity is less than 20% in the near-field (X/D<3). The corresponding chemiluminescence intensities in this region are essentially zero. These observations suggest some fuel-air mixing occurs here, but with little entrainment of products into the fuel stream. In other words, the fuel is initially shielded from the hot products by the annular air. Further downstream, the

scattered intensities drop nearly linearly, until x~125mm (X/D=10), at which point the droplet scattering is reduced to the local background level. The nearly linear decrease in droplet scattering before this points suggests significant dilution of the fuel with air, and possibly products, is occurring, but that the fraction of products is sufficiently low that the temperatures do not exceed the 900-1100K level much before X/D = 10. The rapid increase in average chemiluminescence (or heat release) for the region beyond this indicates temperatures there are high enough to evaporate the oil droplets.

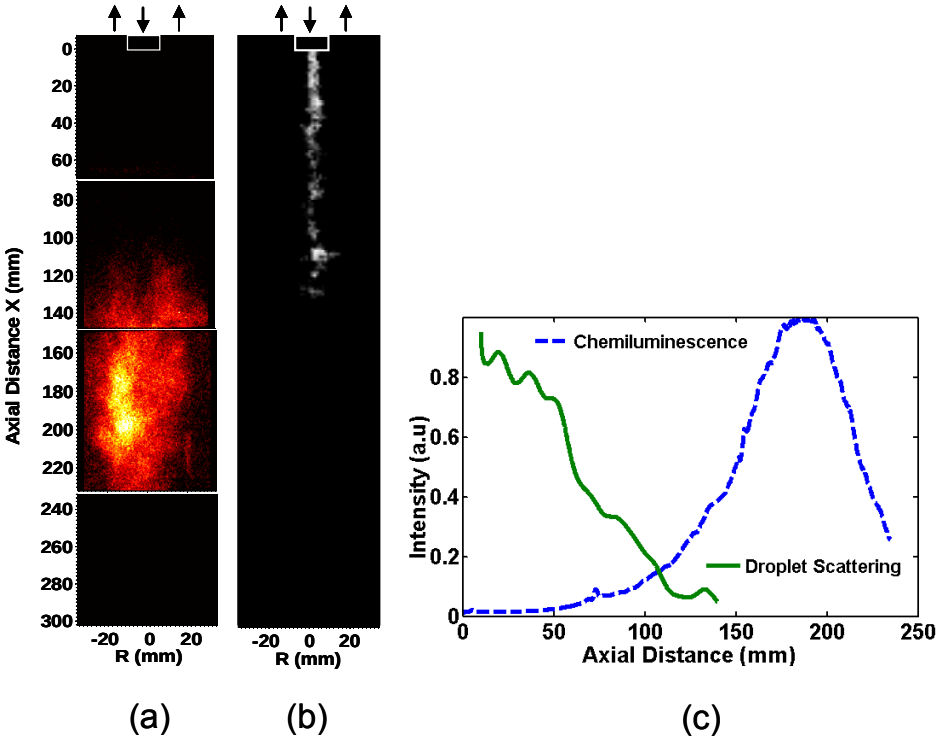

Figure 40. (a) Instantaneous chemiluminescence data, (b) Simultaneous droplet scattering image and (c) Centerline variation of normalized droplet intensity and average chemiluminescence signal.

These results suggest that fuel-air mixing occurs in the initial zone of the combustor, while air and product mixing occurs in the shear layer between the forward flowing reactants and the returning products (Figure 41). Close to the injector exit, the

fuel remains shielded from the hot products preventing the occurrence of a diffusion type flame burning at stoichiometric equivalence ratios thus enabling the SPRF combustor to operate with low NOx emissions even in the nonpremixed mode.

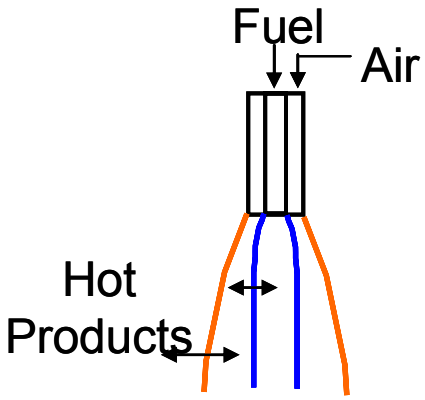

Figure 41. Schematic sketch of the fuel-air-product shear layers in nonpremixed operation of the SPRF combustor.

To visualize the reactant-product streams and the combustion zone in nonpremixed operation, next we examine some OH-PLIF data. A comparison of the instantaneous OH fields for premixed and nonpremixed modes of operation at a global ϕ=0.6 is shown in Figure 42. Starting at X~110mm (X/D~9), the reactant streams (the central dark regions in the images) show similar structures and penetration for both premixed and nonpremixed cases. However, just beyond the point of maximum penetration, where the PLIF images show somewhat uniform signals over a broad region, the nonpremixed case results in higher fluorescence intensities. Comparing 100 instantaneous images for each case, the nonpremixed intensities are found to be approximately 40% higher. Based on the assumption that these broad uniform regions are close to OH equilibrium, the variation of equilibrium OH concentration and the

corresponding (simulated) PLIF signal, which also takes into account variations in quenching and population fraction, were calculated as a function of equivalence ratio.

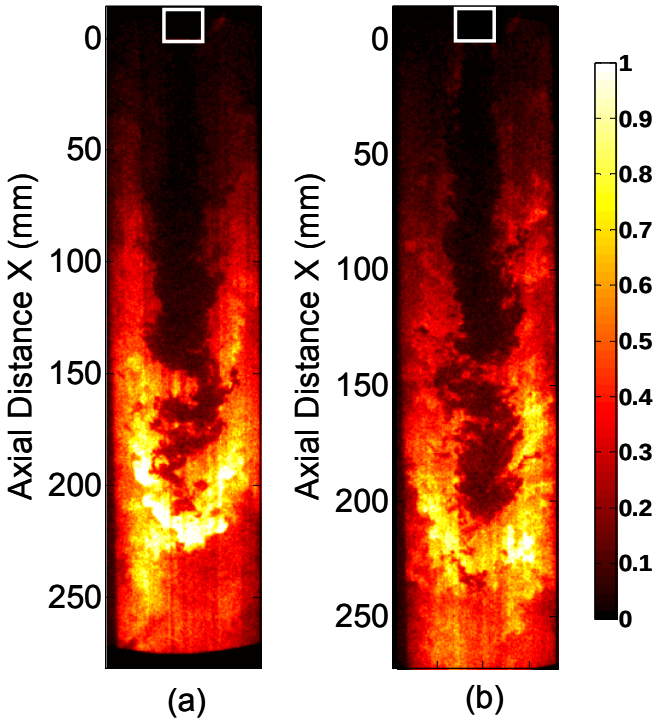

Figure 42. Instantaneous OH PLIF data at ϕ = 0.6 for (a) Nonpremixed (case 3) and (b) Premixed (case 2) reacting flows.

From the simulation results shown in Figure 43, it is seen that a 40% increase in PLIF signal would indicate that the flame in the nonpremixed mode is burning only slightly richer (ϕ~0.65) than in the premixed case (ϕ~0.6). This marginal increase in equivalence ratio of the flame above the overall value indicates effective mixing of nearly all the fuel and air before they reach the flame zone. This observation has also been verified independently based on species concentration measurements obtained at the same inlet conditions as case 3 [58]. Therefore the flowfield produced by the coaxial

injector in the SPRF combustor results in similar NOx emissions for premixed and nonpremixed modes at the leaner inlet fuel-air ratios.

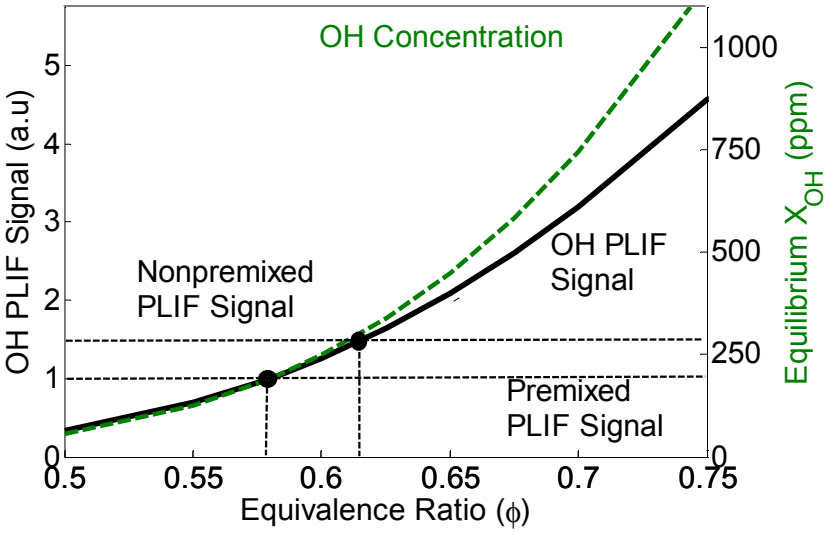

Figure 43. Variation of equilibrium OH concentration and PLIF signal with equivalence ratio.

Another important effect of the combustion process on the flow is seen when we examine the jet expansion in the SPRF combustor more closely. The parameter that is used to classify the jet spread is the jet width defined here as the distance from the centerline of the radial location at which the axial velocity drops to zero. Figure 44 shows the variation of the jet width along the length of the combustor for the different flow conditions.

For all the cases, the overall jet spread is limited both due to the effects of confinement as well as the presence of the return flow. Initially the nonreacting jet has a lower jet width compared to the reacting cases where the higher inlet temperature causes the jet to expand more rapidly. Away from the injector exit, it is seen that the initial jet widths are similar for the nonreacting and premixed combustion cases. Further downstream, the nonreacting jet spreads rapidly in the radial direction since the return

flow is composed of cold gas (same density as entering flow). At approximately X=220mm (X/D~18), the nonreacting jet width drops rapidly to zero as the flow begins to stagnate ahead of the end plate. All the reacting flow cases exhibit a lower jet-width is compared to the nonreacting case as result of the expansion (lower density) of burned product gases exiting the combustor.

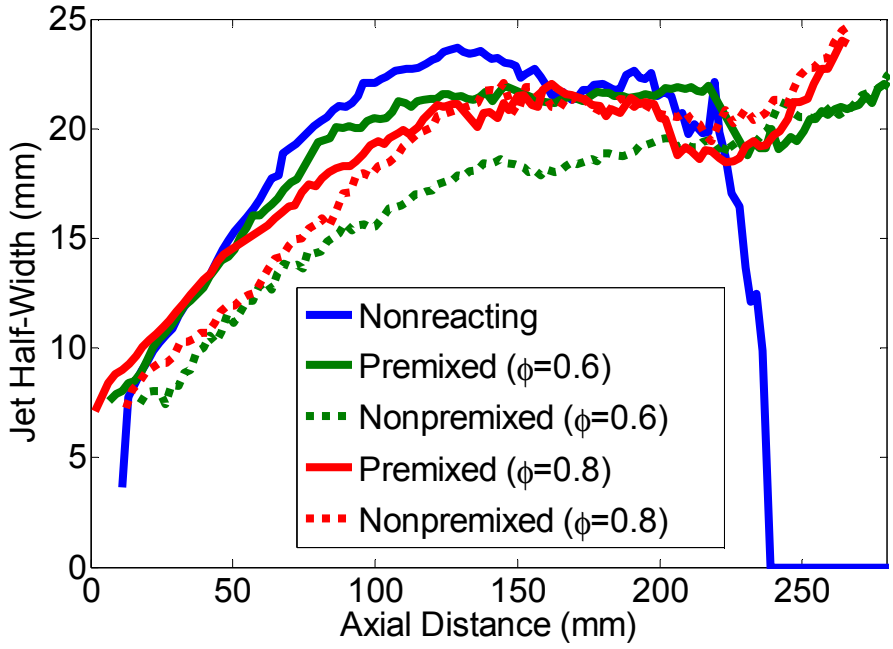

Figure 44. Axial variation of jet half-width for both reacting and nonreacting flow.

It is also seen that initially the jet spread is more in the premixed cases compared to the nonpremixed mode of operation. Since the heat release begins closer to the injector exit when the combustor operates in the premixed mode, the jet expands more rapidly in the radial direction and therefore the jet width is comparatively higher for cases 2 and 4 in the first half of the combustor. In this region, the premixed reacting flow exhibits slightly higher return flow velocities due to the decreased area available to the return flow compared to the nonpremixed case. Further downstream, as the heat release becomes

significant in the nonpremixed flow, the jet width becomes comparable to the premixed cases. This happens earlier for the ϕ=0.8 case where the flame moves closer to the injector as result of the higher preheat temperatures and increased species reactivity.

4.3.2 Instantaneous Velocity Field in Nonpremixed Reacting Flow

In this last section, we compare the instantaneous features of the flowfield for nonpremixed operation of the SPRF combustor. Similar to the premixed and nonreacting flow cases, the sizes of the coherent large-scale structures are calculated based on the velocity correlations and the data are shown in Table 5.

Comparing the values to the data shown in Table 3, it is clearly seen once again that the size of structures is reduced for the reacting flow case compared to the nonreacting case. The sizes of the large scale structures in the nonpremixed cases are also consistently lower compared to the corresponding premixed case for the ϕ=0.6 (case 2) condition (Table 4).

Table 5. Sizes of coherent structures in nonpremixed reacting flow.

Inflow Condition	**Case 3**		**Case 5**	
Measurement Window	**Radial Location (mm)**	**Lc (mm)**	**Radial Location (mm)**	**Lc (mm)**
1st Quarter	±5	4	±5	6
2nd Quarter	±8	8	±8	8
3rd Quater	±13	9	±13	9
4th Quarter	±20	13	±20	10

In case 3, as shown earlier, the nonpremixed case burns at a slightly higher equivalence ratio (ϕ~0.65 compared to ϕ=0.6) resulting in higher product temperatures.

This together with the augmented radial meandering for the nonpremixed case reduces the length over which the velocities remain correlated resulting in smaller coherent structures. In contrast, as the inlet fuel-air ratio is increased to $\phi = 0.8$, the premixed and nonpremixed flows behave nearly the same way as the chemical times are reduced and characteristic mixing time becomes insufficient. Thus as seen from the data above, the sizes of the coherent large scale structures are comparable for case 5 and case 4 (shown in Table 4).

Thus it is seen that the velocity field produced by the unique geometry of the SPRF combustor enables stable operation at very lean equivalence ratios and high loadings while producing ultra-low emissions in both premixed and nonpremixed operation. The presence of a low velocity stagnation zone together with the recirculation of nearly adiabatic product gases laden with radicals provides a robust flame stabilization mechanism in the SPRF combustor. It is also seen that at lean inlet fuel-air ratios, the flowfield causes high levels of internal premixing allowing the combustor to burn at nearly global equivalence ratio resulting in very low NOx emissions even in nonpremixed operation.

CHAPTER 5

LIQUID-FUELED OPERATION OF SPRF COMBUSTOR

As noted previously, one of the key features of the SPRF combustor is its ability to run stably over a range of equivalence ratios and loadings while producing ultra low NOx emissions with both gaseous and liquid fuels. This chapter explores the operation of the SPRF combustor when it is fueled with liquid Jet-A without external prevaporization of the fuel before it enters the combustor. The addition of liquid fuel induces additional time scales to the combustion process, viz., atomization and evaporation times. Aside from this, the liquid- and gas-fueled modes of operation are expected to be similar. Since the stoichiometric fuel-air ratio is very small for Jet-A, the quantity of liquid entering the combustor is very small and is not expected to change the overall characteristics of the velocity field (described in Chapter 4) significantly. As described in the experimental set-up (Section 3.1.2), the fuel injector is modified only slightly for liquid operation and two separate injector placements are chosen for this study. We begin by investigating the distribution of liquid in the combustor for the two injector placements at different inlet conditions. Then, we examine the effect of fuel dispersion on the combustion processes as well as the NOx emissions in liquid-fueled operation of the combustor. These observations are compared against gas-fueled operation of the SPRF combustor throughout this chapter.

5.1 NOx Emission in Liquid-Fueled Operation

Figure 45 shows a comparison of the NOx emissions obtained with (liquid) Jet-A and natural gas. Several similarities are seen between the two modes of operation. In gas-fueled operation, it is observed that premixed and nonpremixed operation produce nearly the same NOx levels at low temperatures (below ~1900K). Beyond this, the nonpremixed mode produces higher NOx emissions. In liquid-fueled operation, the performance is affected by both the temperature as well as the injector placement. The emissions are found to be lower when the liquid injector is retracted into the air annulus compared to when it is flush with the air exit. At low adiabatic flame temperatures, the effect is small, but it increases with temperature.

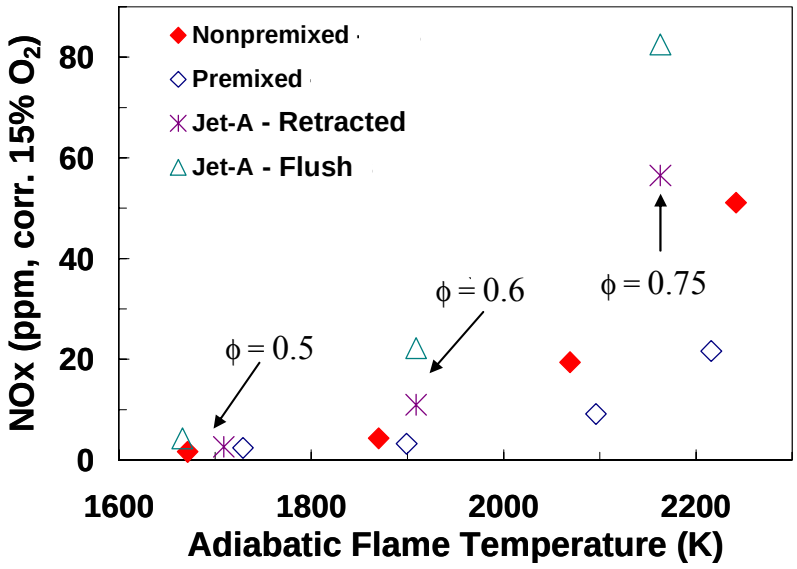

Figure 45. Variation of NOx with adiabatic flame temperature.

5.2 Fuel Dispersion and Liquid Distribution in the Combustor

Instantaneous images of laser scattering from the liquid fuel, shown in Figure 46, demonstrate the effects of injector placement on fuel dispersion. The distribution of liquid changes significantly depending on the location at which the fuel is injected. When the liquid injector exit is level with the exit of the air annulus, the fuel and air remain completely separated until they enter the combustor. As seen in Figure 46(a) for this configuration, the fuel enters the combustor as a liquid jet that gradually breaks up to form droplets. Initially the liquid remains in the center shielded from the returning products by the surrounding air, similar to the nonpremixed gas-fueled operation. Further downstream, the liquid jet spreads and starts to break up as ligaments begin to appear and eventually, the jet disintegrates completely to form droplets. Downstream of the injector, significant product entrainment likely occurs, with the exposure to hot gases allowing the fuel droplets to evaporate.

When the fuel injector is retracted into the air tube, the liquid fuel enters the combustor in the form of droplets that are spread across the entire width of the injector (Figure 46(b)). Since some of the fuel is now located at the edge of the inlet air jet, it is no longer shielded from the high temperature products, unlike the flush configuration. Thus the liquid fuel close to the product-reactant shear layer can evaporate rapidly, and mix with air and products to form a combustible mixture. The fuel distribution in this case resembles the premixed gas-fueled case, where a strong shear layer is observed close to the injector exit resulting in significant product entrainment.

In both injector configurations, droplet scattering images show the presence of a significant amount of liquid at the combustor inlet, suggesting little evaporation has

occurred inside the injector. To investing the amount of evaporation that might occur inside, the SMD of the droplets exiting the injector is estimated to be 120μm based on empirical models [5]. For the measured air injection temperature of 420K, which corresponds to the highest global equivalence ratio case (ϕ_{global}=0.75), the droplet lifetime based on a simple D^2 law is ~400ms with a transient heating time of ~6 ms [42]. As the residence time inside the injector for the retracted case is only ~2ms, it is expected that the quantity of fuel that is prevaporized is not significant for the retracted injector. For the flush injector, although the inlet air temperature is slightly higher, the droplet sizes are expected to be larger since the liquid jet is only atomized after it enters the combustor.

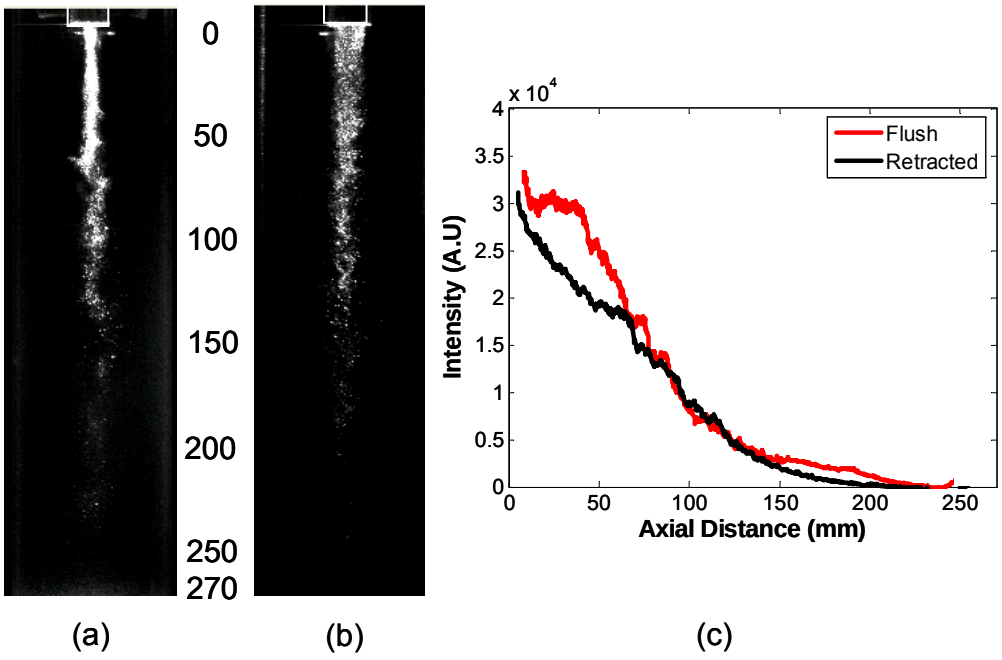

Figure 46. Instantaneous droplet scattering images at ϕ_{global} =0.5 and m_{air} = 8.1g/s for: (a) Flush and (b) Retracted injector locations, (c) Axial variation of time-averaged, transverse-integrated intensities.

The extent of liquid penetration for the two injector placements can be estimated by plotting the variation in the average droplet intensities (radially integrated across the

width of the jet) along the length of the combustor as shown in Figure 46(c). For the flush case, the average intensity is initially high and then remains roughly constant until ~50mm, after which it drops rapidly. This behavior is attributed to the dependence of the scattered light intensity on the liquid morphology. Close to the injector exit, the liquid forms a jet that likely undergoes little evaporation. Downstream, as the jet spreads slightly and breaks up to form droplets, the scattered intensity begins to decrease and this continues as the droplets evaporate. Since the jet spread is limited, the downstream drop in scattering intensity is mainly attributed to evaporation rather than dilution.

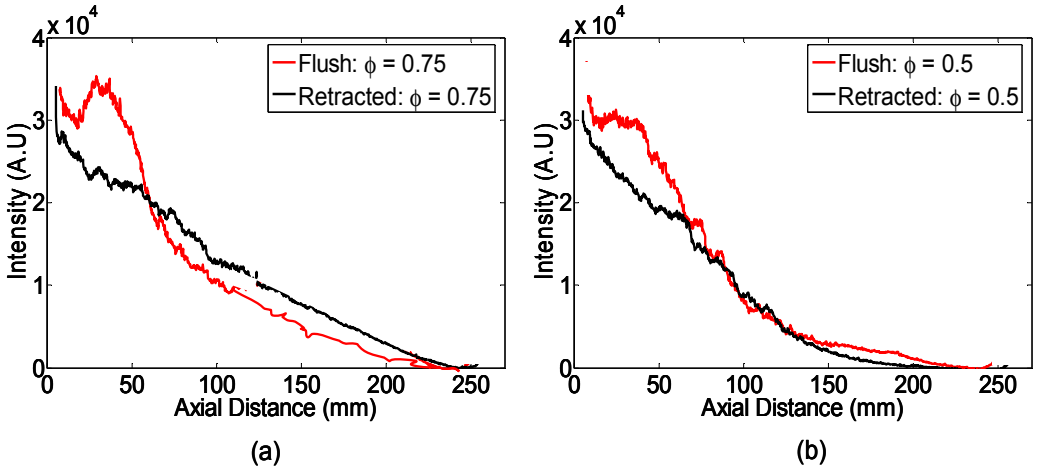

Figure 47. Axial variation of time-averaged, transverse-integrated scattering intensities at mair = 8.1g/s (a) ϕglobal = 0.75 and (b) ϕglobal = 0.5.

In contrast when the liquid injector is retracted, the scattering signal drops more rapidly in the upstream portion of the combustor. This is attributed to the dispersion of liquid droplets across the width of the injector causing fuel-product mixing and more rapid evaporation. In this configuration, the scattering image shows that the liquid does not spread radially, and hence the drop in intensity downstream is again primarily due to evaporation. However, based on a comparison to the flush case, it is seen that for approximately 50mm there is almost no evaporation even inside the combustor where the

temperature is expected to be significantly higher compared to the temperature within the injector. Thus, even when the liquid injector is retracted 80mm into the air tube, the inlet temperature is not expected to be high enough to vaporize any substantial amount of the liquid fuel. On average it is seen that liquid fuel penetrates to approximately 220 mm downstream of the injector for both configurations.

When the global equivalence ratio (ϕ_{global}) is increased to 0.75 while maintaining the same air flow rate, the liquid distribution and the penetration distance remain nearly unchanged for both injector configurations (Figure 47). As seen, initially the rate of fuel evaporation is slightly lower at a higher global equivalence ratio because of the increased mass flow rate of liquid fuel. This difference is more pronounced for the retracted injector. However, further downstream of the injector exit, the higher product temperatures result in rapid evaporation of fuel droplets causing the liquid penetration distance to remain nearly unchanged.

5.3 Flame Characteristics in Liquid-Fueled Operation

The effect of liquid distribution on the combustion process is examined by means of chemiluminescence imaging. The mean CH* (and CO_2*) chemiluminescence field for a global equivalence ratio (ϕ_{global}) of 0.5 and an air mass flow rate of 8.1g/s is shown in Figure 48 for the two injector configurations. As CH* is a marker of heat release, the images reveal that the location of the heat release zone varies significantly depending on the placement of the fuel injector. When the fuel is injected at the exit of the air annulus, a highly lifted flame is observed (Figure 48(a)). No significant heat release is seen until approximately 100mm downstream of the injector; majority of the heat release occurs between 160–240mm (recall, the full combustor length is 300mm). The lack of heat

release near the injector exit is consistent with the fuel distribution seen in Figure 48(a); with the fuel centrally located and shielded from the hot products, no combustion can occur until further downstream where sufficient mixing has occurred. This flame feature is similar to that for nonpremixed gaseous operation of the combustor (Figure 48 (c)), except that the heat release appears to occur in a more extended region (on average). Examination of the instantaneous images suggests that the return flow configuration set by the geometry of the SPRF combustor results in a highly turbulent flowfield causing the flame to exhibit significant radial meandering. Again, this is consistent with the results presented in Chapter 4 for the gas fueled combustor.

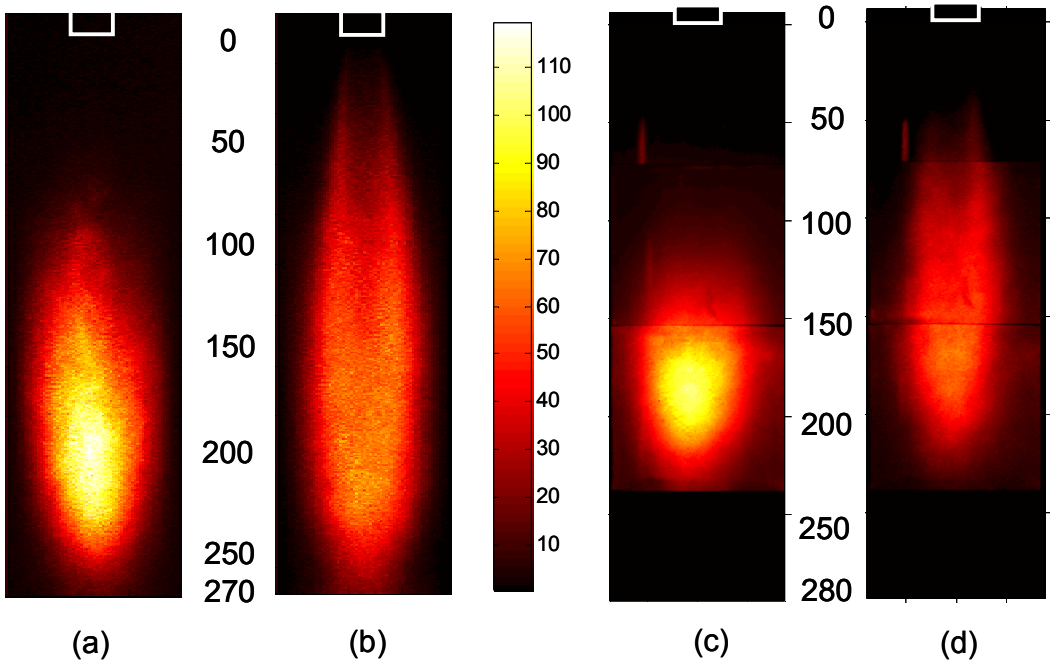

Figure 48. Conditionally averaged CH* chemiluminescence signal for ϕ_{global}=0.5 and m_{air} = 8.1g/s in: Liquid-fueled operation (a) Flush and (b) Retracted cases; and gas-fueled operation at ϕ_{global}=0.6 and m_{air} = 8.1g/s for (c) Nonpremixed and (d) Premixed modes.

When the injector is retracted, however, heat release begins closer to the injector

and extends to the same downstream region as the flush injector case. The near field heat release can occur because some of the fuel is now located along the edge of the inlet jet, where mixing with air and hot products leads to a flammable mixture. The relatively low time-averaged chemiluminescence intensities in this region indicate that a small amount of heat release occurs in the near field region; this may indicate the presence of a highly strained flame in the near-field shear layer between the incoming reactants and exiting products.

A similar shear layer flame region is observed for premixed gas-fueled operation (at the same air mass flow rate, Figure 48(d)). In the liquid-fueled case, however, the flame extends closer to the injector. This may be partly attributed to the lower strain produced when the liquid injector is moved upstream. This placement increases the exit flow area by ~33%, which in turn lowers the exit velocity of the reactant mixture by a similar amount. Based on analysis of the instantaneous images, the flame exhibits less radial meandering in this configuration but has a greater intermittency close to the injector. Presumably the intermittency is associated with the strain and mixture variability in the shear layer between the reactants and returning products close to the injector exit. To account for this, the mean CH* fields shown in Figure 48 were obtained by averaging the instantaneous data conditioned on a chemiluminescence signal above the background noise.

Based on the time-averaged chemiluminescence/heat release images, the combustor operating with a retracted liquid injector, with its greater initial fuel dispersion, more closely resembles operation with gaseous fuel when the reactants are premixed (as opposed to when they are nonpremixed). Hence it appears that retracting the

fuel injector causes the combustor to operate more like a premixed system.

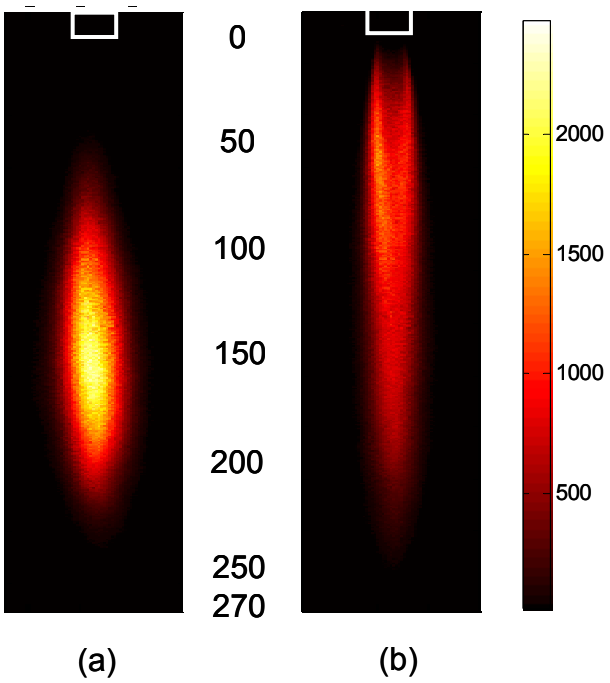

Figure 49. Conditionally averaged CH* chemiluminescence fields for ϕ_{global}=0.75 and m_{air} = 8.1g/s for the different injector placements: (a) Flush and (b) Retracted.

When ϕ_{global} is raised by increasing the fuel flow rate while maintaining a constant air flow rate, the fuel dispersion and liquid penetration did not change significantly. However the combustion characteristics are altered considerably. The averaged chemiluminescence data (Figure 49) show a more compact heat release zone (primarily in radial extent) compared to the global ϕ = 0.5 case for both the injector configurations. As the equivalence ratio increases, the resulting temperature rise causes the overall reactivity of the various species to increase. Consequently, a shorter and more stable flame is obtained at higher equivalence ratios. So instantaneously the flame does not exhibit significant radial meandering and remains confined to central portion of the combustor resulting in a narrowing of the overall heat release zone. When the injector is retracted,

the intermittency close to the injector exit is greatly reduced for the high ϕ case (compared to low ϕ).

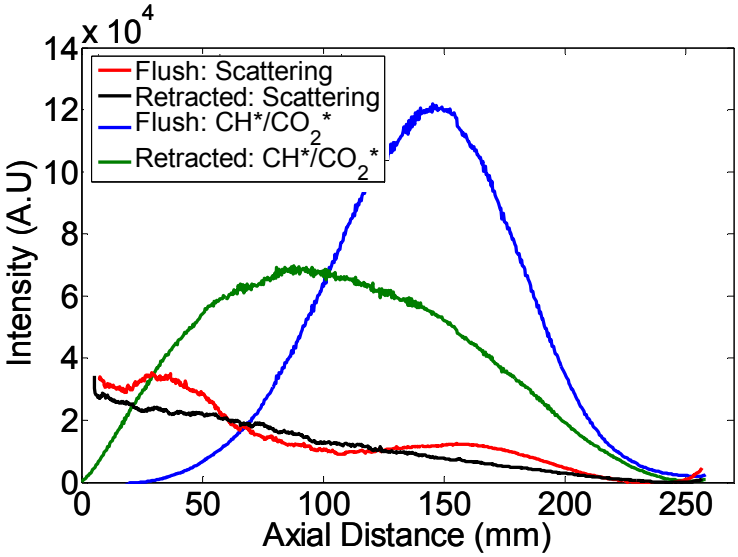

Figure 50. Variation in transverse-integrated CH* signal and scattered intensities with axial distance for m_{air}=8.1g/s and ϕ_{global} = 0.75.

Figure 50 shows the variation in transverse-integrated droplet intensities as well as the chemiluminescence signal with axial distance from the injector exit for the ϕ_{global} = 0.75 case. When the fuel tube is flush with the air annulus, we see a slight increase in the integrated scattering intensities close to the injector before dropping off further downstream. This coincides with the region where the liquid jet breaks up to form droplets. There is a continuous drop in the intensities beyond ~40mm, at which point the heat release starts to pick up. It should be noted that the high chemiluminescence background in the mid-to-far field region causes an apparent rise in the scattering signal due to signal interference. When the fuel tube is retracted, the liquid fuel is well atomized and enters the combustor mostly in the form of droplets. For this case, the immediate rise in heat release due to the presence of a near field shear layer flame causes a steady

decrease in droplet intensity over the entire length of the combustor. This is in contrast to the lower global equivalence ratio (ϕ_{global}=0.5) case where the heat release is delayed until further downstream after almost all the fuel has evaporated and significant fuel-air-product mixing has occurred (Figure 48).

To further examine the combustion process as well as to provide a qualitative understanding of the product entrainment in liquid-fueled operation, simultaneous fuel scattering and OH-PLIF data are presented in Figure 51. It should be noted that the PLIF field seen here is a combination of both OH–PLIF as well as fluorescence signal from both liquid and evaporated Jet-A. To separate the two fields, the laser was tuned off the $Q_1(6)$ line of OH, and simultaneous Jet-A fluorescence and liquid scattering images were acquired.

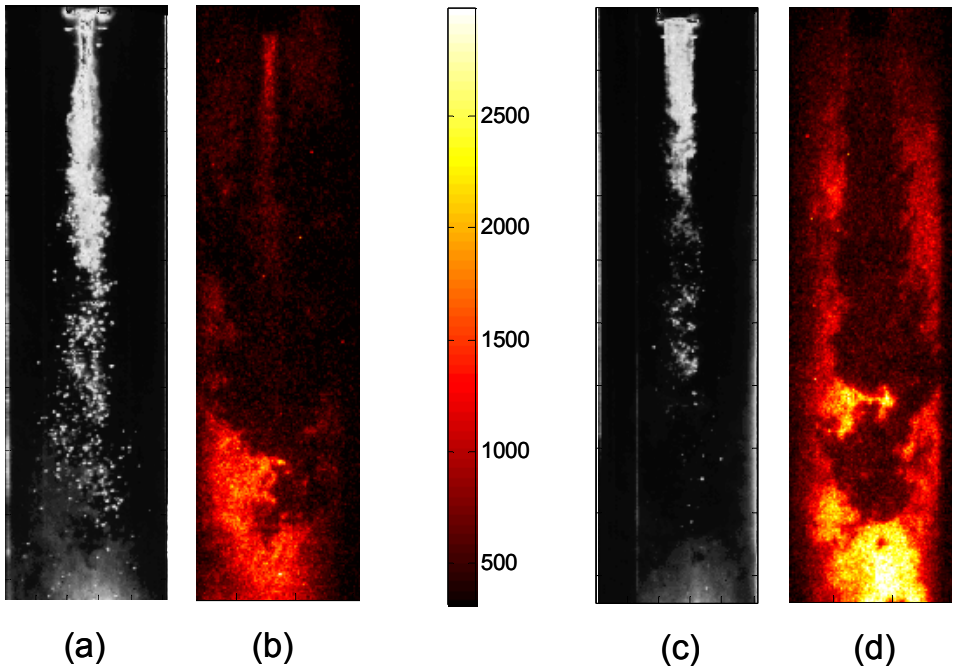

Figure 51. Simultaneous droplet scattering and OH-PLIF data at m_{air} = 8.1g/s and ϕ_{global} = 0.5 for (a) Flush and (b) Retracted cases.

As shown in Chapter 3, the Jet-A florescence signal is mostly obtained from the

fuel in its liquid state, and it is confined mainly to the central portion of the injector where the liquid concentration is highest. Figure 51 (a) shows that the Jet-A fluorescence is significant only for the flush case where the fuel enters as a concentrated liquid jet. There exists a dark region (essentially no fluorescence) separating the Jet-A fluorescence from the OH-PLIF signal indicating that there is little or no droplet burning near the injector exit for the flush case. For the retracted injector, there is almost no observable fluorescence signal from the Jet-A droplets, which are spread across the entire width of the injector.

At low global equivalence ratios, there is no significant OH concentration close to the injector exit for either of the two injector placements. For the retracted case, this indicates that the heat release shown by the chemiluminescence field in that region corresponds to a weak flame mostly in the shear layer between the reactants and the products. Further downstream, the OH PLIF signal increases and reaches its maximum near the end plate just after the flame. The reactants penetrate farther downstream compared to the gas-fueled operation for both injector placements. This may be due to the additional time required for evaporation of the fuel before combustion can occur. Instantaneously, significant radial meandering is also observed at low global equivalence ratios as evidenced by the presence of dark reactant pockets near the combustor walls for both injector placements. It is also interesting to note that the dark regions with no OH signal are wider compared to the PLIF fields obtain with gas-fueled operation of the SPRF combustor. This suggests the overall reaction zone is probably wider and some burning could be occurring in the return flow in liquid operation. As the global equivalence ratio is increased to 0.75 (Figure 52), we see that the reactant penetration is

reduced substantially for both injector placements. This is seen more clearly in the PLIF images, since the scattering signal is affected by the chemiluminescence/PLIF background. Also, the reactant pocket is narrower, indicating that the heat release occurs mostly in the forward moving jet region and there is no significant burning in the return flow.

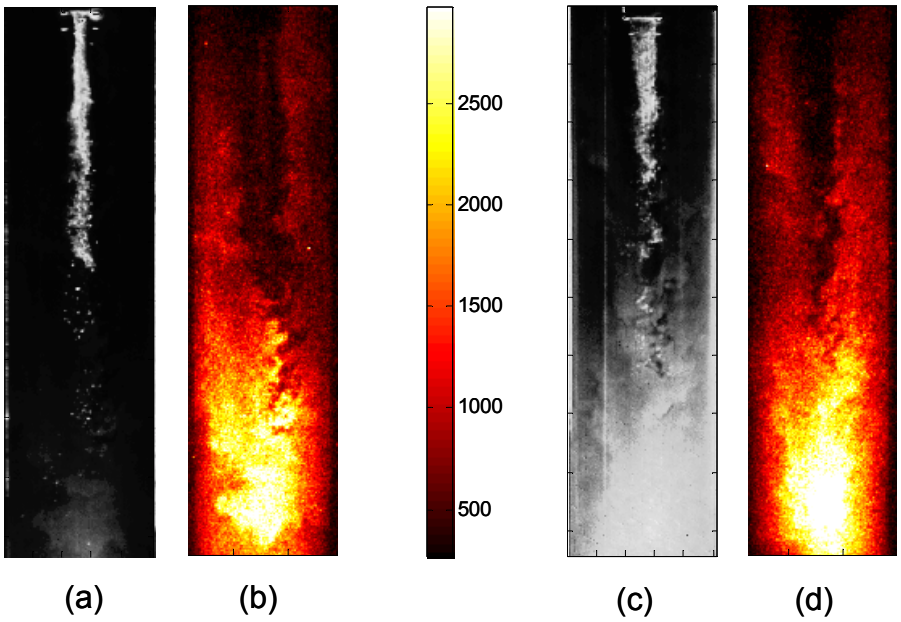

Figure 52. Simultaneous droplet scattering and OH-PLIF data at m_{air} = 8.1g/s and ϕ_{global} = 0.75 for flush case: (a) Scattering, (b) OH-PLIF; and for the retracted case: (c) Scattering, (d) OH-PLIF.

Higher OH PLIF signals are also observed closer to the injector exit for both configurations, which is consistent with the earlier heat release observed at higher inlet fuel-air ratios. For the flush injector, it is seen that a few large droplets survive well into the lower half of the combustor in regions of high OH concentration, suggesting that some of the burning probably occurs in these droplet clusters at near stoichiometric conditions.

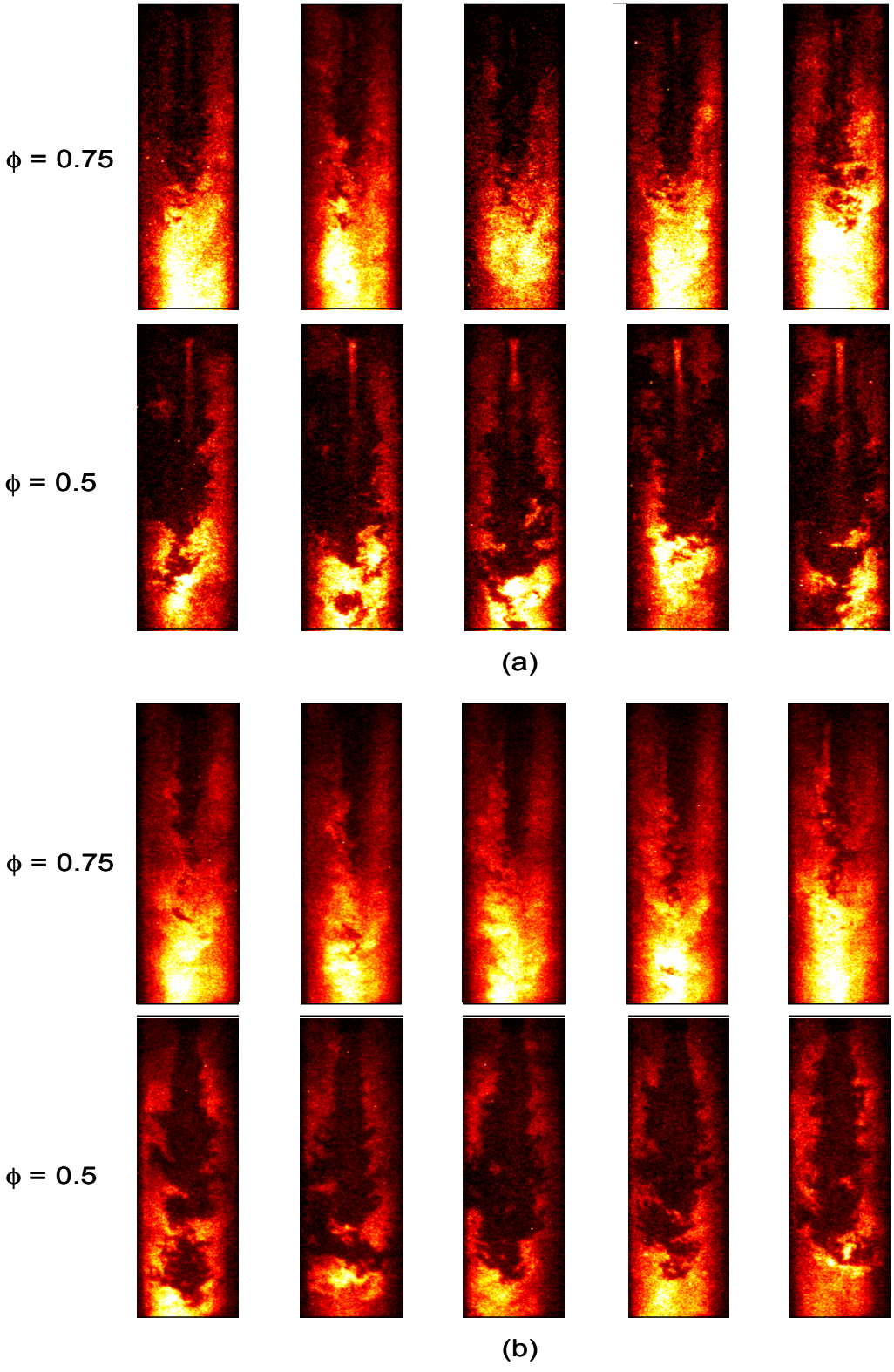

Figure 53. Instantaneous OH-PLIF images at different global equivalence ratios for (a) Flush and (b) Retracted injector.

On an instantaneous basis (Figure 53), the radial meandering is substantially reduced for both injector configurations at the higher equivalence ratio. It should be noted that the colormaps in Figure 53 are adjusted to enhance the contrast between the reactants and products and is not an indication of the differences in OH concentration for the different cases. As seen from the figure, at ϕ_{global}=0.75, the reactant jet is less contorted and remains confined to the central portion of the combustor. In contrast, at lower fuel-air ratios (ϕ_{global}=0.5), the incoming jet meanders a lot and the reactants are sometimes present near the combustor walls. This may be attributed to the higher stability associated with richer mixtures, or the likelihood that the reactants will burn closer to the core of the jet for hotter flames.

It is also interesting to note some of the differences in the PLIF fields for gas- and liquid-fueled operation of the SPRF combustor. The OH distribution is observed to be significantly broader than the heat release/reaction zone indicated by the CH* chemiluminescence data in liquid operation. This occurs because OH also marks the product region, while chemiluminescence is primarily restricted to the reaction zone. In addition, the OH PLIF extends farther downstream in the combustor, closer to the end plate compared to the gas-fueled cases. This may be attributed to at least two causes: (1) differences in mechanisms for OH production and quenching for the different fuels or (2) changes in the temperature profile within the combustor with higher temperatures and possibly some reaction/combustion occurring close to the end plate.

Based on the overall chemiluminescence and PLIF images, the combustor operating with the retracted liquid fuel injector, with its greater initial fuel dispersion, more closely resembles operation with gaseous fuel when the reactants are premixed (as

opposed to when they are nonpremixed). To verify this, integrated CH* chemiluminescence signals and CH*/OH* chemiluminescence ratios are analyzed to study the reaction zone equivalence ratio distribution for the two injector configurations and this data is presented in the next section.

5.4 Flame Zone Equivalence Ratio Distribution

As noted in Chapter 3, it has been shown previously that the total chemiluminescence signal integrated over the entire volume of the combustor can be used as an indicator of the overall reaction zone equivalence ratio. In general, the amount of chemiluminescence from CH* and OH* increases with total fuel flow rate for fixed ϕ and with ϕ for fixed fuel flow rate. For example, for Jet-A, Nori *et al.* [59] have shown that the normalized CH* and OH* chemiluminescence intensities (CH^*/m_f, OH^*/m_f) increase monotonically with equivalence ratio for $0.5<\phi<1.1$ (Figure 54).

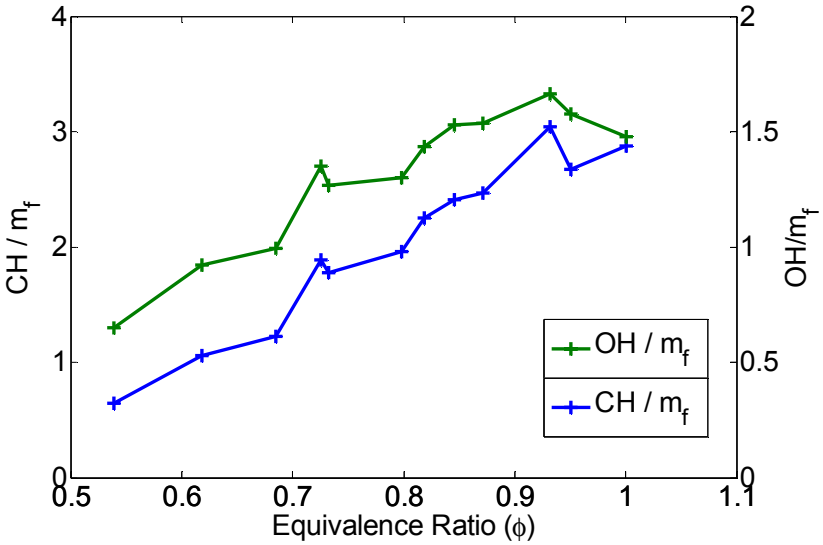

Figure 54. Measured variation of normalized CH* and OH* chemiluminescence signals for Jet -A. [59]

Conditionally averaged CH* chemiluminescence signals were integrated over the

volume of the combustor for the two injector placements and the data is summarized in Table 6 for different global equivalence ratios. As seen in Table 6, the integrated CH* signal is consistently lower for the retracted injector at each ϕ_{global}. The lower intensity obtained when the liquid injector is retracted can be interpreted as a leaner overall burning equivalence ratio compared to the flush case (since both cases have the same flow rates). This is also consistent with the observations from the droplet scattering data presented earlier. When the liquid is injected inside the air annulus and the fuel is dispersed across the inlet, vaporization and partial premixing of air and fuel occur more rapidly than when the fuel is confined within the center of the air jet. The enhanced mixing of vaporized fuel and air leads to leaner fuel-air mixtures in the primary reaction zones, which could aid in reduction of NOx emissions. In gaseous nonpremixed operation of the SPRF combustor, low NOx levels have been attributed to initial shielding of fuel from hot products, which allows the fuel and air to internally premix to nearly the global equivalence ratio before combustion occurs. However, in liquid operation, the additional time required to evaporate the fuel reduces the necessity to shield the fuel.

Table 6. Integrated CH* chemiluminescence signals at different equivalence ratios.

	CH*signal (A.U)	
ϕ_{global}	**Flush**	**Retracted**
0.50	2.3	2.2
0.75	18.8	14.6

It is also seen from Table 6 that the change in the integrated signal when the injector is retracted is much greater at the higher global equivalence ratio. As the temperature increases with ϕ, the enhanced reaction rates lead to a reduction in chemical

times. However as the global equivalence ratio is increased while maintaining a constant air flow rate, the velocities remain nearly the same since the mass flow rate of fuel is negligible compared to that of air. Hence the time scales of mixing remain mostly unaltered as we change the flow condition from ϕ = 0.5 to 0.75. Over this range of equivalence ratios, the enhanced fuel dispersion produced by the retracted injector leads to lower mixing times compared to the flush case, which helps reduce the overall burning zone equivalence ratio. At ϕ = 0.5, this effect is not as evident since the lower temperatures prevent reactions from occurring before fuel-air-product mixing has taken place. However as chemical times decrease at higher global equivalence ratios, the lower mixing times facilitated by the retracted injector results in overall leaner burning in the primary reaction zones. Hence, a greater reduction in NOx emissions is obtained for the retracted case at higher ϕ_{global}.

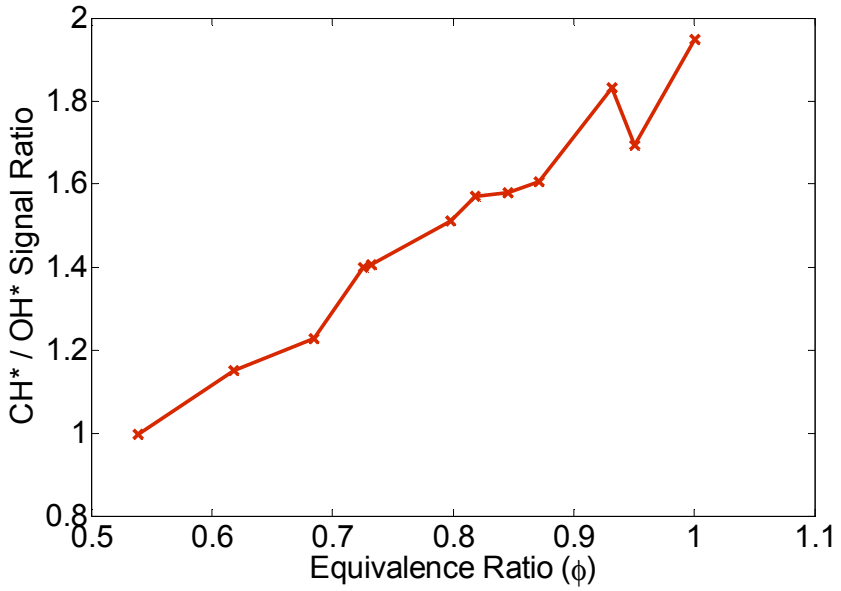

Figure 55. Measured variation of CH*/OH* chemiluminescence ratio with equivalence ratio for Jet-A [59].

Since NOx formation is greatly influenced by the local temperature distribution in

the combustor, it is important to estimate the spatial variation of equivalence ratios produced by the different injector placements. To do this, it is not appropriate to use the integrated CH* or OH* signal since chemiluminescence intensity is also a function of the mass of fuel burned at a given location. This mass dependence is removed by investigating the CH*/OH* chemiluminescence ratio. Previous work has shown that CH*/OH* is good indicator of (local) reaction zone equivalence ratio for several fuels [59]. For methane, this ratio varies monotonically with ϕ, at least for the studied range of $0.7<\phi<1.1$. A similar behavior has also been observed for Jet-A (Figure 55). Thus it may surmised that a high CH*/OH* ratio is an indicator of high equivalence ratio burning. It should be noted, however, that the data provided in the reference does not include the background due to CO_2* radiation that is present in the chemiluminescence data acquired in this study. Thus although the values cannot be compared directly, the distribution of CH*/OH* across the flame zone provides at least qualitative information on the burning equivalence ratio in different regions of the combustor.

Figure 56(a) and (b) show instantaneous images of the ratio, CH*/OH*, for the two injector configurations at $\phi_{global}=0.5$. The distribution of CH*/OH* is fairly uniform showing no systematic variation in the ratios over the entire heat release region in both cases. Moreover, the values are nearly the same for the two fuel injector placements, with the flush case showing slightly higher ratios. Hence it can be inferred that the distribution of equivalence ratios in the combustor is not drastically different for the two injector placements at $\phi_{global}=0.5$. This is consistent with the NOx measurements, which show very little variation in the emission levels for the two injector configuration at this condition. Also, it is observed that most of the heat release occurs in the regions where

CH*/OH* is between 0.5 and 2.

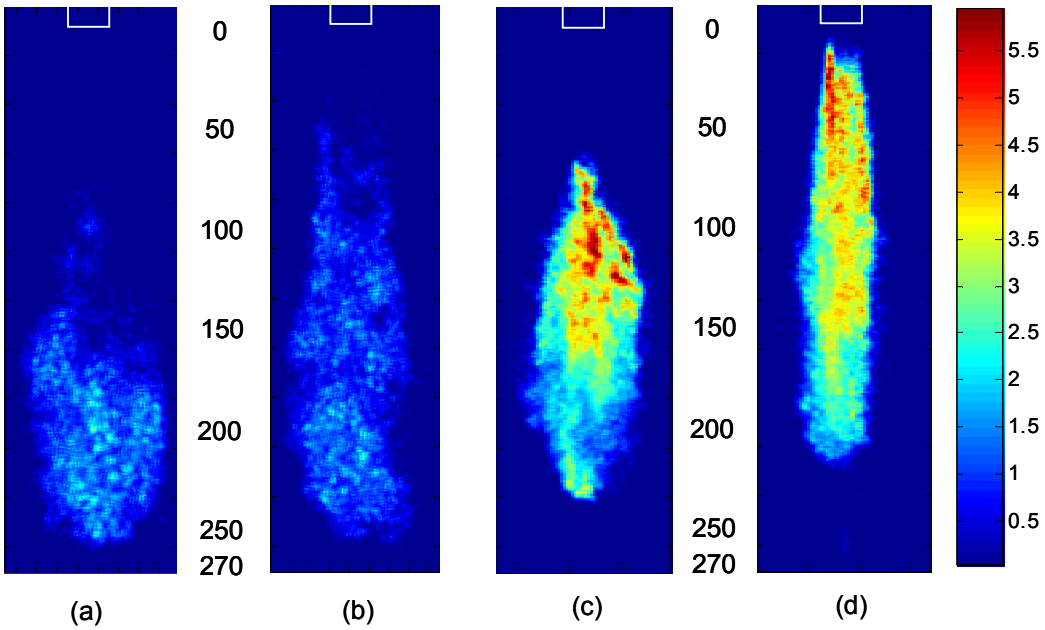

Figure 56. Instantaneous CH*/OH* signal with m_{air} = 8.1g/s and at ϕ_{global}=0.5 for (a) Flush and (b) Retracted cases; and at ϕ_{global}=0.75 for (c) Flush and (d) Retracted cases.

As ϕ_{global} is increased to 0.75 (Figure 56(c), (d)), the CH*/OH* values rise considerably compared to ϕ=0.5 (Figure 56(a), (b)), i.e., the burning zone equivalence ratio increases as ϕ_{global} is increased. In addition, the range of observed CH*/OH* values increases, suggesting a wider range of reaction zone equivalence ratios as ϕ_{global} is increased. The flush injector case (Figure 56c) results in somewhat higher local equivalence ratios compared to the retracted case (Figure 56d). Also, the regions of high CH*/OH*, i.e., richer burning, are primarily close to the injector for the retracted case, whereas they occur downstream for the flush case. In both cases, the burning zone equivalence ratio appears to steadily decrease downstream. Since the overall richer case (ϕ_{global}=0.75) appears to have a significant spatial variation in equivalence ratio, it is

important to ascertain how the equivalence ratio distribution correlates with the heat release distribution.

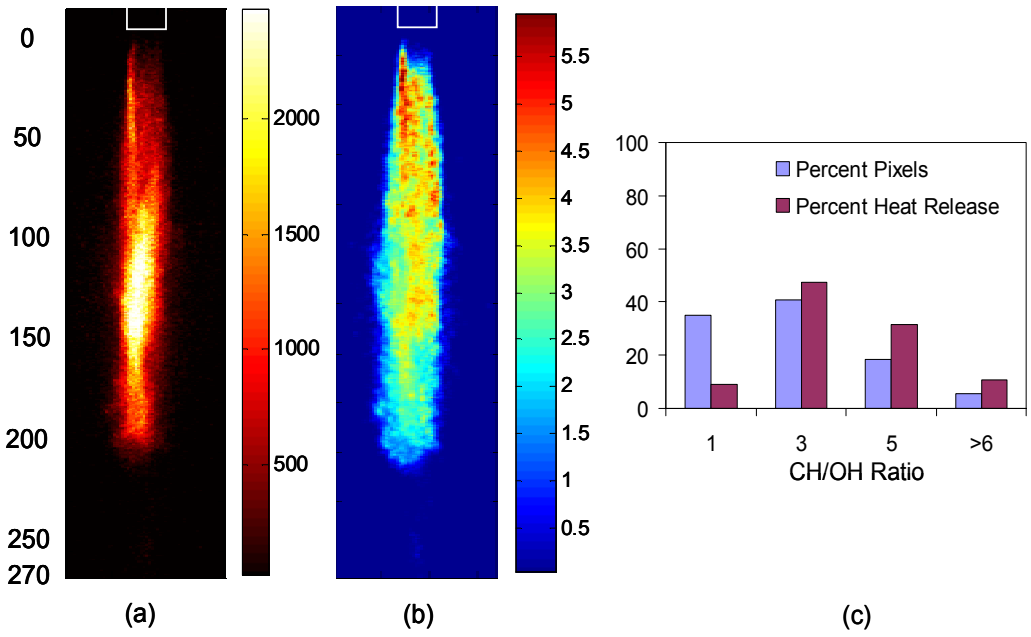

Figure 57. Retracted injector, ϕ_{global}=0.75: (a) Instantaneous CH* chemiluminescence image, (b) Simultaneous CH*/OH* image and (c) Distribution of fractional heat release at different CH*/OH* ratios.

Figure 57 shows an image of instantaneous CH* chemiluminescence (proportional to heat release) along side the corresponding (simultaneous) instantaneous CH*/OH* image (proportional to local equivalence ratio) for the retracted case at a global equivalence ratio of 0.75. While the near field region has the highest fuel-air ratio, a very small fraction of the heat release occurs close to the injector. Most of the heat release occurs downstream (in the mid section of the combustor), where the CH*/OH* values are lower, implying leaner combustion. For the flush case also the heat release occurs in this region, but as seen in Figure 56c, the equivalence ratio of the burning region is still high there. This correlates well with the lower NOx emissions for the

retracted configuration compared to the flush injector.

This is further verified by examining all the instantaneous images (typically 250 realizations are obtained for each condition). First however, the CH*/OH* data is converted to a rough estimate of reaction zone equivalence ratio. Nori *et al.* provide experimental results for the CH*/OH* variation with equivalence ratio for Jet-A based on measurements obtained in a prevaporized, premixed, laminar flame. Their results are calibrated to the current measurement system using the results from the ϕ=0.5 measurements, where the burning equivalence ratio appears to be nearly homogeneous and only slightly richer than the overall ϕ.

Figure 58 shows a histogram of the fraction of image area (i.e., pixels in which a chemiluminescence/heat release signal is present) that correspond to four equivalence ratio ranges (ϕ<0.6, 0.6≤ϕ<0.75, 0.75≤ϕ<0.9, 0.9≤ϕ). As noted above, the equivalence ratios reported in the histograms are only rough estimates, and are intended to provide the reader with a more qualitative rather than quantitative estimate of the ϕ distribution in the reaction zones. Also shown is a histogram of the fraction of heat release (from the CH* images) associated with each equivalence ratio range. Results are presented for three global equivalence ratios and for both injector locations. As ϕ_{global} is increased, the results show that the range of local equivalence ratios measured in the combustor also increases. As noted previously for the leaner case (ϕ_{global}=0.5), the variations of reaction zone equivalence ratios for the flush injector (Figure 58(a)) and retracted injector (Figure 58(d)) are small. Moreover, the majority of the heat release occurs in the same narrow range, though the flush case does show a slightly higher fraction of heat release at local ϕ values near 0.7.

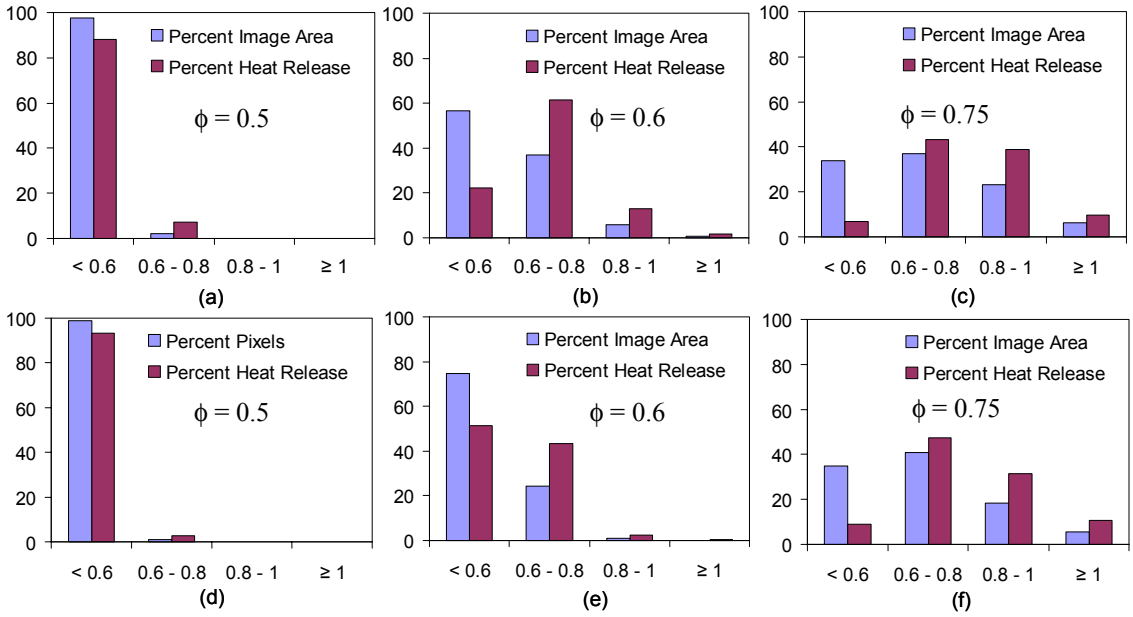

Figure 58. Histogram of the fractional heat release occurring at different global equivalence ratios for the flush case (a) ϕ = 0.5, (b) ϕ = 0.6, (c) ϕ = 0.75 and for the retracted case (d) ϕ = 0.5, (e) ϕ = 0.6, (f) ϕ = 0.75.

Results for an intermediate case (ϕ_{global}= 0.6) show the heat release is spread over a broader range of equivalence ratios (Figure 58(b),(d)). Most (>80%) of the heat release occurs for local ϕ's below ~0.75. In the retracted configuration, the heat release is shifted to lower fuel-air mixtures, with ~50% occurring below ϕ=0.68 and ~90% of the heat release associated with ϕ<0.8. In contrast for the flush case, 10-15% of the heat release occurs at closer to stoichiometric conditions (ϕ>0.9). These small regions of high local fuel-air ratio are the likely source of the higher measured NOx emissions for the flush injector configuration.

For the highest global equivalence ratio case (0.75), both injector configurations (Figure 58(c), (f)) have more than 40% of the heat release occurring in regions with local ϕ>0.75. Again, the flush injector has a slightly higher fraction of heat release associated

with near stoichiometric local conditions. While the distributions for the two injector cases are very close, the small increase in the occurrence of near stoichiometric conditions is still important. Since the NOx penalty associated with near stoichiometric combustion is very high, even this slight increase in burning zone equivalence ratio distribution can result in the significant increase in measured NOx emissions for the flush case at ϕ_{global}=0.75. Therefore the improved fuel dispersion for the retracted injector results in a reduction in equivalence ratios in the primary heat release zone leading to lower NOx emissions over the entire range of global equivalence ratios.

It may be inferred from the above analysis as well as the OH-PLIF images shown earlier that there exists both a partially premixed flame together with diffusion flames around the bigger droplets for the operating conditions investigated here. Although the total number of droplets present is not known, the data suggests that the SPRF combustor in liquid-fueled operation burns in the internal-group combustion regime.

CHAPTER 6

CONCLUSIONS AND RECOMMENDATIONS FOR FUTURE WORK

6.1 Summary and Conclusions

The key features of the flowfield in a stagnation point, reverse flow (SPRF) combustor have been studied with a combination of diagnostic techniques viz., PIV, OH-PLIF, chemiluminescence and laser scattering from liquid particles. The combined effects of confinement, flow reversal and heat release on the flowfield have been detailed. The presence of the closed combustor end and the resulting return flow in the SPRF geometry affect the incoming jet flow significantly. The measured flowfield has been compared to that of other types of jet flows and the effects of confinement and flow reversal have been studied. It is also observed that the "stagnation zone" near the closed end is a region of low mean velocity but significant fluctuating velocity. Towards the far-field region of the combustor the fluctuating and mean velocities become comparable, resulting in high turbulence intensities and enhanced mixing rates for both reacting and nonreacting flows. It is further shown that the decay rate of the jet for nonreacting flow in the SPRF combustor can be roughly approximated as a combination of a free jet and a jet in an uniform opposed flow, at least for the confinement ratio of ~6 in the SPRF studied here. This approximation would be less likely to hold for much smaller confinement ratios.

The flame-turbulence interactions in the reverse flow geometry set up by the SPRF combustor have also been explored. Heat release and preheating of the incoming

reactant jet by the exiting hot products are shown to significantly influence the flow field. This results in an increase in the average and fluctuating velocities for the reacting case as compared to the nonreacting flow. The combined effect is a suppression of turbulent activity compared to the nonreacing case. The reacting flows stagnate farther downstream than the nonreacting flow because of the gas expansion effects associated with heat release. Consequently the jet decay rates are initially lower for the reacting flow compared to the nonreacting case and then increases quickly near the base of the combustor. The jet width and spreading rates in reacting and nonreacting flows are found to be similar, which is attributed to the effect of confinement and the presence of the return flow. All the above results should be generally applicable to similar flowfields with a jet in a self-reversing flow with a stagnation region, as long as the combustor length is not so short that the stagnation zone is close to the jet exit.

Instantaneous velocity and (non-simultaneous) OH PLIF data point to the presence of large vortical structures in the midsection of the combustor that entrain hot combustion products into the reactant stream and thereby increase the chemical reaction rates and aid in flame stabilization. Comparison of the instantaneous flowfields also reveals that the reacting jets exhibit significant lateral motion and distortion compared to the nonreacting case. Therefore it is concluded that the effect of heat release on the flow turbulence is two fold: (1) while the nonreacting flow shows a broad range of structures, the reacting flow shows a considerable reduction in sizes of coherent vortical structures along with a decrease in turbulence intensities and (2) the addition of heat release in a confined environment causes additional large scale unsteadiness and jet meandering, which leads to increased mixing of products and reactants in the heat release regions.

Thus stable operation of the SPRF combustor is a combined result of product entrainment, low mean velocities and high turbulence intensities.

The premixed and nonpremixed reacting velocity fields were found to be similar except in the near field region of the injector. In the nonpremixed mode of operation, the fuel is injected through a coaxial injector such that the fuel and air remain separated till they enter the combustor. As a result the fuel remains shielded from the hot combustion products by the annular air stream surrounding it. Therefore in this configuration, the flame is lifted and stabilized downstream of the injector. This is in contrast to premixed operation, which shows an attached flame stabilized in the near field shear layer. Measurements of the nonpremixed velocity field also show higher turbulence intensities close to injector exit compared to the premixed case, which results in efficient mixing of nearly all the fuel and air before burning. Hence, the flowfield produced by the coaxial injector geometry leads to similar NO_x emissions for both premixed and nonpremixed operation in the SPRF combustor. Since the flame is lifted well away from the injector, air and fuel can premix to nearly the global equivalence ratio before combustion occurs. This is verified by the oil droplet scattering results, which also indicates that hot products are initially separated from the fuel by the surrounding air flow. Further, species concentration measurements have confirmed that the flame in nonpremixed operation is burning only slightly richer than in the premixed case. The entrainment and mixing characteristics reported above are specific to the configuration studied here and are expected to change depending on the injector location (central injection versus peripheral injection) and the relative dimensions of the injector/combustor.

The combustion characteristics of the SPRF combustor operating with liquid fuel (Jet-A) have been also investigated with respect to the variation in NOx emissions for different fuel injector configurations. Non-intrusive optical diagnostic techniques including laser droplet scattering, OH-PLIF and chemiluminescence imaging are employed to analyze the fuel distribution and to study the location of heat release region and reaction zone equivalence ratio distribution in the combustor.

The effect of fuel distribution on the combustion processes in liquid operation of the SPRF combustor was investigated by varying the upstream location at which the liquid fuel is injected, thus altering the spray pattern as well as the extent of fuel-product shielding in the combustor. When the liquid injector is flush with the air annulus, it was observed that the fuel enters the combustor in the form of a liquid jet surrounded by the annular air stream. Shear provided by the high velocity annular air flow facilitates atomization of the liquid jet and also shields it initially from the high temperature return flow. In this configuration it is established that heat release is limited by the rate of evaporation of the liquid and a highly lifted flame is observed where most of the heat release occurs in the central portion of the combustor.

Retraction of the liquid injector into the air annulus (~80mm) results in better dispersion of the fuel across the inlet air jet. In this configuration, although the fuel is no longer shielded from the hot products, the enhanced dispersion has been shown to result in the formation of a leaner mixture of fuel, air and products in the primary reaction zones; thus NOx emissions are reduced. This is confirmed by the chemiluminescence measurements, interpreted two ways: first by the global/integrated chemiluminescence signal (which decreases as the fixed total heat release occurs at a lower average reaction

zone equivalence ratio), and second by CH*/OH* ratios which show that the regions of high heat release are associated with lower reaction zone equivalence ratios in the retracted injector case. Also, it may be surmised that for the current injector dimensions, retraction of the fuel tube further into the air annulus (beyond 80mm) will not provide additional benefit in terms of fuel-dispersion or of reaction zone equivalence ratio since the fuel spray is already spread across the entire width of injector and because little evaporation appears to be occurring within the injector.

The effect of relative time scales for evaporation, mixing and combustion on the emissions performance in liquid operation has also been examined. At low global equivalence ratios, there is sufficient time in both configurations for evaporated fuel to mix well with the air before combustion occurs. For the higher ϕ_{global} cases, the combustor temperature rises, and therefore the characteristic chemical (τ_{chem}) and evaporation (τ_{evap}) times for the reactant/product mixtures decrease. Since the current experiments maintained the overall flowrate nearly constant, the mixing time is expected to be a weaker function of ϕ_{global}, i.e., $\tau_{mix} \approx$ constant. Thus the effective Dahmkohler number ($Da=\tau_{mix}/\tau_{chem}$) for the combustor increases with ϕ_{global}. As *Da* increases, eventually there is not enough time for good fuel-air mixing to occur before reactions begin, and the fuel burns at local equivalence ratios significantly richer than ϕ_{global}. This is confirmed from the chemiluminescence measurements and the CH/OH distribution in the combustor. Since the retracted injector disperses the fuel better, τ_{mix} is lower in this configuration compared to the flush case, and therefore results in leaner reaction zone equivalence ratios at a given ϕ_{global}. These observations regarding the importance of fuel dispersion to reduce the effective mixing times are likely relevant to most injectors,

except for situations where atomization is so fine that evaporation times are so low that the system behaves more like the nonpremixed gas-fueled cases.

Therefore it is seen that the interaction of the chemical times, evaporation rates and mixing times controls the NOx performance of the combustor in liquid operation. While low NOx levels in nonpremixed gas-based operation have been attributed to complete shielding of fuel from products when they enter the combustor, it is observed in liquid-fueled operation that the added delay caused by fuel evaporation before mixing and combustion can occur, changes this fuel-product shielding requirement.

In summary, the results help explain why the SPRF geometry is able to produce a stable flame with relatively low NOx emissions in both premixed and nonpremixed modes of operation, and when fueled with either gaseous or liquid fuels. The velocity measurements obtained in this thesis demonstrate that the geometry of the SPRF combustor ensures the presence of a low velocity, high turbulence "stagnation zone" at high flow rates and low equivalence ratios. This together with internal product recirculation due to the "the reverse flow" creates a stable, combustion process under a large range of combustor operating conditions. The velocity data also provides a comprehensive and reliable data set for comparisons with computational models and serves as an input for development of reduced order analytical models.

The flowfield studies presented here also provide a basis for understanding the NOx performance of the SPRF combustor. In the gas-fueled case, the low emission levels in the nonpremixed mode are attributed to the shielding of the fuel from the hot products, and efficient mixing of most of the fuel and air (and some products) before combustion occurs. In liquid-fueled operation, it is found that retracting the fuel injector well inside

the annulus produces a better-dispersed fuel pattern at the reactant inlet, but the delay required for evaporation still allows time for fuel-air mixing before combustion occurs. This leads to an overall reduction of the equivalence ratio in the fuel consuming reaction zones. This results in a decrease in NOx emissions when the liquid injector is retracted for the entire range of global equivalence ratios investigated.

6.2 Recommendations for Future Work

Although this thesis provides the basis for a comprehensive understanding of the reacting flowfield in the SPRF combustor with gaseous and liquid fuels, there are several other performance aspects that need to be studied further. It would be highly advantageous to obtain simultaneous planar measurements of the velocity field and the reaction zone to better characterize interaction between the combustion zone and the velocity field on an instantaneous basis. Also, the PIV system used in the current study is a 2-component velocity measurement system. As seen from the present work, the flowfield produced by the SPRF combustor is highly 3-dimensional in nature. Therefore, it is highly recommended that future velocity measurements use a stereo-PIV system, which can provide more accurate measurements of the radial and tangential velocities. This would also help generate a more accurate data set for comparison with computational models. To quantify the time scales of jet meandering, it is also necessary improve the frequency response of the existing data acquisition system.

The present study was mainly limited to the influence of changes in equivalence ratio on the flowfield and performance of the SPRF combustor. It is necessary to investigate the effect of changes in loading i.e., variation in air and fuel flow rates on the operation of the combustor. From the current data it is theorized that the velocity field

will remain largely unaltered due to the self-reversing nature of the flowfield produced by the geometry of this combustor. As the inflow velocities are increased, the return flow velocities also rise proportionately causing the jet penetration and stagnation zone properties to remain unchanged. However, the shear layer properties such as strength and width will be affected considerably, which can potentially change the mixing and product entrainment characteristics thus affecting the combustion process as well as the NOx emissions.

Throughout this thesis, the study has been restricted to a simplified baseline combustor and injector geometry. The velocity measurements should be extended to a wider range of configurations; for example flowfield studies should be conducted with different combustor lengths and diameters to better understand the influences of the stagnation plate and the effect of radial confinement on the velocity field and combustion processes. Reducing the overall volume of the combustor also offers distinct advantages in terms of power density and would be of great interest particularly in the aircraft gas turbine industry. Changes in combustor length are also expected to have a significant impact on the product entrainment characteristics which in turn would affect the flame stabilization and emissions performance of the combustor and should therefore be explored more closely.

Also, at this stage, the SPRF combustor is a highly simplified lab-scale atmospheric device. Practical adaptations of this device for use in industrial gas turbines, boilers and furnaces should be explored. To achieve this it is necessary to begin by testing at more realistic high pressure conditions typical of gas turbines. As the pressure is increased, the combustion process is expected to change significantly as the chemical

times are reduced and the flame speeds are altered. In methane, it has been shown that flame speeds are lower at high pressures. Thus there are two competing effects in place that will modify the region where the flame is stabilized. However, the velocity field and consequently the mixing times will likely remain almost unchanged at high pressure conditions because of the reverse flow geometry of the combustor. Thus to maintain low emission levels, it will be necessary to change the fuel injection system and modify the mixing characteristics of the jet so that sufficient time is available for fuel-air-product mixing before combustion occurs. It is also necessary to understand the influence of pressure on the NOx production mechanisms in the SPRF combustor.

Another aspect of the combustor that is hereto unexplored is the combustion dynamics. Since the combustor is essentially a tube with one end closed, there exists a natural resonance frequency which could be acoustically excited at some conditions which may then feed back into the combustion process. Although there is almost no visible or audible combustion instability over the range of equivalence ratios explored, it is necessary to further investigate this possibility especially close to lean blow-out conditions. As the equivalence ratio is reduced, the flame anchoring point tends to oscillate causing a “popping” noise, which suggests a dynamic process that could provide a feedback route in a high pressure combustor.

Lastly, to apply this technology successfully to commercial applications, it is necessary to test the combustor for fuel flexibility. With syn-gas, bio-mass fuels and other low-BTU fuels gaining popularity due to rising oil prices, it is essential for all present day combustors to run stably with different fuels without significant changes in injector design. The SPRF combustor with its high degree of internal mixing and product

entrainment presents an exciting option to burn various fuels effectively while maintaining ultra-low emission levels and should be explored further.

APPENDIX A

SEEDER DESIGN

As noted in Chapter 3, a fluidized bed seeding generator is employed in the current study in order to seed the flow for PIV measurements. The seeder essentially consists of concentric cylindrical vessel with a porous end plate located inside a second cylinder. The air enters the seeder at the bottom through two diametrically opposite holes which allow tangential injection of the air into the seeder (Figure 59).

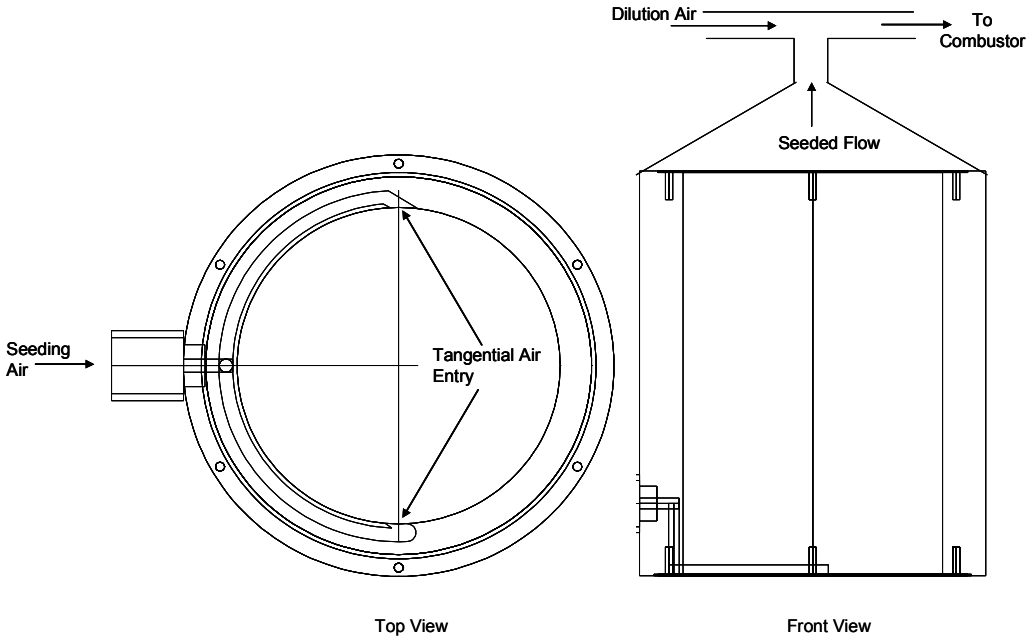

Figure 59. Seeder design.

The swirling air flow then passes through the porous plate of the vessel containing the seed particles which are picked up and carried out through an exit at the top. To adjust the seed density to the required level, the seeded flow may be diluted by mixing more air

before it enters the combustor. The outer vessel of the seeder is also fitted with an air turbine vibrator to prevent particle agglomeration.

APPENDIX B

PIV - STATISTICAL ERROR ANALYSIS

Aside from the uncertainty in the measurement of particle displacement mentioned in Chapter 3, there exist errors in the calculation of the mean and RMS velocities. As seen from the instantaneous data presented in Chapter 4, the flow field in the SPRF combustor is highly turbulent in nature both in the nonreacting as well as the reacting flow cases. For the reacting flow case it was observed that the heat release also causes reactant jet to meander/flap which increases the variance in the data. Therefore the mean and RMS velocities are estimated based on 300-500 independent instantaneous observations of the velocity field.

For the mean velocities, the 95% confidence intervals shown in Figure 60 are calculated based on the following equation:

$$U - \frac{u' t_{n;0.05/2}}{\sqrt{N}} \le U \le U - \frac{u' t_{n;1-(0.05/2)}}{\sqrt{N}}$$

$$n = N - 1$$

where U is the mean velocity, u' is the standard deviation i.e., root mean square (RMS) velocity, $t_{n;0.05/2}$ is the area of the curve under a t-distribution with n degrees of the freedom and N is the number of independent observations. For N > 120, $t_{n;0.05/2} \approx \sqrt{2}$. Since the values of the instantaneous velocities used in this calculation include the measurement uncertainty, the data along with the 95% confidence intervals represent the total error in the mean velocity data.

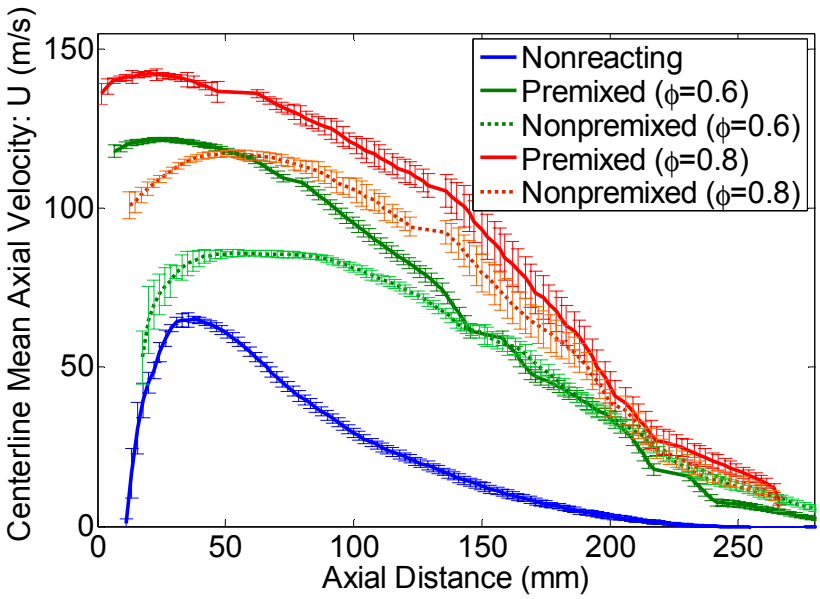

Figure 60. Variations of centerline mean axial velocity along with 95% confidence intervals.

Based on the above calculations, it seen that the maximum error in the velocity measurements is ~12% and occurs near the stagnation region. Elsewhere the error in the mean velocities is approximately 7-8%.

Similarly, the 95% confidence intervals for the RMS velocities can be estimated as a function of the sample size, N and the standard deviation of the velocity (s) at a given point based on the following expression:

$$\sqrt{\frac{ns^2}{\chi^2_{n:0.05/2}}} \leq u' \leq \sqrt{\frac{ns^2}{\chi^2_{n:1-0.05/2}}}$$

where n = N-1 and $\chi^2_{n:0.05/2}$ is the value of a chi-square distribution with n degrees of freedom. The variation of the centerline RMS velocities along with the 95% confidence intervals is shown in Figure 61. Based on the data, it is observed that the

maximum error in the RMS velocities is ~12-15% and the largest errors are observed mid-way through the length of the combustor where majority of the heat release occurs.

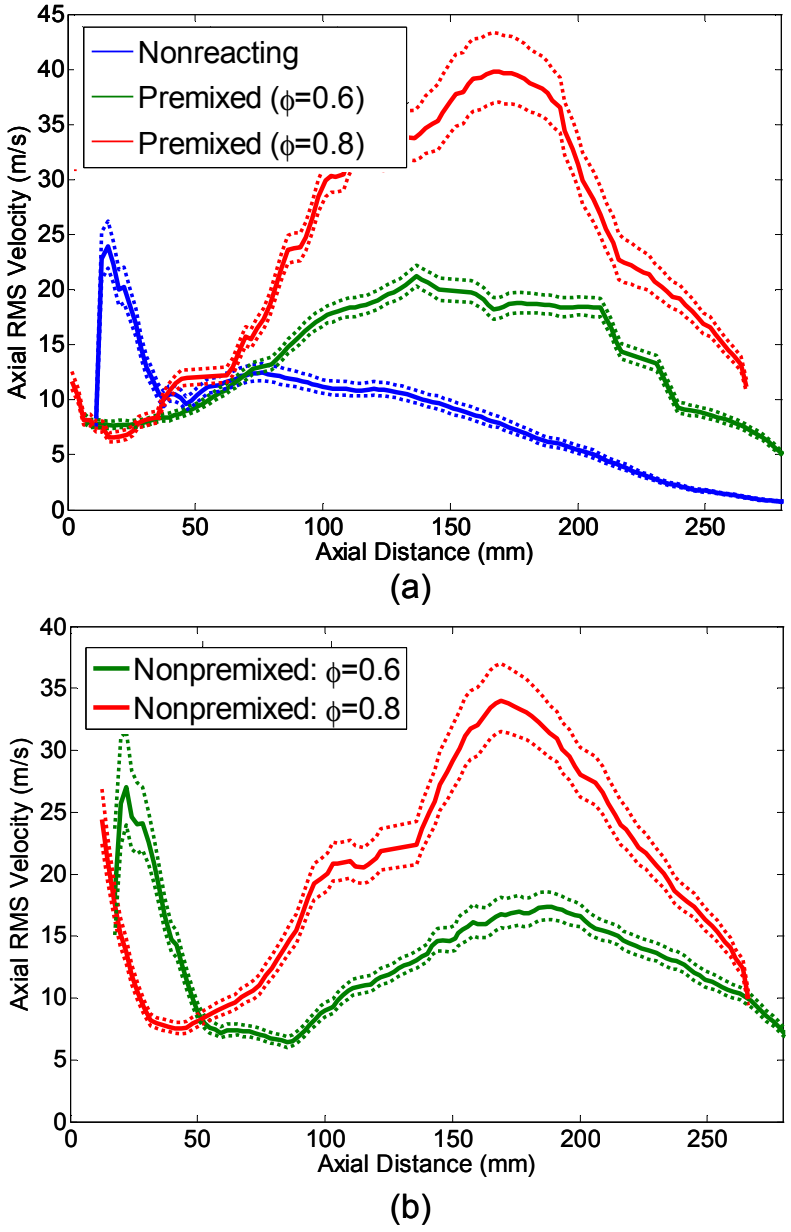

Figure 61. Variations of centerline axial RMS velocity along with 95% confidence intervals.

REFERENCES

1 http://www.aero-space.nasa.gov/goals/emissions.html (Accessed: June, 2004)

2 Correa, S.M., "Power Generation and Aeropropulsion Gas Turbines: From Combustion Science to Combustion Technology", Proceeding of the Combustion Institute, Vol. 27, 1998, pp. 1793-1807.

3 Tacina, R., Mao, C. P., and Wey, C., "Experimental Investigation of a Multiplex Fuel Injector Module for Low Emission Combustors", AIAA 2003-0827, AIAA Aerospace Sciences Meeting, Reno, NV, 2003.

4 Richards, G. A., McMillian, M. M., Gemmen, R. S., Rogers, W. A., and Cully, S. R., "Issues for low-emission, fuel-flexible power systems", Progress in Energy and Combustion Science, Vol. 27, 2001, pp. 141-169.

5 Lefebvre, A. H., "Gas Turbine Combustion", Taylor & Francis, Philadelphia, 1998.

6 Arai, M., "Flue gas recirculation for low NOx combustion system", IJPGC2000-15073, Proceedings of 2000 International Joint Power Generation Conference Miami Beach, Florida, July 23-26, 2000.

7 Arai, M., "Flue gas recirculation for low NO_x combustion system", IJPGC2000-15073, Proceedings of 2000 International Joint Power Generation Conference Miami Beach, Florida, July 23-26, 2000.

8 Neumeier, Y., Weksler, Y., Zinn, B.T., Seitzman, J.M., Jagoda, J. and Kenny, J., "Ultra low emissions combustor with non-premixed reactants injection," AIAA 2005-3775 41st AIAA/ASME/SAE/ASEE Joint Propulsion Conference & Exhibit 10 - 13 July 2005, Tucson, Arizona.

9 J. Crane, Y. Neumeier, J. Jagoda, J. Seitzman and B. Zinn, "Stagnation− Point Reverse− Flow Combustor Performance With Liquid Fuel Injection", GT2006-91338, Proceedings of the ASME/IGTI Turbo Expo 2006, Barcelona, Spain May 8-11, 2006.

10 C. J. Chen, and W. Rodi, "Vertical Turbulent Buoyant Jets; A Review of

Experimental Data", Pergamon, Oxford, 1980, HMT Vol. 4.

11 List, E. J., "Turbulent jets and plumes", Annual Review of Fluid Mechanics 14, 1982, pp189-212.

12 Panchapakesan, N.R., and Lumley, J.L., "Turbulence measurements in axisymmetric jets of air and helium. Part 1. Air jet", Journal of Fluid Mechanics 246, 1993, pp197-223.

13 Hussein, H. J., Capp, S. P. and George, W. K., "Velocity measurements in a high-Reynolds-number, momentum-conserving, axisymmetric, turbulent jet", Journal of Fluid Mechanics 258, 994, pp31-75.

14 Falcone, A. M., and Cataldo, J. C., "Entrainment Velocity in an Axisymmetric Turbulent Jet", Journal of Fluids Engineering, Vol.125, July 2003 pp 620-627.

15 Xu, G. and Antonia, R. A., "Effect of different initial conditions on a turbulent round free jet", Experiments in Fluids: 33, 2002, pp 677-683.

16 Boersma, B.J., Brethouwer, G. and Nieuwstadt, F., T., M., "A numerical investigation on the effect of the inflow conditions on the self-similar region of a round jet", Physics of Fluids 10, 1998, pp899–909.

17 Ferdman, E., Otugen, M.V. and Kim, S., "Effect of initial velocity profile on the development of round jets", Journal of Propulsion and Power 16, 2000, pp676–686.

18 Djeridane, T., Amielh, M., Anselmet, F. and Fulachier, L., "Velocity turbulence properties in the near-field region of axisymmetric variable density jets", Physics of Fluids 8, 1996, pp1615-1630.

19 Borean, J.L, Huilier, D., and Burnage, H., "On the effect of a co-flowing stream on the structure of an axisymmetric turbulent jet", Experimental Thermal and Fluid Science 17, 1998, pp10-17.

20 Rajaratnam, N., "Turbulent Jets", Elsevier Scientific Publishing Co., Amsterdam, Netherlands, 1976.

21 Chua, L. P. and Lua, A. C, “Measurements of a confined jet”, Physics of Fluids, Vol. 10, No. 12, December 1998, pp3137-3144.

22 Serres, I., Chauveau, C., Sarh, B., and Gokalp, I., “Characterization of confinement and impingement effects on the near field of axisymmetric jets using LDA and PIV”, 10th International Symposium on Applications of Laser Techniques to Fluid Mechanics, Lisbon, Portugal 2000.

23 Champagne, F.H. and Wygnansky, I.J., “An experimental investigation of coaxial turbulent jets (Flow field generation by coaxial turbulent jets, determining velocity distribution, turbulence intensities and shear stresses by hot-wire anemometers)”, International Journal of Heat and Mass Transfer 14, 1971, pp445-1464.

24 Dahm, W.A., Friedler, C.E. and Tryggvason, G, “Vortex Structure and Dynamics in the Near Field of a Coaxial Jet”, Journal of Fluid Mechanics, 241, 1992, pp371-402.

25 Durão, D. and Whitelaw, J.H., “Turbulent Mixing in the Developing Region of Coaxial Jets”, Transactions of the ASME - Journal of Fluids Engineering, 1973, pp467-473.

26 Villermaux, E. and Rehab, H., “Mixing in coaxial jets”, Journal of Fluid Mechanics, 425, 2000, pp161- 185.

27 Driscoll, J. F., Chen, R-H. and Yoon, Y., “Nitric oxide levels of turbulent jet diffusion flames: Effects of residence time and Damkohler number”, Combustion and Flame 88, 1992, pp37-49.

28 Chen, R-H. and Driscoll, J.F., “Nitric Oxide Levels of Turbulent Jet Diffusion Flames: Effect of Coaxial Air”, Proceedings of the Combustion Institute 23, 1990, pp281-288.

29 Kim, S-H., Yoon, Y. and Jeung, “Nitrogen Oxides Emissions In Turbulent Hydrogen Jet Non-Premixed Flames: Effects Of Coaxial Air And Flame Radiation”, Proceedings of the Combustion Institute, Vol. 28, 2000, pp463-470.

30 Lam, K., M. and Chan, C., H., C., “Round Jet in Ambient Counterflowing Stream”, Journal of Hydraulic Engineering, Vol. 123, No. 10, October 1997, pp895-903.

31 Beltaos, S., and Rajaratnam, N., "Circular turbulent jet in an opposing infinite stream", Proceedings of the 1st Canadian Hydrotechnical Conference, Edmonton, Canada, 1973, pp220–237.

32 M. Yoda and H. E. Fiedler, "The round jet in a uniform counterflow: Flow visualization and mean concentration measurements", Experiments in Fluids 21, 1996, pp427-436.

33 Lam, K., M. and Chan, C., H., C., "Time-Averaged Mixing Behavior of Circular Jet in Counterflow: Velocity and Concentration Measurements", Journal of Hydraulic Engineering, Volume 128, Issue 9, September 2002, pp861-865.

34 Lam, K., M., Lee, W., Y., Chan, C., H., C. and Lee, J., H., W., "Global Behaviors of a Round Buoyant Jet in a Counterflow", Journal of Hydraulic Engineering,Volume 132, Issue 6, June 2006, pp589-604.

35 Yamaguchi, S., Ohiwa, N., and Kinoshita, S., "A Study on Opposed Jet Flames Stabilized in a Uniform Air Stream (1st report: Development of Isothermal Opposed Jets.)", Bulletin of the JSME, Vol. 18, No. 121, July 1975.

36 Yamaguchi, S., Ohiwa, N., and Kinoshita, S., "A Study on Opposed Jet Flames Stabilized in a Uniform Air Stream (2nd report: Mixing Characteristics of an Opposed Jet.)", Bulletin of the JSME, Vol. 18, No. 121, July 1975.

37 Ballal, D. R., "An Experimental Study of Flame Turbulence", Acta Astronautica, Vol. 5, Nov. - Dec.1978, pp1095-1112.

38 Ballal, D. R., "Studies of Turbulent Flow-Flame Interaction", AIAA Journal, Vol. 24, No. 7, July 1986, pp1148-1154.

39 Ballal, D., R. and Lefebvre, A., H., "Turbulence Effects on Enclosed Flames", Acta Astronautica, Vol. 1, Mar.-Apr. 1974, pp471-483.

40 Ballal, D. R., "Combustion-Generated Turbulence in Practical Combustors", Journal of Propulsion, Vol. 4, No. 5, Sept-Oct 1988, pp385-391.

41 Rink, K. K. and Lefebvre, A. H., "The Influences of Fuel Composition and Spray Characteristics on Nitric Oxide Formation", Combustion Science and Technology: 68, pp 1-14, 1989.

42 Sirignano, W. A., “Fluid Dynamics and Transport of Droplets and Sprays”, Cambridge University. Press, 1999.

43 Chiu, H. H. and Liu, T. M., “Group Combustion of Liquid Droplets”, Combustion Science and Technology 17, 1977, pp127-131.

44 Rangel, R. H. and Sirignano, W. A., “Combustion of parallel fuel droplet streams”, Combustion and Flame 75, 1989, pp241-254.

45 Griebel, P., Bombach, R., Inauen, A., Schären, R., Schenker, S. and Siewert, P., “Flame Characteristics and Turbulent Flame Speeds of Turbulent, High-Pressure, Lean Premixed Methane/Air Flames”, GT2005-68565, Proceedings of GT2005 ASME Turbo Expo 2005: Power for Land, Sea, and Air, Reno-Tahoe, Nevada, USA June 6-9, 2005.

46 Muniz, L., Martınez, R. E. and Mungal, M. G., “Application of PIV to turbulent reacting flows”, Developments in Laser Techniques and Fluid Mechanics (Berlin: Springer) 1997, pp 411–424.

47 Keane, R., D. and Adrian, R., J., “Theory of cross-coreelation analysis of PIV images”, Applied Scientific Research, Vol. 49, No. 3, July 1992, pp191-215.

48 Adrian, R. J., Christensen, K. T. and Liu, Z.-C., “Analysis and interpretation of instantaneous turbulent velocity fields”, Experiments in Fluids, Vol. 29, No. 3, September 2000, pp275-290.

49 Sung, C. J., Law, C. K. Axelbaum, R. L., “Thermophoretic Effects on Seeding Particles in LDV Measurements of Flames”, Combustion Science and Technology, Vol. 99, No, 1-3, August 1994, pp119-132.

50 Melling, A., “Tracer Particles and Seeding for Particle Image Velocimetry”, Measurement Science and Technology 8, 1997, pp1406-1416.

51 Roby, R. J., Reaney, J .E., and Johnsson, E. L. “Detection of Temperature and Equivalence Ratio in Turbulent Premixed Flames Using Chemiluminescence”, Proceedings of the 1998 International Joint Power Generation Conference, Vol. 1, 1998, 593-602.

52 Ikeda, Y., Kojima, J., and Nakajima, T. “Chemiluminescence based local

equivalence ratio measurement in turbulent premixed flames", AIAA-2002-0191, 40th Aerospace sciences meeting and exhibit, Reno, Nevada, Jan 14-17, 2002.

53 Morrell, M. R., Seitzman, J. M., Wilensky, M., Lubarsky, E. and Zinn, B. T., "Interpretation of Optical Emissions for Sensors in Liquid Fueled Combustors", AIAA 2001-0787 39th AIAA Aerospace Sciences Meeting and Exhibit, Jan. 8-11, 2001 Reno, Nevada.

54 Muruganandam, T. M., Kim, B.-H., Morrell, M. R., Nori, V., Patel, M., Romig, B. W. and Seitzman, J. M., "Optical Equivalence Ratio Sensors for Gas Turbine Combustors", Proceedings of the Combustion Institute 30, 2005, pp1601-1609.

55 Seitzman, J. M. and Hanson, R. K. "Planar fluorescence imaging in gases: Instrumentation for Flows with Combustion", ed. A. M. K. P. Taylor, 1993.

56 Baranger, P., Orain, M. and Grisch, F., "Fluorescence Spectroscopy of Kerosene Vapour: Application to Gas Turbines", AIAA 2005-828, 43rd AIAA Aerospace Sciences Meeting and Exhibit, Jan.10-13 2005, Reno, Nevada.

57 Gopalakrishnan, P., Undapalli, S., Bobba, M. K., Sankaran, V., Menon, S. and Seitzman, J. M., "Measurements and Modeling of the Flow Field in an Ultra- Low Emissions Combustor", AIAA-2006-0962, 44th Aerospace Sciences Meeting, Reno, NV, Jan 9-12, 2006.

58 Bobba, M. K., "Flame Stabilization and Mixing Studies in a Stagnation Point Reverse Flow Combustor", Ph.D Thesis, Georgia Institute of Technology, December 2007.

59 Nori, V. N. and Seitzman, J. M., "Chemiluminescence Measurements and Modeling in Syngas, Methane and Jet-A Fueled Combustors", AIAA-2007-0466, 45th Aerospace Sciences Meeting, Reno, NV, Jan 8-11, 2007.